Univerzita Karlova v Praze
Matematicko-fyzikální fakulta

DIPLOMOVÁ PRÁCE

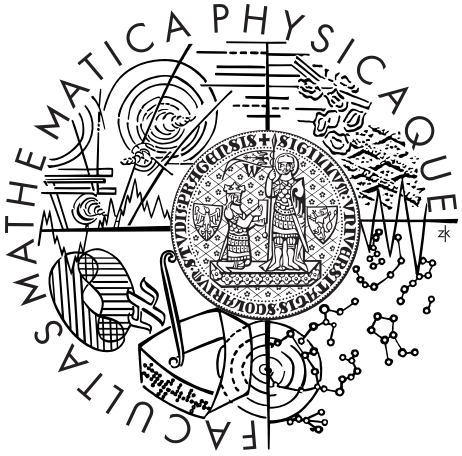

Petr Cejpek

Rentgenová difrakce a difuzní rozptyl na Heuslerových slitinách

Katedra fyziky kondenzovaných látek

Vedoucí diplomové práce:	prof. RNDr. Václav Holý, CSc.
Studijní program:	Fyzika
Studijní obor:	Fyzika kondenzovaných soustav a materiálů

Praha 2015

Charles University in Prague
Faculty of Mathematics and Physics

MASTER THESIS

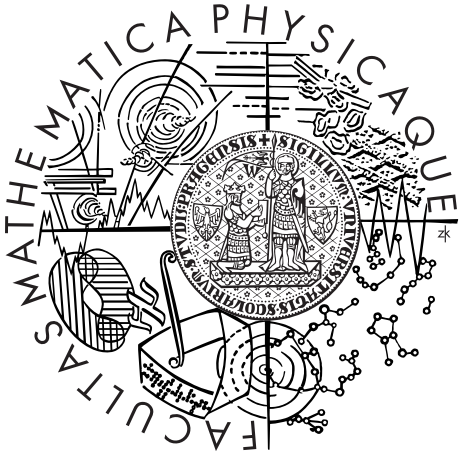

Petr Cejpek

X-ray diffraction and diffuse scattering from Heusler alloys

Department of Condensed Matter Physics

Supervisor of the master thesis:	prof. RNDr., Václav Holý, CSc.
Study programme:	Physics
Specialization:	Physics of Condensed Systems and Materials

Prague 2015

I hereby would like to show my appreaciation to my supervisor prof. RNDr. Václav Holý, CSc. for guiding my work and for sugestions to its processing. Next, I would like to thank Mgr. Jan Endres for helping me with the processing EXAFS data. Although the attempts of single-crystaline samples preparation has not been successful, I am grateful to RNDr. Jiří Pospíšil, PhD. and RNDr. Michal Vališka as well for a support and also to RNDr. Jana Šmilauerová for a help with opening the molybdenum capsules. One part of thanks belongs to Mgr. Lukáš Horák, PhD. as well, who teached me how to perform a mesurement of diffractions in high temperatures.

I want to thank doc. Stanislav Daniš for good advices with the program *FullProf*. I am obligated to my friend and colleague Bc. Attila Bartha too for a help with work on the vacuum unit and for much advices to work with the LaTeX.

And I cannot forgot to show my big appreaciation to Ms. Chau Pham, who has read all my work and tried to correct mistakes in my english grammar and other aspects in my writting.

I declare that I carried out this master thesis independently, and only with the cited sources, literature and other professional sources.

I understand that my work relates to the rights and obligations under the Act No. 121/2000 Coll., the Copyright Act, as amended, in particular the fact that the Charles University in Prague has the right to conclude a license agreement on the use of this work as a school work pursuant to Section 60 paragraph 1 of the Copyright Act.

In ..... date ..... signature of the author

Název práce: Rentgenová difrakce a difuzní rozptyl na Heuslerových slitinách

Autor: Petr Cejpek

Katedra: Katedra fyziky kondenzovaných látek

Vedoucí diplomové práce:
prof. RNDr. Václav Holý, CSC., Katedra fyziky kondenzovaných látek

Abstrakt: Heuslerovy slitiny jsou v poslední době studovány pro své zajímavé vlastnosti, ať už magnetické či elektronické. Tyto vlastnosti podstatně závisejí na krystalové struktuře. Práce se zabývá studiem Heuslerových slitin typu A2BC. Studium proběhlo jak na práškových, tak na monokrystalických vzorcích. Cílem je popsat krystalickou strukturu jednotlivých vzorků, určit obsazení mřížkových poloh jednotlivými atomy a jejich případné rozuspořádání. Na práškových vzorcích byla změřena prášková difrakce a EXAFS. Na monokrystalických vzorcích byly změřeny klasické a v případě přítomnosti modulované struktury byly změřeny i satelitní difrakce.

Klíčová slova:
Heuslerovy slitiny, okupační rozuspořádání, okupační čísla, modulovaná struktura

Title: X-ray diffraction and diffuse scattering from Heusler alloys

Author: Petr Cejpek

Department: Deparment of Condesed Matter Physics

Supervisor:
prof. RNDr., Václav Holý, CSc., Department of Condesed Matter Physics

Abstract: Recently, Heusler alloys are studied for their interesting magnetic and electronic properties. These properties are strongly dependent on the crystallographic structure. This work deals with Heusler alloys of the A2BC type. We have powder samples and single-crystaline samples for our study as well. An object of interest was a description of crystallographic structure of the samples, site occupation numbers of each type of atoms and their possible occupation disorder. Powder difraction and EXAFS have been measured on the powder samples. Clasical single-crystal diffractions has been meassured on the single-crystaline samples. In the case of a modulated structure in the samples, satelite difractions have been measured too.

Keywords:
Heusler alloys, occupation disorder, site occupations, modulated structure

Contents

Introduction **2**

1 Fundamentals of Heusler alloys **4**
1.1 Structure of the Heusler parent phase 4
1.2 Disorder phenomena 5
1.3 Application of the Heusler alloys 7

2 Theory of experimental methods, samples preparation **9**
2.1 Theoretical principles of the used experimental methods 9
2.1.1 Single crystal diffraction 9
2.1.2 Laue method 11
2.1.3 Powder diffraction 12
2.1.4 EDX 13
2.1.5 EXAFS 14
2.2 Preparation of the samples 16
2.2.1 Powder samples 17
2.2.2 Single-crystalline samples 17
2.2.3 List of the used samples 19

3 Powder diffraction and EDX on series $Mn_2Co_{1-x}Rh_xSn$ **20**
3.1 EDX 20
3.2 Powder diffraction 21
3.3 Summary 28

4 EXAFS measurement on powder samples $Mn_2Co_{1-x}Rh_xSn$ **31**
4.1 Obtaining of EXAFS spectra from the measured data 31
4.2 Processing of EXAFS spectra 31
4.3 Summary 37

5 Single-crystal diffraction on Ni_2MnGa **38**
5.1 Lattice parameters and domain structure 38
5.2 Modulation of the structure 46
5.3 Diffraction at higher temperatures 50

Discussion and conclusions **56**

Appendix **59**
A Matlab scripts 59

Bibliography **70**

List of Tables **74**

List of Abbreviations **75**

Attachments **76**

Introduction

Heusler alloys are named after their discoverer - german geochemist Friedrich Heusler, who has discovered them at the turn of the nineteenth and twentieth century. Heusler found [1] that manganese forms ferromagnetic compounds with some metals, although none of elements in the compound is ferromagnetic itself.

Nowadays, we take Heusler alloys as ternar compounds of selected elements and we distinguish two main groups according to a stoichiometry: full-Heusler alloys with the stoichiometry 2:1:1 and half-Heusler alloys with the stoichiometry 1:1:1. These alloys are often investigated for their various properties. For example, the work [2] describes all important fundamentals of these compounds. Heusler alloys can exhibit a number of interesting properties, such as a magnetic shape memory [3, 4, 5] or a superconductivity [6]. Full-Heusler alloys are used for a fabrication of monochromators in neutron diffraction [7], where we apply the diffraction 111 in a parent Heusler phase. Half-Heusler alloys are used mostly as semiconductors. We can observe the properties, which are analogical to topological insulators, on them [8]. Heusler alloys are investigated for their spintronic behaviour [9, 10].

The properties of Heusler alloys are strongly dependent on their structure. Band structure calculations show that already small amounts of a disorder within a distribution of the atoms on atomic sites cause distinct changes in an electronic structure [11]. This is the reason, why the proper examination of a structure is really valuable. In this thesis, I deal with the structure of some Heusler alloys and I study their structure with x-rays.

The first object of interest is an examination of the possible occupation disorder in specified Heusler alloy. The powder samples of the series $Mn_2Co_{1-x}Rh_xSn$ have been chosen as representative specimens. These series have been studied previously for their magnetic properties (see [12]), where the autors investigated the increase of Curie temperature because of doping. Mn_2CoSn has been analysed in [13] to obtain its electronic, magnetic and structural properties. I study these samples with powder diffraction and EXAFS to obtain some information of the possible occupation disorder. In the case of powder diffraction, information is obtained by the fitting of diffraction patterns and by the fitting of corresponding integrated intensities to their theoretical values. In a theoretical formula for the integrated intensities, the structure factor plays an important role, because it includes information about occupation of each site in the unit cell. Therefore, an own script for generation randomly disordered unit cells and for the subsequent fitting has been written.

EXAFS was chosen as another method to determine possible occupation disorder. EXAFS is a spectroscopic method, which is based on the absorbtion and scattering of x-ray radiation by individual atoms and it is very sensitive to a local structure in the closest neighborhood of specified atom. Because of an unique electronic structure of each element, this method should be able to distinguish between individual types of atoms, which sit in the unit cell. The EXAFS will be measured on the specified samples from the series $Mn_2Co_{1-x}Rh_xSn$ in a powder form. Because of a presence of Co and Mn atoms in the samples, EXAFS spectra will be measured on CoK and MnK absorption edges, which are well accessi-

ble with synchrotron radiation. The proccessing of the measured data will be done with the set of programs *Demeter* [14], which includes scripts for ab initio multiple scattering calculations and the subsequent fitting.

Next task is a study of specified Heusler alloy in a single-crystalline form. Ni_2MnGa was chosen as a suitable specimen. Recently, this material is well studied, because it is one of the few members of shape memory Heusler alloys. This material has several structure features such as the twinning and the modulation in the structure, which should be well visible by single-crystal diffraction. Up to now, the structure of the Ni_2MnGa has been studied mostly with powder diffraction. For example, [15] deals with the modulated structure measured by high-resolutin x-ray powder diffraction, or [16] deals with the martensite transformation studied with powder diffraction as well. Beside this, there are few articles, which deal with single-crystal diffraction on it (see [17] for instance). Because the properties of Ni_2MnGa are well tunable by its composition, it is worth to study the structure of each sample. Only a small difference from the 2:1:1 stoichiometry leads to a distortion of the basic structure - however the parent phase is cubic, the distortion may lead to a tetragonal and even monoclinic structure.

An examination of Ni_2MnGa is performed by high-resolution reciprocal space mapping on CuKα wavelength. The structural features mentioned above should lead to extra diffraction spots in the measured reciprocal maps. We are able to determine their origin from their positions in reciprocal space. The twinning should lead to more than one diffraction spot close to the expected diffraction coordinates. Beside this, the modulated structure should lead to the diffraction spots with non-integer indices. Because of the mentioned martensite transformation, high-temperature diffraction measurement was performed. The change of the structure should lead to a disappearance of diffraction peaks belonging to a low-temperature phase and an appearance of peaks belonging to a more symetric cubic high-temperature phase. The temperature of the transition and possible hysteresis should be well visible.

The original plan included a study of $Mn_2Co_{1-x}Rh_xSn$ single-crystalline thin layers by diffuse x-ray scattering, but we were not able to prepare required specimens. Therefore, I have focused on a study of powder samples and additional experimental method has been chosen to study their structure (EXAFS mentioned above).

This work is divided in several chapters. In the first chapter, I briefly introduce Heusler alloys, their possible applications and especially the structure of their parent phase. One section in the first chapter is devoted to the occupation disorder. The second chapter is devoted to theoretical basics and several formulas of the experimental methods, which will be necessary to know for following proccesing of the measured data. Other chapters are devoted to the individual experimental methods and their results. The results from EDX and powder diffraction on the series $Mn_2Co_{1-x}Rh_xSn$ are shown in the third chapter. Next chapter shows the results from EXAFS measurement. The final fifth chapter is devoted to single-crystal diffraction measurement on the sample Ni_2MnGa. There, I show the results from room-temperature and high-temperature measurement.

1. Fundamentals of Heusler alloys

1.1 Structure of the Heusler parent phase

Generaly, Heusler alloys are divided into two main groups according to the stoichiometry: full-Heusler alloys (the formula X_2YZ) and half-Heusler alloys (the formula XYZ). The letters X, Y and Z describe some of selected elements from the periodic table. In Figure 1.1 the periodic table is depicted and the most common elements X, Y and Z are shown with a color difference. As one can see, the Z elements are always from the right hand side of the table (half-metals). The element X is mostly one of the transition metals and the Y element can be one of the wide range of metals.

The basic structure of Heusler alloys is cubic. Structure of half-Heusler alloys can be described with a combination of the ZnS-type and the NaCl-type of structure - the X element sits then in octahedral sites. This structure can be described with the space group $F\bar{4}3m$ (n. 216) and the atoms sit in these Wyckoff positions: X in $4c$ $\left(\frac{1}{4},\frac{1}{4},\frac{1}{4}\right)$, Y in $4b$ $\left(\frac{1}{2},\frac{1}{2},\frac{1}{2}\right)$ and Z in $4a$ $(0,0,0)$. Corresponding unit cell is depicted in Figure 1.2a.

Structure of full-Heusler alloys can be described with four interpenetrating *fcc* lattices. For an interpretation of the symetry we can choose the space group $Fm\bar{3}m$ (n. 225) and the atoms lie in these Wyckoff positions: X in $8c$ $\left(\frac{1}{4},\frac{1}{4},\frac{1}{4}\right)$, Y in $4b$ $\left(\frac{1}{2},\frac{1}{2},\frac{1}{2}\right)$ and Z in $4a$ $(0,0,0)$. But we can have another type of structure. If the atom X is more electropositive than Y we obtain the inverse structure (in case that X and Y are from the same period, X has smaller atomic number). The inverse structure looks like that one half of the X atoms from $8c$ position swap his position with the Y atoms in $4b$ - the inverse four-fold axis occurs. This structure can be expressed again with the space group $F\bar{4}3m$ (as in the case

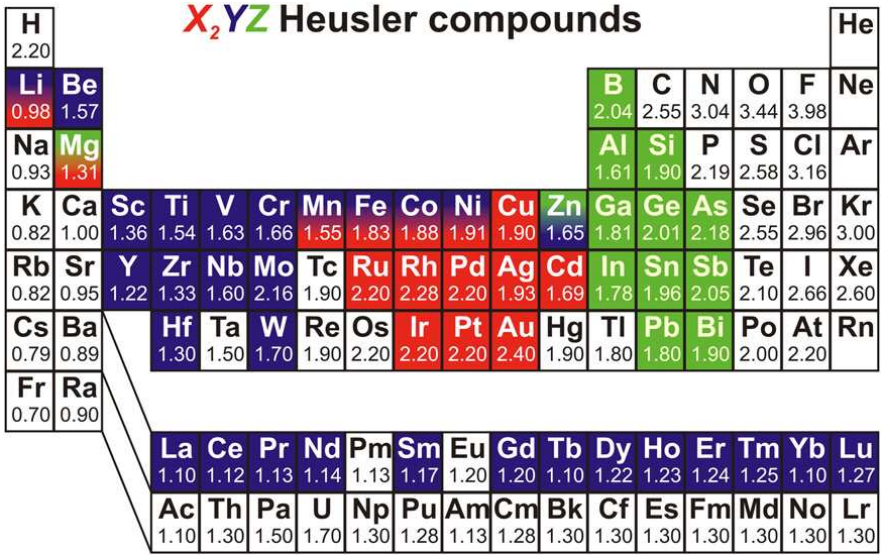

Figure 1.1: This figure is taken from [2]. The picture shows the most common elements used in the Heusler alloys. The X elements are labelled with red color, the Y element with blue one and the Z elements in green one.

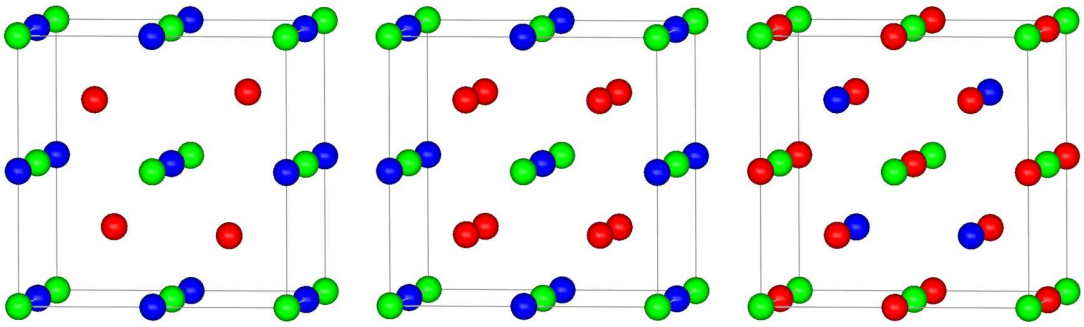

(a) half-Heusler (b) full-Heusler (c) inverse full-Heusler

Figure 1.2: The structure of Heusler parent phase. The colors correspond to the colors in Figure 1.1.

with half-Heusler alloys) and the atoms $X^{(1)}$, $X^{(2)}$, Y and Z occupy the Wyckoff positions $4d$ $\left(\frac{3}{4},\frac{3}{4},\frac{3}{4}\right)$, $4c$, $4b$ and $4a$ respectively. Both of these structures are shown in Figure 1.2b and 1.2c.

The structures described above are basic and they could be distorted due to a chemical composition, dopants and other effects. The most common effect might be a disorder of the atoms. For example, if the atomic numbers of the elements X and Y are similar, they can occupy mutually their positions in the unit cell. We observe four basic types of an occupation disorder, which are shown and characterized for example in [2]. Also, we can observe a tetragonal distortion. It can be frequently observed in compounds Mn_2YZ. In several cases, hexagonal analogues of Heusler alloys can be found, for instance in the compounds XYZ with X = RE (rare earth).

1.2 Disorder phenomena

As mentioned, we can observe several types of the occupation disorder in Heusler alloys. Previous research and band structure calculations show that already small amounts of disorder within a distribution of the atoms on the atomic sites lead to distinct changes in an electronic structure, and corresponding changes in their magnetic and transport properties [11]. Here, I will describe briefly some of the common types of the occupation disorder, which are typical for full-Heusler compounds.

If the Y and the Z atoms are evenly distributed, their positions in the lattice become equivalent. This leads to the CsCl-type of disorder. As a consequence of this, the symmetry is reduced and the resulting space group is $Pm\overline{3}m$. In the other case, if we have a random distribution of X and Y or X and Z, the BiF_3-type of disorder occurs. This leads to the space group $Fm\overline{3}m$. Other type of the occupation disorder, the NaTl-type, is observed very rarely. Here, the X atoms, which occupy one of the *fcc* sublattices, are mixed with the Y atoms, whereas the X atoms on the second sublattice are mixed with the Z atoms. The corresponding space group is then $Fd\overline{3}m$. In a contrast to the previous partial occupation disorder, all positions become equivalent in the W-type of disorder and the symmetry is reduced to $Im\overline{3}m$. These types of disorder are depicted in Figure 1.3.

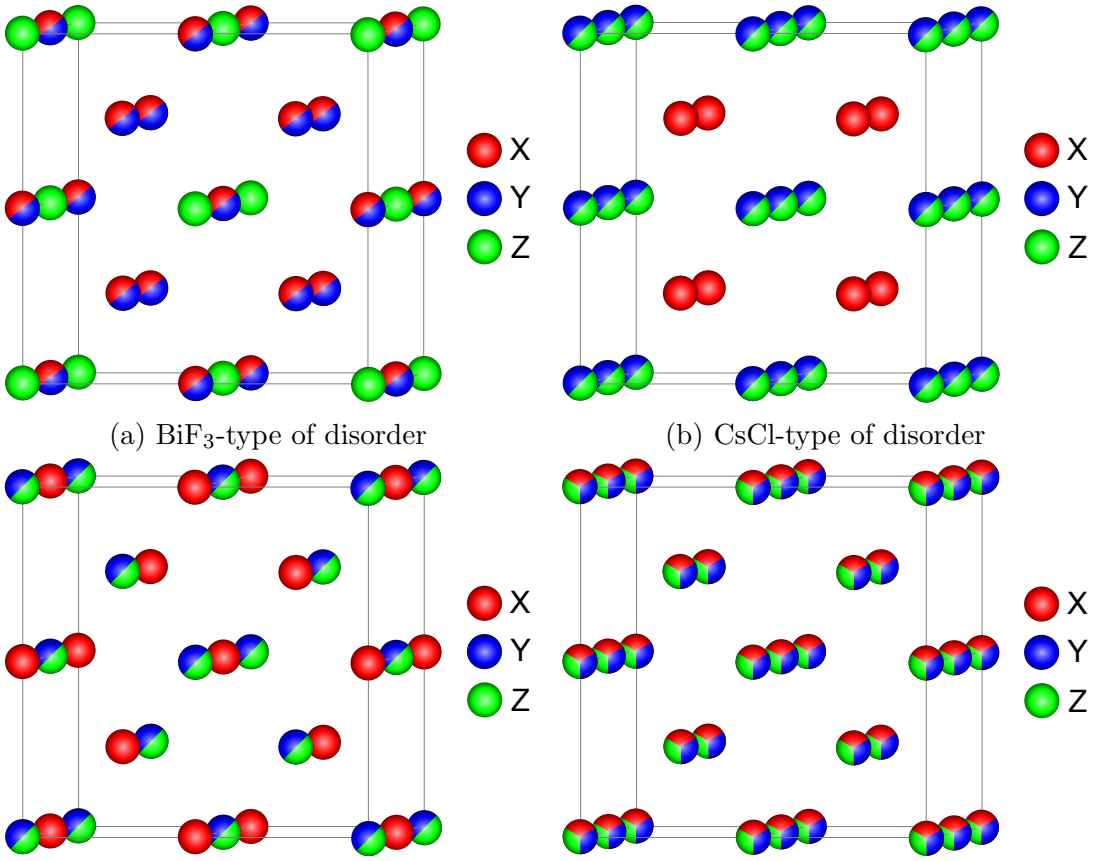

(a) BiF_3-type of disorder (b) CsCl-type of disorder

(c) NaTl-type of disorder (d) W-type of disorder

Figure 1.3: The types of the occupation disorder in the full-Heusler alloys

disorder	sp.group	$site_X$	occ_X	$site_Y$	occ_Y	$site_Z$	occ_Z
CsCl-type	$Pm\overline{3}m$	8g	1	1a,1b,3c,3d	$\frac{1}{2}$	1a,1b,3c,3d	$\frac{1}{2}$
BiF_3-type	$Fm\overline{3}m$	4b,8c	$\frac{2}{3}$	4b,8c	$\frac{1}{3}$	4a	1
NaTl-type	$Fd\overline{3}m^*$	8a	1	8b	$\frac{1}{2}$	8b	$\frac{1}{2}$
W-type	$Im\overline{3}m$	2a,6b,8c	$\frac{1}{2}$	2a,6b,8c	$\frac{1}{4}$	2a,6b,8c	$\frac{1}{4}$

Table 1.1: Atomic sites occupied by individual types of the atoms in the types of fully disordered structures. $site_X$ means the atomic site which is occupied by the atom X, occ_X is the corresponding occupation number. **the first choice of the origin*

If we have a completely distorted structure with respect to an occupancy, we can compute the occupation numbers of the individual atoms as a probability that we would find individual atoms at these sites. There is a list of the atomic sites and the occupation numbers in Table 1.1. In an example, one can see [19] for the complex information about the space groups, atomic sites and their coordinations.

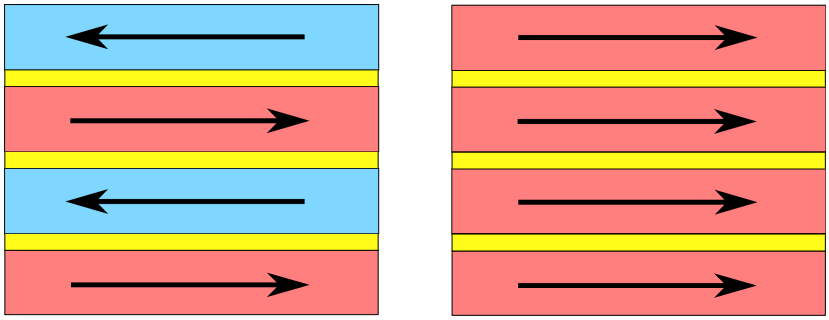

Figure 1.4: Ordering of magnetic moments in the spin valve.

1.3 Application of the Heusler alloys

Heusler alloys have plenty of interesting properties and due to that they can have a lot of possible application. Some of the material properties can be roughly predicted due to the rules of a number of the valence electrons. For instance, if half-Heusler compound has 18 valence electron per unit cell, it is semiconductor. We can apply similar rule to full-Heusler compounds, but with the 24 valence electrons. Obviously, there are several exceptions - for example if we have a compound with manganese or if a tetragonal distortion in the structure is present. Some works such as [2, 20, 21] can be read for other information. I will introduce briefly some interesting groups of Heusler alloys in the following section.

- **compounds suitable for spintronics** - The spintronics took its important place in the information technology after the discovery of giant magnetoresistance (GMR). Today, we are in daily contact with spintronics, in form of spin valves based on GMR effect, which are used in magnetic hard disk drives. There is such a spin valve in Figure 1.4. In that device, two magnetic layers sandwich a very thin non-magnetic layer (spacer). If a magnetization of both ferromagnetic layers is aligned in parallel direction, the resistance of the device is low (the electric current can flow trough, it means logical 1), whereas a high resistance is present, if the ferromagnetic layers are aligned antiparallely (logical 0). The resistance of the valve can be tuned with a thickness of the spacer or with an external magnetic field.

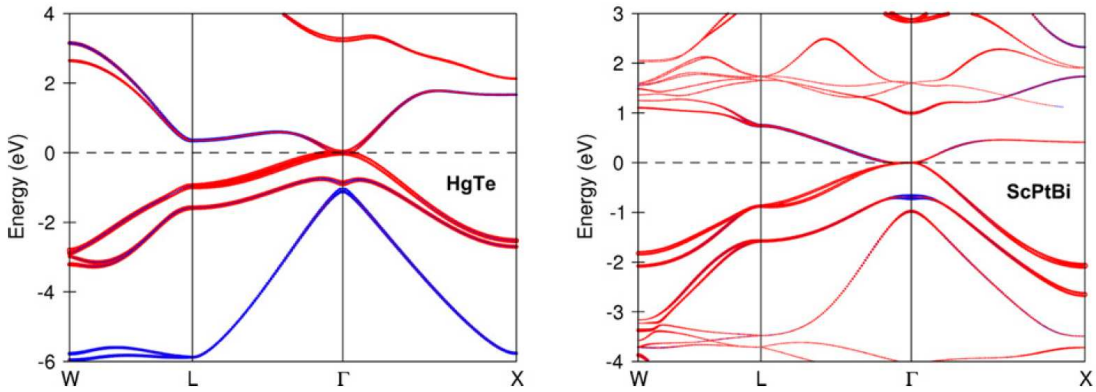

Figure 1.5: The picture is taken from [2]. There is a comparison of the band structure of HgTe and half-Heusler alloy ScPtBi in this figure.

The materials, which is suitable for spintronics, must have high spin polarisation, high Curie temmperature and their possible atomic disorder has to be well controllable.

- **shape memory alloys** - Today, the most intensively studied system is Ni_2MnGa. This kind of alloys exhibits well tunable properties, which can be reached due to the change in a composition. Curie temperature T_C and the temperature T_M (temperature of the transition to a low-tamperature structure martensitic phase) are two of them. The twinning may occur in these systems as well. Their application takes place in the actuator devices, because strain of these alloys can be well controlled by an external magnetic field. Also, a magnetic field can easily shift their twin boundaries.

- **superconductors** - The family of Heusler compounds includes not only metallic and semiconducting materials, but superconducting compounds as well. Pd_2RESn was the first discovered superconducting Heusler alloy. However, several other superconducting Heusler compounds have been discovered, their critical temperatures are too low from an application point of view. Heusler superconductors have to fulfill the condition of the van Hove singularity, which should be close to the Fermi energy [2, 22] and they have to have 27 valence electrons per elementary unit (similar rule like that one for Heusler semiconductors mentioned above). An interesting thing is that for RE containing compounds, a coexistence of superconductivity and a magnetically ordered state has been reported [23].

- **thermoelectric materials** - A thermoelectric device creates voltage when there is a difference in temperature between its individual sides. Conversely, when we apply a voltage to it, the temperature difference occurs. As said, half-Heusler compounds exhibit semiconductor properties. It is seemingly possible to dope individual sublattices to optimize the thermoelectric properties. For example, we could vary the number of charge carriers by doping the sites with Z element, and simultaneously introduce disorder by doping the X and Y position. This should lead to a mass fluctuation and decrease of a thermal conductivity. Up to now, n-type TiNiSn-based compounds have been most intensively investigated, but recently great progress was made for p-type TiCoSb-based materials as well.

- **topological insulators analogues** - To design a topological insulator we need a direct band gap at the center of the Brillouin zone - Γ point is favorable [24]. It is worth to mention that the name topological insulators is slightly misleading - the systems are, in fact, low band gap semiconductors such as Bi_2Te_3 (300 meV) or even zero band gap semimetals such as HgTe. There is a comparison of the band structure of the HgTe and ScPtBi in Figure 1.5. The properties of Heusler topolocial insulators can be tuned with a strain or with a composition.

2. Theory of experimental methods, samples preparation

2.1 Theoretical principles of the used experimental methods

An examination of samples with x-rays has a wide range of use. One can use for example x-ray diffraction (XRD) to obtain basic geometry of the lattice, x-ray photo-electron spectroscopy (XPS) to obtain some information of energy levels, energy-dispersive x-ray spectroscopy (EDX) is used for the elemental analysis or a chemical characterization of the samples or for instance we can choose extended x-ray absorption fine structure (EXAFS) to obtain some information of the nearest atom neighborhood. I will describe the methods, which I have used, in the following section.

2.1.1 Single crystal diffraction

XRD is analogical to the diffraction on the grid in the visible region of a light. Because typical atomic distances in solids are in the order of 10^{-10} m = 1 Å, we need to use a light with a comparable wavelength. In a laboratory, we use a copper lamp mostly and x-rays, which it emits, have a typical wavelength $\lambda_{\mathrm{Cu}K\alpha} = 1.54056$ Å.

Let us consider the scattering of a monochromatic plane wave on a crystal. The atoms scatter x-rays and there a path difference occurs between each two beams, which are scattered by neighboring planes of the atoms. An interference of the individual scattered beams leads to the diffraction. There are several ways how to describe the conditions of the diffraction. The basic formula is so-called Laue condition:

$$\vec{Q} = \vec{k}_f - \vec{k}_i = \vec{G}_{hkl} \tag{2.1}$$

where $\vec{Q}$ is the scattering vector, $\vec{k}_f$ is the wave vector of the scattered beam, $\vec{k}_i$ is the wave vector of the incidence beam and $\vec{G}_{hkl}$ is a reciprocal lattice vector. If the Laue condition is fulfilled and the angle between the primary beam and the outline of planes (hkl) is Θ, the same angle must be between the outline and the diffracted beam. This situation can be described with the Bragg equation:

$$2d_{hkl} \sin\Theta = \lambda \tag{2.2}$$

where λ is the wavelenght of x-rays and d_{hkl} is the interplanar distance of the outline of planes (hkl) (it has a relation to $\vec{G}_{hkl}$). The h, k, l are indices of the diffraction here, so it indicates that $\vec{G}_{hkl}$ points to some reciprocal lattice point and the indices h, k, l have not be relatively prime integers. As one can see, the angle 2Θ is the angle between the diffracted and the primary beam. It can be derived from the relation between the reciprocal lattice vector and the interplanar distance and from the Equation 2.2 that norm of the scattering vector is:

$$\left|\vec{Q}\right| = \frac{4\pi}{\lambda}\sin\Theta \tag{2.3}$$

Another description of the conditions of the diffraction is so-called Ewald construction (see [25] or [26]).

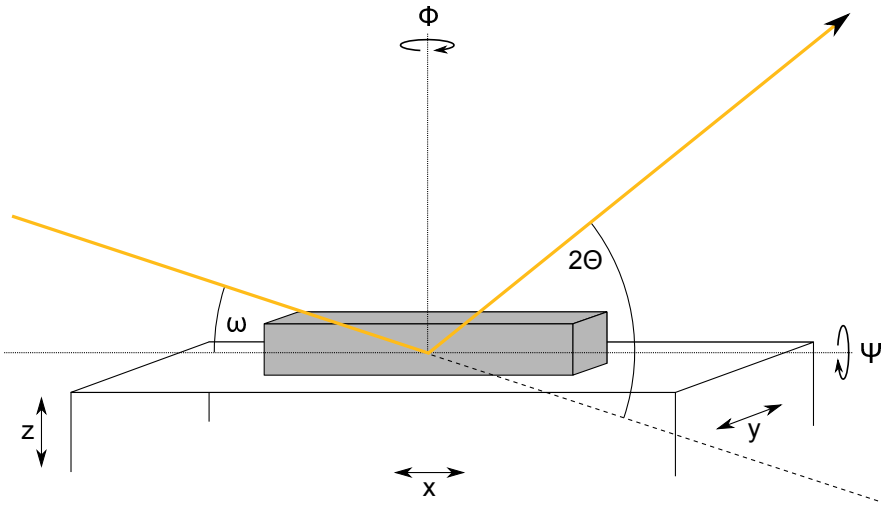

Figure 2.1: A scheme of an experimental arrangement of the diffraction experiment

A basic view of an measurement of the single-crystal diffraction is scanning of reciprocal space with positioning the detector and the sample, which is a single crystal. There is a scheme with the basic arrangement of the experiment in Figure 2.1.

The integrated intensity obtained from a mosaic single-crystal can be derived in the form:

$$\begin{aligned} I_{int}^{M} =& 8\pi^3 \left|A\right|^2 \left|F_{\vec{G}}\right|^2 \mathrm{e}^{-2M} \frac{S}{2Q_{i,z}} \left(1 - \mathrm{e}^{-2Q_{i,z}T}\right) \\ Q_{i,z} =& K\beta \left(\frac{1}{\sin\left(\omega\right)} + \frac{1}{\sin\left(2\Theta - \omega\right)}\right) \\ \left|A\right|^2 =& \left|Pr_{\mathrm{el}} \frac{\mathrm{e}^{\mathrm{i}KR}}{RV_{\mathrm{C}}}\right|^2 I_0 \end{aligned} \tag{2.4}$$

where $F_{\vec{G}}$ is the structure factor, e^{-2M} is the overall temperature Debye-Waller factor, which includes the decrease of the intensity due to thermal fluctuations of the atoms, S is the irradiated area of the sample, T is the width of the sample (in most cases of x-ray experiments is the term $\mathrm{e}^{-2Q_{i,z}T}$ negligible and we use $T \longrightarrow \infty$) V_C is the volume of the elementary unit, r_{el} the classical electron radius, P is the polarisation factor, K is the norm of the wave vector, β is the imaginary part of the refraction index. R is distance of the detector from the sample and I_0 is the intensity of the primary beam.

The values of 2Θ and ω are taken as the angular coordination of the diffraction maximum (the effect of the absortion correction is practically constant within the

integration of the intensity around one diffraction spot). The value of the polarisation factor can be computed as $P = \frac{1+\cos(2\Theta_M)\cos^2(2\Theta)}{1+\cos(2\Theta_M)}$, where Θ_M is a characteristic value of a monochromator (Θ_M is the Bragg angle of the used diffraction on a crystal in the monochromator). The value of S depends on a fact whether the cross-section of the incident beam is smaller than sample or not. If the beam is smaller, $S = \frac{S_B}{\sin\omega}$, where S_B is the cross-section of the incident beam. If the beam cross-section is bigger than the sample, the whole sample is irradiated always.

The structure factor can be written in the form:

$$F_{\vec{G}} = \sum_j \left(f_j(\Theta) + f_j'(\lambda) + \mathrm{i} f_j''(\lambda) \right) \mathrm{e}^{-\mathrm{i}\vec{G}\cdot\vec{R}_j} \tag{2.5}$$

where the sum goes over all atoms in the elementary unit. f_j, f_j' and f'' is the atomic scattering factor and its corrections respectively and $\vec{R}_j$ is the vector, which points to the individual atoms in the elementary cell.

A shape of a diffraction spot in reciprocal space corresponds to the Fourier transform of a crystal shape fuction $\Omega\left(\vec{R}\right)$ ($\Omega = 1$ inside of crystal and $\Omega = 0$ outside). If we have a small spherical crystal with the radius ρ, we can simply derive that Fourier transform is:

$$\Omega^{\mathrm{FT}}(q) = 4\pi\rho^3 \frac{\sin(q\rho) - q\rho\cos(q\rho)}{(q\rho)^3} \tag{2.6}$$

where $q = \left|\vec{Q} - \vec{G}\right|$ and $\vec{G}$ means diffraction vector (it points to a center of the diffraction spot). From previous, full width at highest maximum (FWHM) Δq can be numericaly estimated [27] approximately as:

$$\Delta q \approx \frac{3.63}{\rho} \tag{2.7}$$

As one can see, FWHM is independent on the diffraction vector. This statement will be valid in every case with a prefect crystal of any shape. Then, widths of diffraction spots along individual directions in reciprocal space will be inversely proportional to proportions of the crystal in direct space.

2.1.2 Laue method

This method is a basic way to obtain some information of a quality and of an orientation of the crystal in our sample. X-rays are screened by a small circular slit (diameter up to 1 mm) and they reach the sample in a goniometer. Diffracted beams are registred on a plane film or a plane detector, which is in a distance of 3-5 cm behind or before the sample (registration of the backscattered beams).

We use the whole spectrum of the wavelengths. Therefore, if the crystal in the sample has a random orientation, the Equation 2.1 or 2.2 is fulfilled for a lot of planes. If we want to interpret resulting Lauegrams, the diffractions from the planes corresponding to the same zone play an important role. The beams, which are diffracted by these planes, lay on a conical surface with the apex in the center of Ewald sphere. The cone intersects the plane film around an ellipse (the film is behind the sample) or around a hyperbola (the film is before the sample).

We can use this fact to find important axes of the symmetry. Then, we can rotate with the sample in the goniometer and set the important diffraction spot to the center of Lauegram. As a result, we have set the orientation of the crystal in the sample, because the corresponding crystallographic plane is perpendicular to the primary beam then.

If our sample is a good polycrystal, we will see diffraction circles in the Lauegram instead of the discrete diffraction spots.

2.1.3 Powder diffraction (XPD)

Powder sample is a pollycrystall, which contains a lot of single-crystalline grains with all possible orientations. Then, if we would scan reciprocal space properly, we cannot see the discrete diffraction spots. Every diffraction, which has the same corresponding 2Θ, will be merged to the one diffraction circle.

Now, we have two basic possible options to obtain the diffraction pattern. One can do a symmetric $2\Theta - \omega$ scan (but we obtain only information from the crystallites, which are oriented parallelly to the surface), or an asymmetric 2Θ scan with fixed ω angle, which is set to a small value. We can rotate the sample around Φ axis (see Figure 2.1) as well to eliminate effects of a possible texture (there can be some distribution of the orientation of the grains).

The resulting diffraction pattern contains an amount of information. From positions of diffraction peaks we can obtain the geometry of the lattice, some information of the macroscopic strain and qualitative information of the sample too. Each material has an original diffraction pattern, so if the sample contains more phases, the resulting pattern will be a superposition of the individual ones.

From the integrated intensities we can obtain some information about the structure of the lattice, some information of the texture and information for the quantitative phase analysis. The widths of the peaks contain information of the sizes of the coherently irradiated crystallites and about the microstrain. From shape parameters of the peaks we can obtain some information of the particle sizes and of the types of the crystallographic defects.

The value of the integrated intensities depend on a plenty of factors. In my work, it is suitable to work with the integrated intesities as the formula:

$$I_{hkl} = NVLP \left|F_{hkl}^2\right| m_{hkl} T_{hkl} \tag{2.8}$$

where N is the scale factor, V is the volume of the elementary cell, L is the Lorentz factor, P is the polarisation factor, F_{hkl} is the structure factor, m_{hkl} is the multiplicity of the diffraction and T_{hkl} is the influence of the texture. Other influences, such as the primary and secondary extinction, can be mostly neglected, because the grains in the powder are really small - extinction effects may be noticable in the nearly perfect or large mosaic crystals. In powder diffraction, extinction effects are often smaller than experimental errors.

For the powder diffraction experiment, the Lorentz factor is $L = \frac{1}{\sin(\Theta)\sin(2\Theta)}$. The multiplicity m_{hkl} has to be counted in, because several diffractions with the same 2Θ value can lay on the same diffraction circle. For example, if we have cubic crystallographic system, the diffraction $h00$ has the multiplicity 6, because $h00$, $0h0$, $00h$, $\overline{h}00$, $0\overline{h}0$ and $00\overline{h}$ have the same Bragg angle. The multiplicities for all crystallographic systems can be found in [25]. Texture factor T_{hkl} reflects

the fact that some of the planes in the powder might be preferably oriented. T_{hkl} is then considered as a density function of the vectors hkl around the diffraction circle. For example, if there is a preferable orientation 100, all set of diffractions $h00$ is affected.

In the case of the powder diffraction experiment, the structure factor 2.5 can be rewritten in the following form:

$$F_{hkl}(\Theta) = \sum_j o_j \left(f_j(\Theta) + f_j'(\lambda) + \mathrm{i} f_j''(\lambda) \right) \mathrm{e}^{-2\pi \mathrm{i}(hx_j + ky_j + lz_j)} \mathrm{e}^{-M_j(\Theta)} \tag{2.9}$$

where the sum goes over all atoms in the elementary unit. The o_j are the occupancies of the individual atomic sites, f_j, f_j' and f'' is the atomic scattering factor as in the Equation 2.5, x_j, y_j and z_j are the fractional coordinates of the j-th atom in the elementary unit and e^{-M_j} is the temperature Debye-Waller factor of the j-th atom. The most common approximation is to use one overall Debye-Waller factor for every atom, or we use one Debye-Waller factor for each individual type of atom in the elementary unit. Another way is to consider Debye temperature - Debye-Waller factors are then dependent on it and inversely proportional to an atomic mass. The corresponding formula (see [26]) is:

$$\begin{aligned} M_j &= B_T^j \left(\frac{\sin\Theta}{\lambda} \right)^2 \\ B_T^j &= \frac{6h^2}{m_A^j k_B \Theta_D} \left(\frac{\Phi(\Theta_D/T)}{\Theta_D/T} + \frac{1}{4} \right) \end{aligned} \tag{2.10}$$

where h is Planck constant, k_B is Stefan-Boltzmann constant, m_A^j is the atomic mass corresponding to j-th atom, T is a temperature, Θ_D is Debye temperature and $\Phi(x)$ is Debye integral, which is given by $\Phi(x) \equiv \frac{1}{x} \int_0^x \frac{\xi}{e^\xi - 1} \mathrm{d}\xi$.

For the processing of the measured diffraction patterns I use *FullProf* [28], which is the program for the Rietveld analysis. Rietveld refirement fits a whole pattern and it has several steps. The first of them is indexing the diffractions and involves finding the unit cell size and symmetry. The second step is to extract the measured intensities and convert them into structure factors. In the third step, the measured structure factors are used to build a structural model.

2.1.4 EDX

Energy-dispersive X-ray spectroscopy (EDX) is an analytical technique used for an elemental analysis or a chemical characterization of the sample. We use a high-energy beam of charged particles or a beam of x-rays to stimulate the sample.

The electrons in the sample are excited from inner electron shells. When the electron is ejected, an electron hole occurs where the electron was. Because everything goes to a state of the minimal energy, an electron from an outer, higher-energy shell then fills the hole, and a difference in the energy between the higher-energy shell and the lower-energy shell may be released in a form of x-rays.

Each element has a unique atomic and electron structure, which leads to a unique set of peaks in x-ray emission spectrum. A study of the resulting x-ray spectrum allows us to determine the chemical composition of the sample.

The accuracy of EDX spectrum can be affected by that fact that many elements have overlapping peaks. The other thing is that outcoming x-rays are emitted in any direction, so any of them may not escape from the sample. This fact can reduce the accuracy in inhomogeneous and rough samples.

2.1.5 EXAFS

EXAFS is an abbreviation from Extended X-rays Absorption Fine Structure, which indicates the measurement of a fine structure of the intensity of a transmitted radiation behind the absorption edge with respect to the wavelength of the incident radiation. We cannot manage this experiment with a common x-ray lamp in a laboratory, because common x-ray lamp is a monochromatic source. Therefore, we have to use synchrotron radiation, which is suitable for the wavelength tunning.

As it was said in the previous EDX section, each element has an unique electron structure. This fact leads to a characteristic position of the absorption edges. The position corresponds to an amount of energy, which is necessary to add to the electron to overcome his binding energy and hit it out from the atomic shell into a vacuum. According to a type of electron, we can label the individual edges with letters and numbers. The letter corresponds to the shell, from which the electron is hit out (it means the principal quantum number n). For $n = 1, 2, \ldots$ the corresponding letters are $K, L, M, \ldots$. Beside this, the number, which follows the letter, corresponds to the orbital quantum number l. It can acquire the values $l = -n, -n+1, \ldots, n-1, n$. According to this, we assign the numbers 1 up to $2n-1$ in the label of the absorption edge.

So, there can be absorption edges like $K, L_1, L_2, L_3, M_1, M_2, M_3, M_4, M_5, \ldots$ in the absorption spectrum. The positions of the absorption edges can be theoretically derived in the simplest cases, such as hydrogen-like atom. Moseley's law says:

$$\sqrt{\frac{\nu_n}{R}} = \frac{Z - \sigma}{n}, \tag{2.11}$$

where ν_n is frequency corresponding to the position of absorption edge, R is Rydberg's constant, Z is the atomic number of the corresponding element, n is the principal quantum number and σ is screening constant, which reflects the screening of the rest of the electrons.

The positions of the absorption edges are tabelated, see for example [29]. In my work, I used the software *Demeter* [14], [30] to process the resulting EXAFS data. *Demeter* includes the program *Hephasteus*, which is a database with the positions of the absorption edges.

We can obtain the EXAFS data from the intensity of transmitted or fluorescence radiation. The structure of a signal behind the absorption edge can for example look like that one in Figure 2.2. As the proper EXAFS data we take the quantity $\chi(k)$, which is defined as:

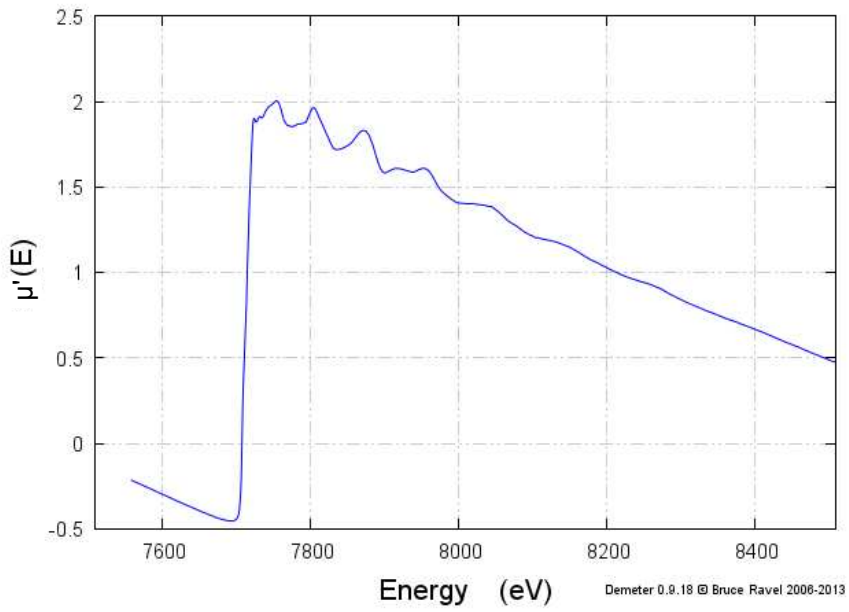

Figure 2.2: The normalized absorption coefficient obtained from the measurement is depicted here. The sample contains cobalt and the data are measured at the edge CoK, $E_{\mathrm{Co}K} = 7709$ eV. If we use the transmission data, we obtain the μ' as $\mu' \sim \ln \frac{I_0}{I_{trans}}$, where I_0 is the intensity of the incident beam and I_{trans} is the intensity of the transmitted one. If we use fluorescence data, then $\mu' \sim \frac{I_{fluo}}{I_0}$, where I_{fluo} is the intensity of the fluorescence radiation.

$$\chi(k) = \frac{\mu'(k) - \mu_0(k)}{\Delta\mu_0}, \quad k = \frac{\sqrt{2m_e(E - E_0)}}{\hbar} \tag{2.12}$$

where μ' is the measured signal, μ_0 is a smooth function equivalent to the absorption on the isolated atom, $\Delta\mu_0$ is the jump in the signal at the energy E_0 of the absorption edge and m_e is the mass of the electron.

The physical principle of the fine structure in the signal is following. An (photo)electron is emitted due to the hit with the photon from the incident x-ray beam. We can consider the electron like a spherical wave, which spreads from an absorbing atom - this wave is scattered on neighboring atoms as well. An interference between this spherical wave and waves backscattered from the neighboring atoms results in a modulations of the signal behind the absorption edge.

The wavelegnth corresponding to the emitted photoelectron depends on the energy of the incident radiation, the phase and the amplitude of the backscattered waves depends on the type of the neighboring atoms and their distance from the central absorbing atom (we call it *the core*). Therefore, we can obtain some information about the chemical composition of the closest neighborhood of the absorbing atom and information about its arrangement too.

A contribution to the resulting singal differs according to the directions, in which the photoelectron goes, and from which of the atoms is the photoelectron scattered - we call this *a scattering path* Γ. The resulting signal is a sum over individual scattering paths. A number of the paths is very big, but contributions of most of them are negligible. In most cases, we can count in only a few

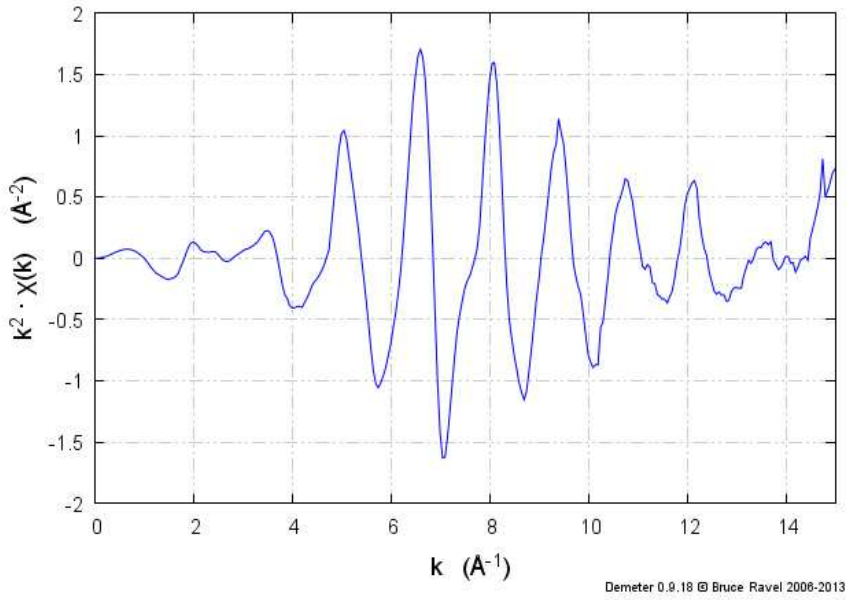

Figure 2.3: Here is the function 2.12 obtained from the data in Figure 2.2. The data is often weighted with a norm of the wave vector k to highlight small modulations in higher energies.

types of them:

- single scattering paths
- collinear or nearly collinear multiple scattering paths
- very short triangle paths

This is because the scattering amplitude is quite small far from 0° or 180°. A derivation of a theoretical shape of the function $\chi(k)$ can be found for example in [31]. The contribution of the single scattering path Γ can be obtain as:

$$\chi_\Gamma(k) = \frac{N_\Gamma S_0^2 F_\Gamma}{kR_\Gamma^2} \mathrm{e}^{-2\sigma_\Gamma^2 k^2} \mathrm{e}^{-2\frac{R_\Gamma}{\lambda(k)}} \sin(2kR_\Gamma + \Phi_\Gamma) \tag{2.13}$$

where N_Γ is the multiplicity of the path, S_0 is the passive electron amplitude reduction factor, F_Γ is the effective scattering amplitude, R_Γ is the half path length, σ_Γ is the mean squared displacement, which can be caused for example by the thermal fluctuations, $\lambda(k)$ is the mean free path of the electron and Φ_Γ is the effective phase shift. The k is the wave vector from Equation 2.12.

F_Γ, Φ_Γ and $\lambda(k)$ are the parameters, which are generated with the ab initio multiple scattering calculation from the program (*FEFF* in our case) after we have entered the structure of the elementary unit. R_Γ, σ_Γ, N_Γ, S_0 and E_0 are the objects of our interest and we fit them.

2.2 Preparation of the samples

In my work, I am dealing with the samples of different kind of origin. I will describe a system of a preparation of our samples in this section.

2.2.1 Powder samples

If we want to prepare a powder sample, we have to prepare a polycrystal of a required material. At first we have to weight a correct amount of the materials, which corresponds to the stoichiometry of our required samples. Secondly, we have to melt the materials together in a furnace.

I have used *monoarc furnace* in our department. The main part of *monoarc* consists of an evacuable chamber, a crucible made from a copper and a tungsten electrode. We have to evacuate the whole chamber before melting to prevent the burning of atmospheric oxygen - the pressure of value $10^{-9} - 10^{-10}$ bar has been achieved. After the evacuation, we have pumped some high purity argon inside the chamber as a protective atmosphere - the pressure of argon in the chamber was set approximately to 0.3 bar.

If we bring sufficiently big voltage to the electrode, an electric discharge occurs in the gas of the protective atmosphere in the chamber. The temperature of the discharge is able to melt the materials in the crucible. We have to proceed slowly and carefully during the melting, because for example quick temperature jump might lead to a sputter of the materials outside the crucible. We repeated the melting three or four times to obtain a homogeneous element distribution throughout the sample and we have obtained a polycrystalline button as the result.

If we have compound, which consists of more elements, some troubles may occur. We have to decide, if we can melt all elements together or melt them gradually. Then, we must study some phase diagrams, find some information about melting points of our elements and so on. There are some databases of phase diagrams, which can be found for instance on [32] or in [33, 34].

In my case, I wanted to prepare the compound Mn_2CoSn. Therefore, I have melted manganese together with tin firstly because of high manganese sublimation. Tin has the melting point only at 232°C, so it has covered the manganese pieces and it has reduced the manganese sublimation during the melting. So, Mn_2Sn has been prepared at the first step and then I have melted it together with cobalt.

Polycrystalline buttons obtained by the preparation mentioned above has been grinded to a powder to use them in powder diffraction.

2.2.2 Single-crystalline samples

For the attempts of the single crystals growth we need a polycrystalline sample prepared by the previous method. I have tried two methods of a single crystal preparation.

Czochralski method

This method has its name after Polish scientist Jan Czochralski, who invented it in 1916. This method is mostly used to obtain single crystals of semiconductors, metals and synthetic gemstones. A principle is in pulling of the seed from the melted material. On the interface between a melted material and a seed is a place with the temperature gradient and there the material crystalizes.

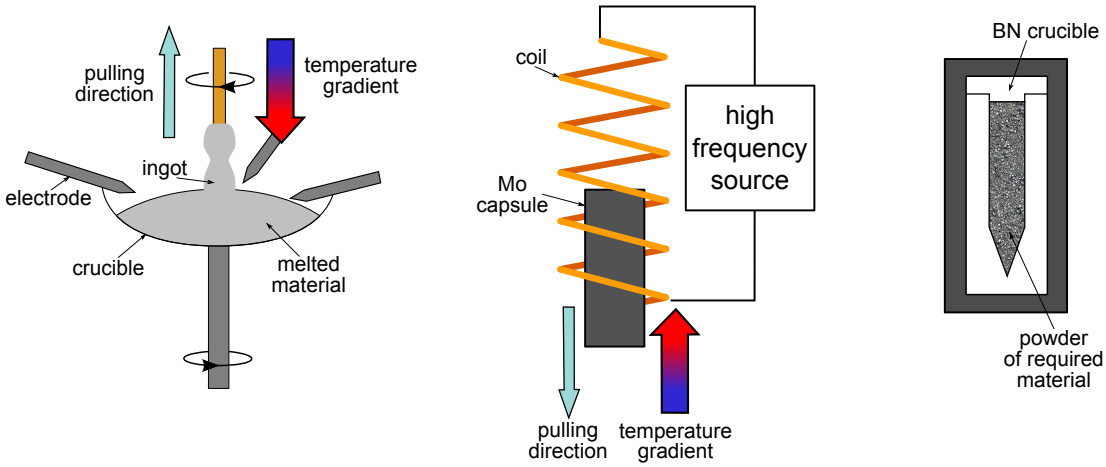

(a) Czochralski method

(b) Bridgmann method

(c) the cut of the molybdenum capsule

Figure 2.4: The basic scheme of Czochralski and Bridgmann method is depicted in this figure.

The experimental arrangement is depicted in Figure 2.4a. In our case we used *triarc*, which has three electrodes for the melting and a crucible, which can rotate to obtain better homogenity of the melted material. We have used argon as the protective atmosphere as in previous case. It is important to do a neck on the ingot. It is the place on the ingot, where the width is several times smaller - the actual width during the crystal growth is regulated by a current on the electrodes and the pulling speed, which was set to 8 $\frac{\text{mm}}{\text{h}}$. The crystal defects will be accumulated in the neck and a rest of the ingot should be without them.

Unfortunately, my attempt of a growth of the single crystal of Mn_2CoSn was unsuccessful. The optimal current on the electrodes was set only at approximately 8 A - this fact indicates a quite small melting point of our material. As we found out from the Laue patterns, the resulting ingots were neither single crystals nor good polycrystals (the diffraction circles were absent in the Laue patterns).

Bridgmann method

In this method, we let go the temperature gradient through the whole crucible of our material. We have used the experimental arrangement as it is shown in Figure 2.4b. We achieve a high temperature with an induction furnace. It contains the coil, which is connected to the a frequency source. Our material is sealed in a molybdenum capsule, which is a very good temperature conductor. Due to Foucault eddy currents, which are induced by a changing magnetic field of the coil, the temperature of the capsule is growing. Because only the part of the molybdenum capsule inside the coil is heated and the part outside is not, the temperature gradient occurs. So, if we pull the capsule outside the coil, the material inside crystalizes.

A cut of the molybdenum capsule is depicted in Figure 2.4c. Our material in a form of powder is closed in a boron nitride (BN) crucible. Boron nitride

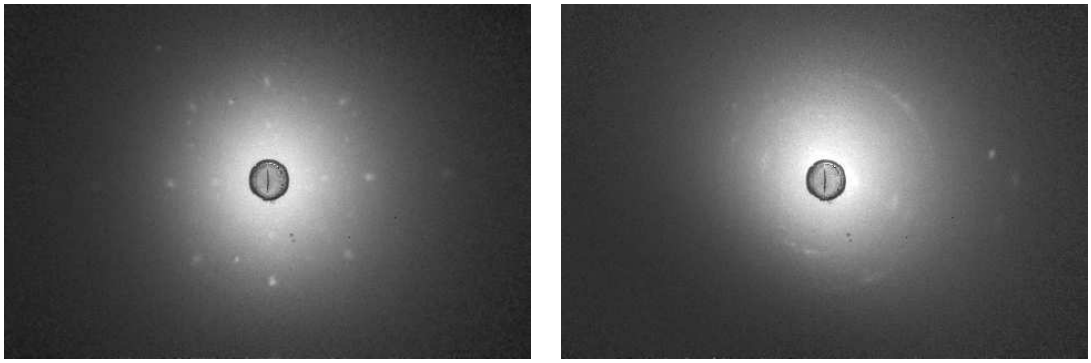

(a) Before annealing (b) After annealing

Figure 2.5: The Lauegrams before and after annealing.

is used because of its very low reactivity with other materials. The function of the neck (like in Czochralski method) is fullfilled with a shape of the inside of boron nitride crucible - a bullet shape mostly.

I have performed several attempts of growing single-crystals by Brigmann method. The pulling speed in individual attemps was set from 1 to 5 $\frac{\text{mm}}{\text{h}}$ and the voltage on the source was at 130-140 V (it corresponds to approximately 900-950°C on the molybdenum capsule; the melting point of Mn_2CoSn has been estimated as 850°C by differential thermal analysis). My attempts of growing single crystal of Mn_2CoSn by Brigmann method were more successful than by Czochralski method. There is the Laue pattern of the best attempt in Figure 2.5a. You can see that the diffraction maxima are not very sharp, so I have decided to anneal the sample. The sample was annealed for 3 days at the temperature 600°C (the melting point is at 850°C). Unfortunately, the sample became to be polycrystalline - you can see the circles in the Laue pattern in Figure 2.5b.

2.2.3 List of the used samples

chemical formula	**form**	**created / supported by**
Mn_2CoSn	powder	Petr Cejpek[1)]
$Mn_2Co_{0.7}Rh_{0.3}Sn$	powder	Olga Meshcheriakova[2)]
$Mn_2Co_{0.6}Rh_{0.4}Sn$	powder	Olga Meshcheriakova
$Mn_2Co_{0.5}Rh_{0.5}Sn$	powder	Olga Meshcheriakova
$Mn_2Co_{0.3}Rh_{0.7}Sn$	powder	Olga Meshcheriakova
$Mn_2Co_{0.2}Rh_{0.8}Sn$	powder	Olga Meshcheriakova
$Mn_2Co_{0.1}Rh_{0.9}Sn$	powder	Olga Meshcheriakova
Mn_2RhSn	powder	Olga Meshcheriakova
Ni_2MnGa	single crystal, bulk	Oleg Heczko[3)]

Table 2.1: The list of the samples, which I have studied. [1)]Charles University in Prague, [2)]Max Planck Institute for Chemical Physics of Solids in Dresden, [3)]Academy of Science in Prague.

There is the list of the samples, which I have studied in my work, in Table 2.1.

3. Powder diffraction and EDX on series $Mn_2Co_{1-x}Rh_xSn$

3.1 EDX

The first part of samples to study was the series $Mn_2Co_{1-x}Rh_xSn$. The samples were prepared as polycrystalline buttons. One part of them was grinded to powder in order to powder diffraction. In this chapter I will show the results of EDX and XPD measurement.

The EDX meassurement has been done to determine an exact relative concentration of the elements in our samples. The measurement has been performed

Element	w [%]	x	x_n		Element	w [%]	x	x_n
sample Mn_2CoSn					**sample $Mn_2Co_{0.7}Rh_{0.3}Sn$**			
Co	21.92	0.277	1.101		Co	14.11	0.178	0.753
Mn	37.13	0.444	2.000		Mn	34.94	0.472	2.000
Rh	0.00	0.000	0.000		Rh	10.15	0.073	0.310
Sn	40.95	0.248	1.021		Sn	40.23	0.252	1.066
O	not measured				O	0.52	0.024	0.102
Si	not measured				Si	0.05	0.001	0.006
sample $Mn_2Co_{0.4}Rh_{0.6}Sn$					**sample $Mn_2Co_{0.5}Rh_{0.5}Sn$**			
Co	12.04	0.153	0.649		Co	9.20	0.117	0.525
Mn	34.59	0.472	2.000		Mn	32.70	0.446	2.000
Rh	13.01	0.095	0.402		Rh	16.90	0.123	0.552
Sn	39.69	0.250	1.062		Sn	39.70	0.251	1.124
O	0.61	0.029	0.121		O	1.30	0.061	0.273
Si	0.07	0.002	0.009		Si	0.10	0.003	0.012
sample $Mn_2Co_{0.3}Rh_{0.7}Sn$					**sample $Mn_2Co_{0.2}Rh_{0.8}Sn$**			
Co	5.56	0.071	0.324		Co	3.93	0.053	0.221
Mn	32.01	0.441	2.000		Mn	33.13	0.478	2.000
Rh	22.15	0.163	0.739		Rh	24.96	0.192	0.804
Sn	38.60	0.246	1.116		Sn	37.45	0.250	1.046
O	1.61	0.076	0.345		O	0.51	0.025	0.106
Si	0.08	0.002	0.010		Si	0.06	0.002	0.007
sample $Mn_2Co_{0.1}Rh_{0.9}Sn$					**sample Mn_2RhSn**			
Co	1.85	0.024	0.107		Co	0.01	0.000	0.001
Mn	32.26	0.456	2.000		Mn	32.74	0.481	2.000
Rh	27.66	0.209	0.915		Rh	28.93	0.227	0.943
Sn	36.76	0.241	1.055		Sn	37.56	0.255	1.062
O	1.40	0.068	0.298		O	0.71	0.036	0.149
Si	0.07	0.002	0.008		Si	0.05	0.001	0.006

Table 3.1: The results of the EDX measurement. The measured values are the weight percents w, x are molar fractions and x_n are molar fractions which are normalized to the theoretical content of Mn (it should be 2).

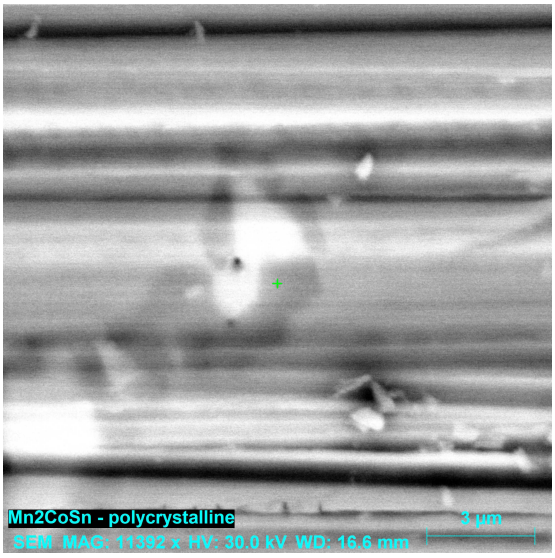

Figure 3.1: An inclusion seen by EDX. The measurement under the green cross shows weight percents 44.90% (Mn), 12.88% (Co) and 42.27% (Sn), which correspond to the normalized composition (see Table 3.1) 2:0.53:0.87.

on the microscope Tescan MIRA I LMH SEM, which is equiped with the energy dispersive analyser Bruker AXS. We managed the measurement on non-grinded polycrystalline samples. The results are shown in Table 3.1. We use a high-energy electron beam for a sample stimulation. Because the beam has a small finite size, we measure a chemical composition of the sample under a spot of the electron beam. One can see, that EDX shows a presence of silicon and oxygen. Silicon could appear here due to polishing on a sandpaper, oxygen may appear due to an oxidation. Deviations of the measured weight factors are in a range of several percents.

From Figure 3.1 it can be seen that the sample Mn_2CoSn contains some inclusions, which contain less amount of cobalt. It corresponds to the composition 2:0.53:0.87.

3.2 Powder diffraction

XPD meassurements have been performed on two x-ray wavelengths - CuKα (λ = 1.54056 Å) and CoKα line (λ = 1.788965 Å). CoKα line lies under Co absorption edge (see Figure 3.2) and it may help to determine the Co atoms position. I managed the measurement in the Bragg-Brentano geometry (symetric 2Θ-ω scan) on the diffractometer Bruker D8 Advance and Seifert-FPM, XRD-7. The resulting data were processed by *FullProf* at first to obtain lattice parameters.

Because Mn is more electropositive than Co, Mn_2CoSn is an inverse Heusler compound. Therefore, I have chosen the space group $F\overline{4}3m$ for a description of the symetry of the samples (see Section 1.1). The pseudo-Voight function has been chosen as the resolution function.

I have found that the samples with $x^{th}_{\mathrm{Rh}} \leq 0.3$ (a theoretical Rh content) are cubic, the other samples with $x^{th}_{\mathrm{Rh}} \in (0.3, 1]$ are tetragonal. Corresponding space

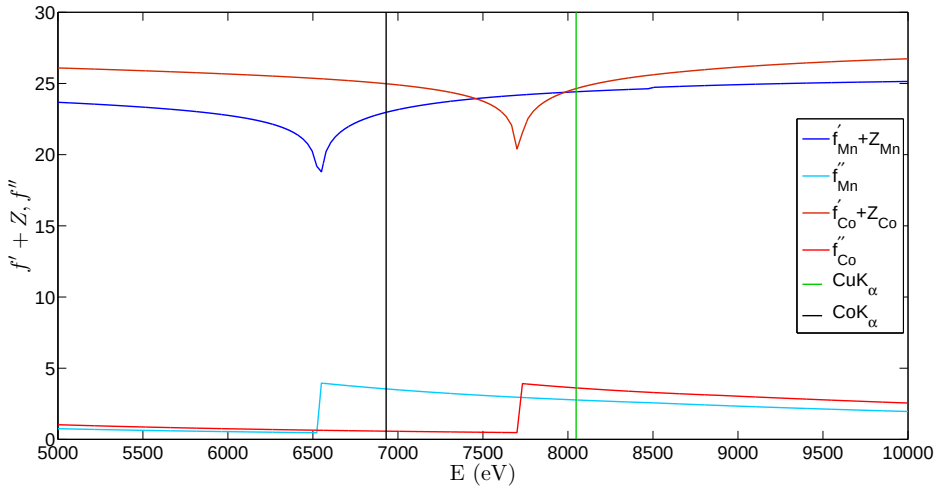

Figure 3.2: The dispersion correction of the Mn and Co scattering factors. The positions of CuKα and CoKα energies are depicted here as well. One can see that the real parts of the scattering factors are almost equal at the CuKα, so we cannot distinguish practically the Co and Mn atoms only from the results of XPD on CuKα.

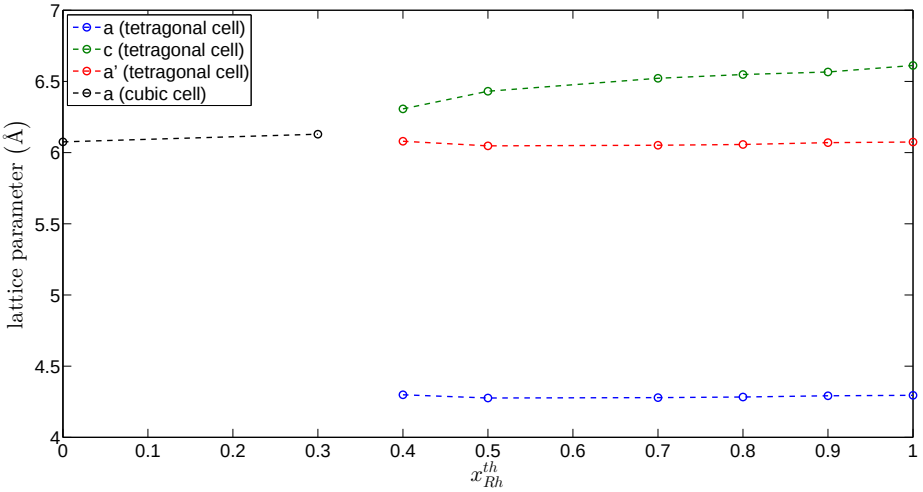

Figure 3.3: A dependence of the lattice parameters on amount of Rh in the samples. a' is a value of a multiplied by $\sqrt{2}$ - the original cubic cell is rotated around c axis by 45° with respect to a corresponding tetragonal cell. Therefore, a' corresponds to a lattice parameter of the cubic cell, whose base is circumscribed to the base of the corresponding tetragonal cell. The error bars are so small that they are not visible in this figure.

x^{th}_{Rh}	a [Å]	c [Å]
0.0	6.075 ± 0.001	-
0.3	6.129 ± 0.002	-
0.4	4.299 ± 0.002	6.307 ± 0.003
0.5	4.276 ± 0.002	6.431 ± 0.003
0.7	4.279 ± 0.002	6.522 ± 0.003
0.8	4.283 ± 0.002	6.548 ± 0.003
0.9	4.292 ± 0.003	6.566 ± 0.005
1.0	4.295 ± 0.003	6.612 ± 0.005

Table 3.2: The lattice parameters obtained from the Rietveld analysis in dependence of theoretical content of rhodium (x^{th}_{Rh})

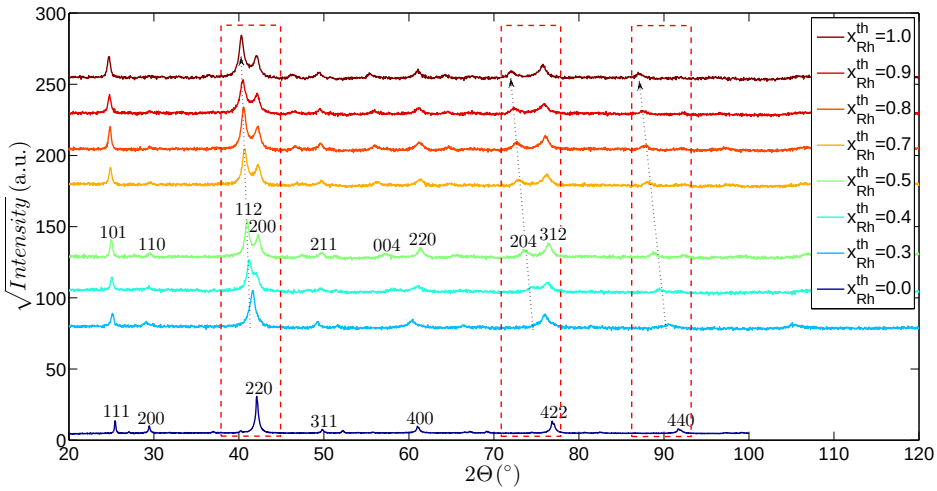

Figure 3.4: The XPD patterns measured with CuKα wavelength. Indices of some of the strongest diffractions are labeled here as well. One can see shifts of some diffraction corresponding to a change of the lattice parameters (highlighted in the red rectangles).

group, which describes the tetragonal distorted structure, is $I\overline{4}m2$ (see for example [2, 12]). The resulting lattice parameters are shown in Table 3.2 and plotted in Figure 3.3. All XPD patterns, which were measured with CuKα wavelength, are ploted in Figure 3.4. One can see a split of the diffraction peak 220 (cubic phase) to the diffraction peaks 200 and 112 (tetragonal phase). A comparison of the measured patterns ($x^{th}_{\mathrm{Rh}} = 0.9$) using CuK$\alpha$ and CoKα lines are pltoted in Figure 3.5.

type of disorder	missing distinct peaks
BiF_3	-
CsCl	111, 311, 331
NaTl	200, 222, 420
W	111, 200, 311, 222, 331, 420, 333, 511

Table 3.3: Distinct diffraction peaks missing in XPD patterns corresponding to the individual types of occupation disorder.

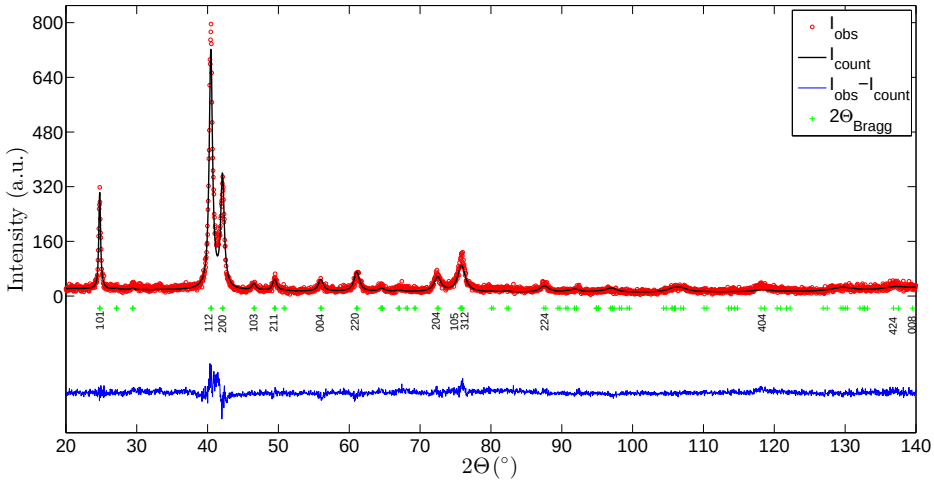

(a) Measured with CuKα

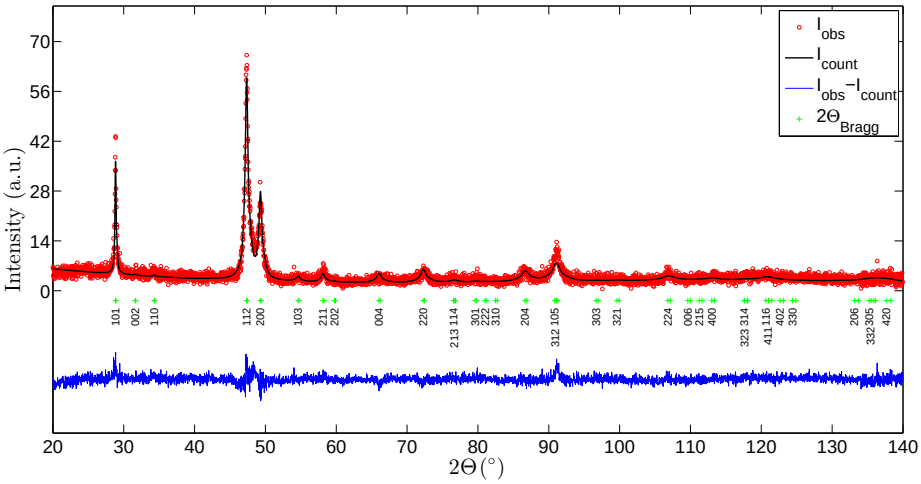

(b) Measured with CoKα

Figure 3.5: The XPD patterns measured with CuKα and CoKα wavelength on the sample with $x^{th}_{\mathrm{Rh}} = 0.9$.

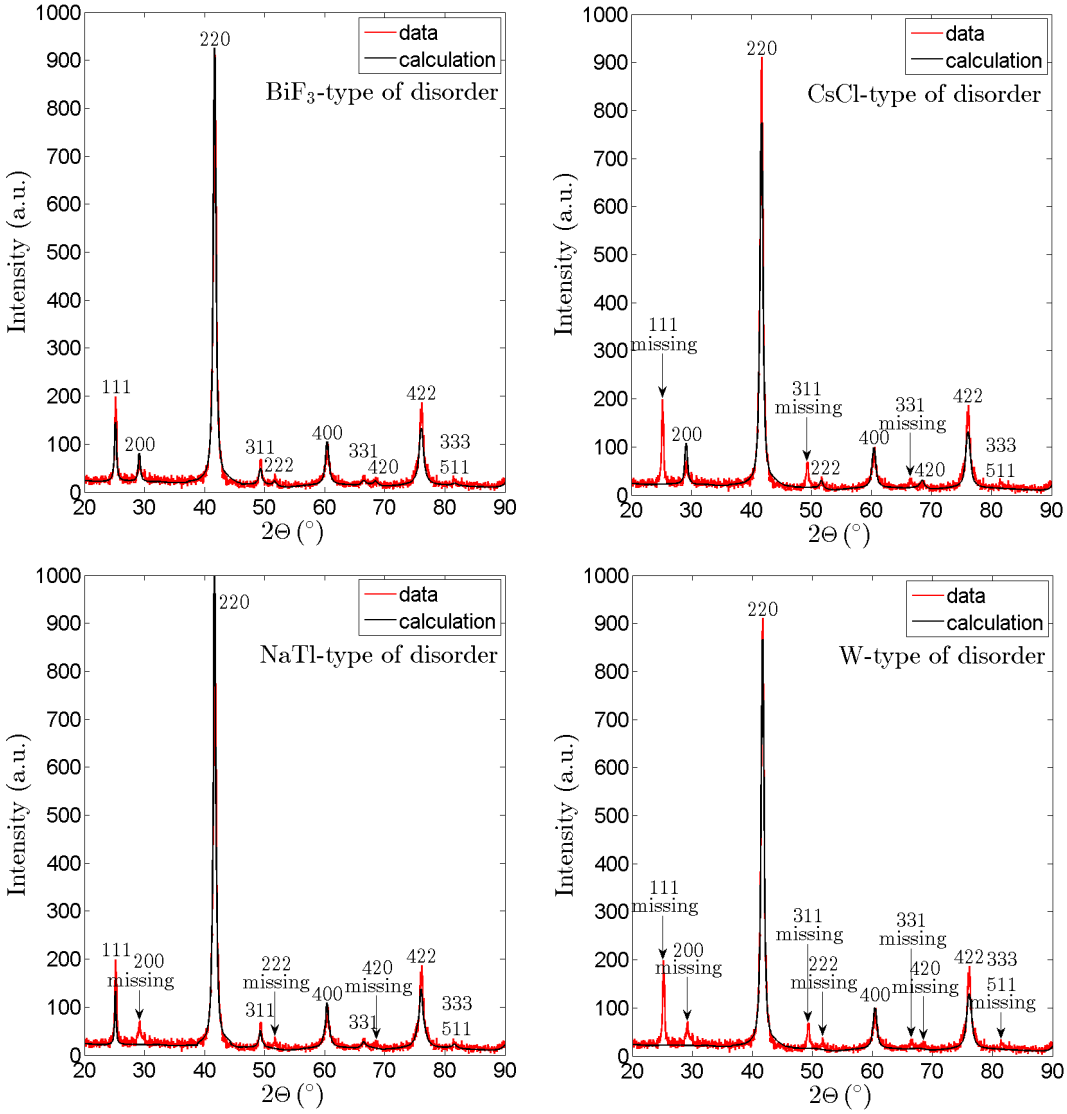

Figure 3.6: The XPD patterns generated from different types of the occupation disorder. There is a comparison with the XPD pattern measured with the CuKα wavelength on the sample with $x_{\mathrm{Rh}}^{th} = 0.3$.

Because a consideration of the structure belonging to the basic parent phase (see Section 1.1) was not able to fit the resulting patterns properly (see Figure 3.5), a consideration of some occupation disorder was necessary. I have considered four disorder types, which are described in Section 1.2. We can exclude a presence of some of them even only with a quick observation of the diffraction patterns. Some diffraction peaks disappear due to the different structure and symmetry of the disordered unit cell. The diffraction patterns generated from the disordered types of structure are ploted in Figure 3.6 for the sample with $x^{th}_{\mathrm{Rh}} = 0.3$. One can see that here we can exclude the CsCl, W, and NaTl-type of disorder, because the corresponding profiles do not contain some peaks, which are in the measured patterns. The missing diffraction peaks for the individual types of disorder are shown in Figure 3.6 and summarized in Table 3.3.

The next procedure to obtain some information about the atomic sites occupation was following - *FullProf* allows the fitting of more diffraction pattern together. Each pattern has its own set of parameters, but they can be bounded mutually (because we have one structure, we need only one set of parameters for it). From previous considerations about the missing peaks due to the disorder, it follows that the structure might be BiF_3-type disordered or it might be in some state between the non-disordered and fully disordered structure.

Unfortunately, it was not possible to obtain exact values of occupation numbers of all atomic sites by a classical Ritveld analysis by least squares method. There was a lot of parameters to fit and the occupation numbers could be strongly corelated with Debye-Waller factors. Therefore, another method was taken to process the data. I have obtained integrated intensities by *FullProf* from the measured XPD profiles and I have fitted them to their theoretical formula 2.8 only with the scale and the Debye temperature as free parameters; the occupation numbers were changed manually. The change of the occupation numbers was with the step of 0.1, smaller values would not have visibile effects. I have chosen such a combination of the occupation numbers, which leads to the smallest residuum, as the final result. For this fitting, I have written my own script in *MatLab*, which can be found in the appendix and attachment.

The script generates a specified number of elementary units with the different occupation numbers for each atom at each atomic site. The space group is specified as $P1$ here, so one obtains the occupation numbers of each atom in all 16 position corresponding to one unit cell (4 types of atoms lead to the 64 occupation numbers). The integrated intensity is than computed by Equation 2.8. The patterns measured on the CuKα and the CoKα lines are then fitted together. A result of the script is a list of combinations of the occupation numbers with their corresponding residua after the fit. An influence of a texture is not considered - from the measured patterns it seems that noone set of the mutually corresponding diffractions has distinctly bigger or smaller intensities.

But the minimum of the sum of the deviations from the fit is not so deep. I have obtained similar values of a residuum with different combinations of the occupation numbers or only by a swap of atomic sites of individual atoms (especially Mn and Co, because they have simillar number of electrons). There are combinations leading to the two smallest residui for the sample with $x^{th}_{\mathrm{Rh}} = 0.3$ in Table 3.4. A comparison of the integrated intensities, which were obtained from the messurement, and the integrated intensities, which correspond to sim-

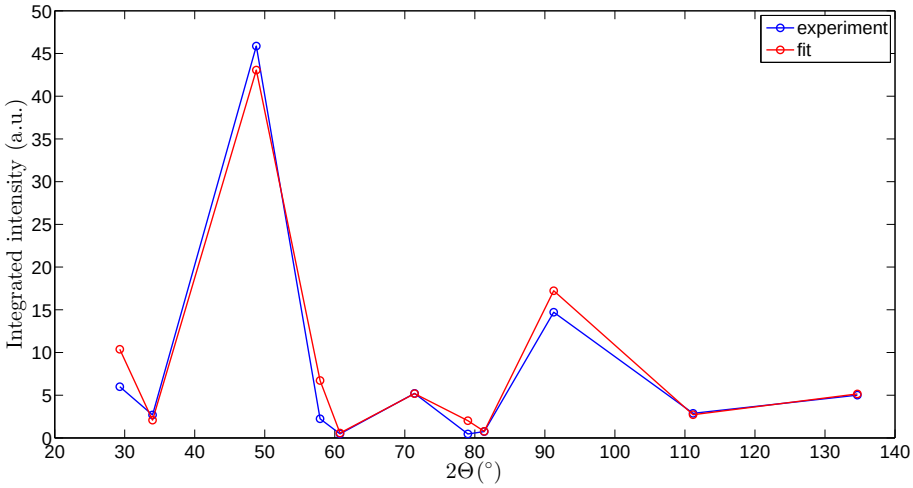

(a) A fit of the integrated intensities with a consideration of the sample with $x_{\mathrm{Rh}}^{th} = 0.3$, which has its unit cell without disorder.

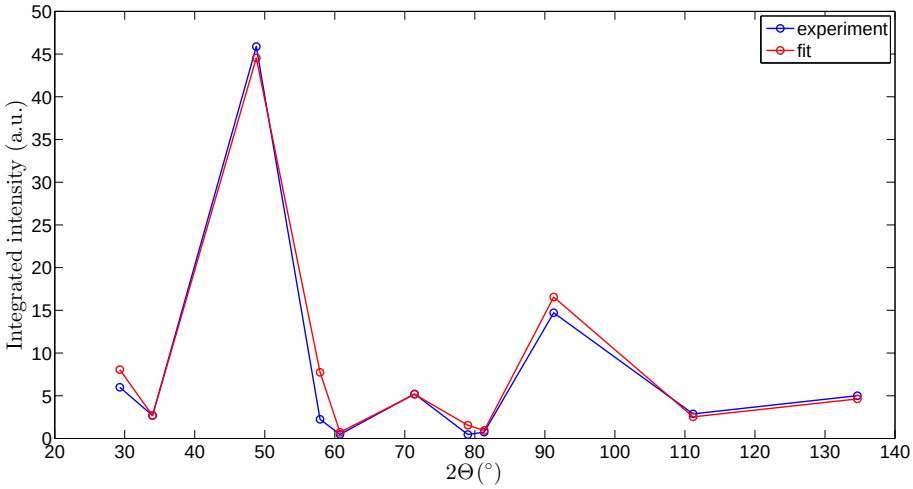

(b) A fit of the integrated intensities with a consideration of the sample with $x_{\mathrm{Rh}}^{th} = 0.3$, which has its unit cell with the BiF_3-type of occupation disorder - a many of the unit cells with different combinations of the occupation numbers were generated by a computer. The combination, which led to the smallest residuum after the fit, was taken as a result.

Figure 3.7: The comparison of the measured and the computed integrated intensities from XPD patterns on the sample with $x_{\mathrm{Rh}}^{th} = 0.3$ measured with CoKα line.

site	without disorder				disorder sim. (1st SR*)				disorder sim. (2nd SR*)			
	occ_{Mn}	occ_{Sn}	occ_{Co}	occ_{Rh}	occ_{Mn}	occ_{Sn}	occ_{Co}	occ_{Rh}	occ_{Mn}	occ_{Sn}	occ_{Co}	occ_{Rh}
0,0,0	0	1	0	0	0	1	0	0	0	1	0	0
$\frac{1}{2},\frac{1}{2},0$	0	1	0	0	0	1	0	0	0	1	0	0
$0,\frac{1}{2},\frac{1}{2}$	0	1	0	0	0	1	0	0	0	1	0	0
$\frac{1}{2},0,\frac{1}{2}$	0	1	0	0	0	1	0	0	0	1	0	0
$\frac{1}{2},\frac{1}{2},\frac{1}{2}$	1	0	0	0	0	0	0.5	0.5	1	0	0	0
$\frac{1}{2},0,0$	1	0	0	0	0.8	0	0	0.2	0.6	0	0.4	0
$0,\frac{1}{2},0$	1	0	0	0	0.7	0	0.2	0.1	0	0	0.2	0.8
$0,0,\frac{1}{2}$	1	0	0	0	0.9	0	0.1	0	1	0	0	0
$\frac{1}{4},\frac{1}{4},\frac{1}{4}$	0	0	0.7	0.3	0.9	0	0	0.1	0	0	0.8	0.2
$\frac{3}{4},\frac{3}{4},\frac{1}{4}$	0	0	0.7	0.3	0.8	0	0.2	0	0.9	0	0.1	0
$\frac{1}{4},\frac{3}{4},\frac{3}{4}$	0	0	0.7	0.3	0.8	0	0	0.2	0.2	0	0.6	0.2
$\frac{3}{4},\frac{1}{4},\frac{3}{4}$	0	0	0.7	0.3	0.3	0	0.7	0	0.8	0	0.2	0
$\frac{3}{4},\frac{3}{4},\frac{3}{4}$	1	0	0	0	0.1	0	0.9	0	0.7	0	0.3	0
$\frac{1}{4},\frac{1}{4},\frac{3}{4}$	1	0	0	0	1	0	0	0	1	0	0	0
$\frac{3}{4},\frac{1}{4},\frac{1}{4}$	1	0	0	0	1	0	0	0.1	0.9	0	0.1	0
$\frac{1}{4},\frac{3}{4},\frac{1}{4}$	1	0	0	0	0.8	0	0.2	0	0.9	0	0.1	0
residuum	100.261				42.877				43.142			

Table 3.4: The occupation numbers obtained from the simulation for the sample with $x^{th}_{\mathrm{Rh}} = 0.3$. **the smallest residuum.*

ulation with the smallest residuum after fit, is ploted in Figure 3.7. It can be seen from Table 3.4 that change about 0.3 (without respect to the swapping of the individual atomic sites) in the resulting values of the occupation numbers makes no distinct change in the value of residuum. Therefore, the error in the estimation of the resulting occupation numbers is roughly 0.3. It means, that resulting occupation numbers of the individual types of atoms in the symetricaly equivalent sites ($4a$, $4b$, $4c$ and $4d$) described by the space group $F\overline{4}3m$ have practically the same values.

Because we have a relatively small number of diffraction peaks in XPD patterns due to the crystallographic symetry of our material, a realization of a measurement on more than two wavelengths should be reasonable to obtain much information and results with less error. Alternatively, we have to choose another experimental method to determine the possible occupation disorder clearly.

3.3 Summary

EDX and XPD has been measured on the powder series of $Mn_2Co_{1-x}Rh_x$. It has been found that this series undergo a tetragonal distortion caused by chemical pressure on the lattice due to the changing content of Rh in our samples. This distortion occurs approximately at $x^{th}_{\mathrm{Rh}} = 0.3$. The unit cell is then elongated in the direction of c-axis with respect to the increasing amount of Rh (see Figure 3.3). Then, another proccess to obtain information about occupation disorder has been done. The fitting of the occupation numbers directly in *Fullprof* has

no reason, because the occupation numbers and scale factor may be strongly correlated. Therefore, the occupation numbers were generated by my own *MatLab* script and only the scale factors and Debye temperature have been set as free parameters in the fit. The results can be seen in Table 3.4 and Figure 3.7. A consideration of the occupation disorder led to smaller value of residuum after fit, but the minimum of the sum of the deviations is not so deep, because I have obtained similar values of the residuum with different combinations of the occupation numbers. According to this, the error in estimation of the occupation numbers is roughly 0.3, because less changes in the resulting occupancy does not make distinct changes in the value of the residuum after fit. Consequently, resulting occupation numbers of the individual types of atoms in the symetricaly equivalent sites described by the space group $F\overline{4}3m$ are practicaly the same.

site	$\overline{occ}_{\mathrm{Mn}}$	$\overline{occ}_{\mathrm{Sn}}$	$\overline{occ}_{\mathrm{Co}}$	$\overline{occ}_{\mathrm{Rh}}$
$4a$	0	1	0	0
$4b$	0.600	0	0.200	0.200
$4c$	0.700	0	0.225	0.075
$4d$	0.725	0	0.275	0.025

Table 3.5: The mean occupation numbers of the symetricaly equivalent atomic sites discribed by the space group $F\overline{4}3m$ for the sample with $x^{th}_{\mathrm{Rh}} = 0.3$. Original values are taken from Table 3.4.

Therefore, we can computed mean values of the occupation numbers in the atomic sites $4a$, $4b$, $4c$ and $4d$. These values are shown in Table 3.5.

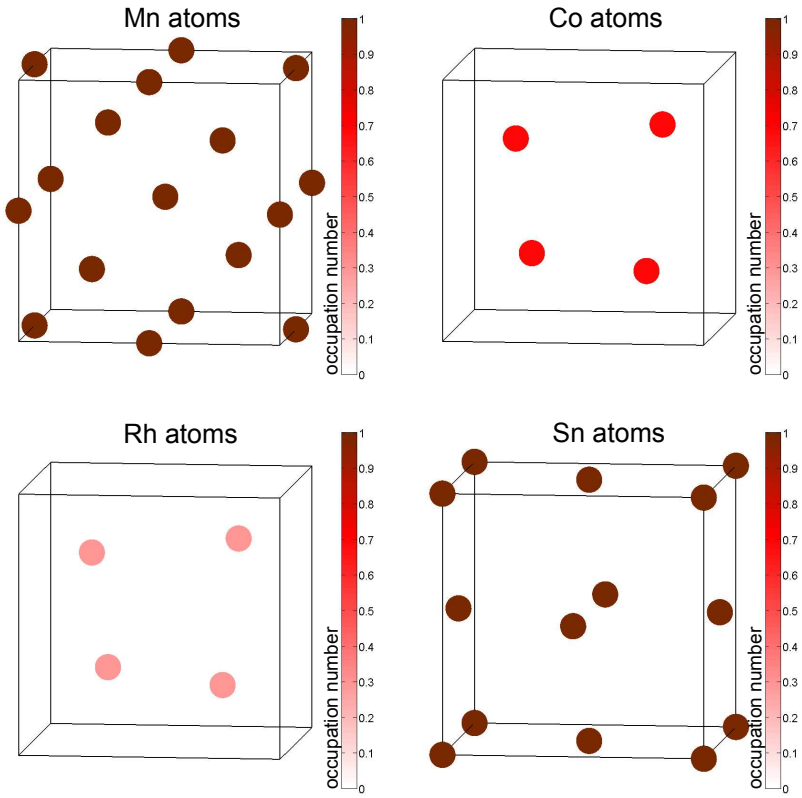

(a) An atomic occupation in the unit cell without a disorder

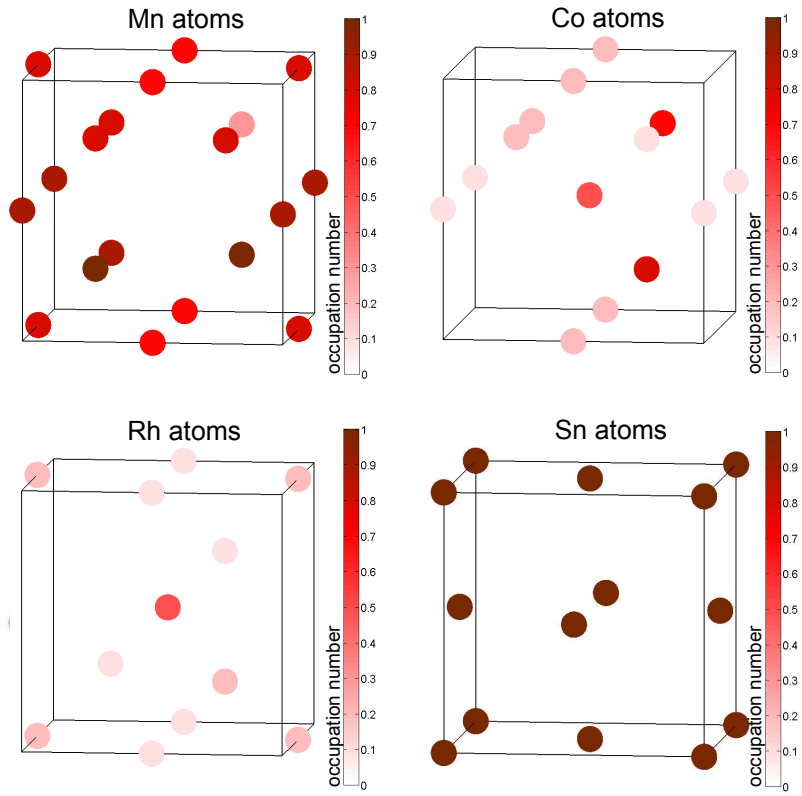

(b) An atomic occupation in the unit cell with an occupation disorder obtained from the simulation (1st SR)

Figure 3.8: The graphical representation of the atomic occupation numbers from Table 3.4. The script for plotting is included in the attachment.

4. EXAFS measurement on powder samples $Mn_2Co_{1-x}Rh_xSn$

EXAFS measurement has been done on the XAS Beamline of the synchrotron ANKA at the Karlsruhe Institute of Technology (KIT), Germany. The principles of this experimental method are described in Section 2.1.5. We have performed the measurement on two absorption edges - CoK edge (7709 eV) and MnK edge (6539 eV). EXAFS was measured on three samples - $x_{\mathrm{Rh}}^{th} = 0.3, 0.4$ and 0.8. During the measurement, the powder was sealed between several layers of a kapton tape sticked to each other. Transmission data and fluorescence data were being collected at the same time, but I have used the fluorescence data for a further analysis, because they have less noise and did not contain any glitches. For the processing of the measured data I have used the software *Demeter* [14] - this software package includes *Athena* (a program for XAS data processing and the exporting of proper EXAFS spectra), *Artemis* (a program for fits of EXAFS spectra), *Hephaestus* (a database of the absorption edges positions), *FEFF* (a script for ab initio calculations from multiple scattering theory) and *Atoms* (generator of the structure input for FEFF calculations).

4.1 Obtaining of EXAFS spectra from the measured data

At first, it is needed to obtain proper EXAFS spectra from the measured data. The program *Athena* is suitable for this process. We have measured the data three times at each abovementioned sample and we have made a mean value of them to reduce a noise in the data. Then, the background has been substracted (the substraction of the smooth function μ_0 from Equation 2.12) and renormalized. The whole process for the sample with $x_{\mathrm{Rh}}^{th} = 0.3$ is depicted in Figure 4.1.

Fourier transform to direct space (see Figure 4.1c) has been made with the resulting data from Figure 4.1b and Hanning function has been chosen as a resolution window. It is recommended to set the higher edge of the resolution window at the point, where the measured data are sufficiently bigger than the noise. This should avoid a creation of new oscilations because of Fourier transformation of the random noise.

4.2 Processing of EXAFS spectra

The EXAFS spectra obtained with the process mentioned above were processed further with the program *Artemis*. The main task was, how to count possible occupation disorder into the FEFF calculations and subsequent fits. Unfortunately, FEFF cannot work with a partial site occupation directly. If we want to count with a disorder or dopants, we have two possible options here (see *Artemis* documentation [35]):

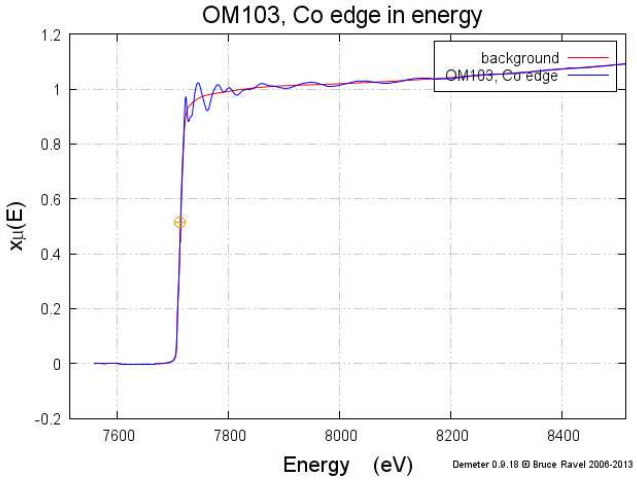

(a) A substraction of a smooth function corresponding to the absorption on isolated atom (red curve) from the measured data (blue curve).

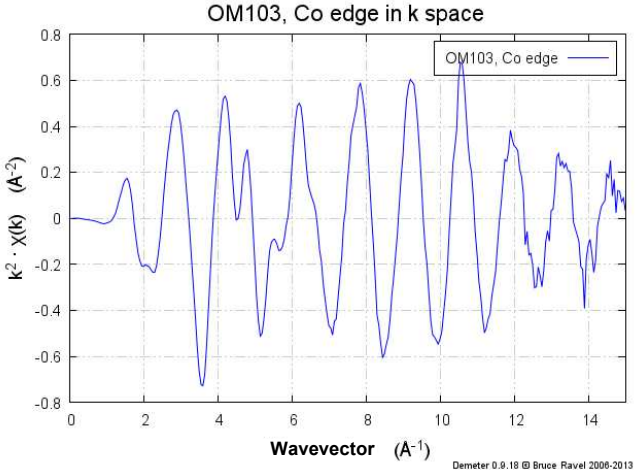

(b) EXAFS data with respect to the wave vector.

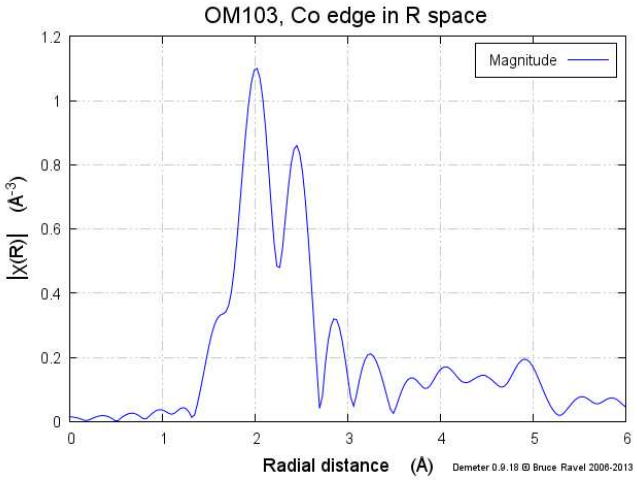

(c) EXAFS data with respect to the radial distance from the core atom (Fourier transformation of the data from figure (b)).

Figure 4.1: Data processing by *Athena*

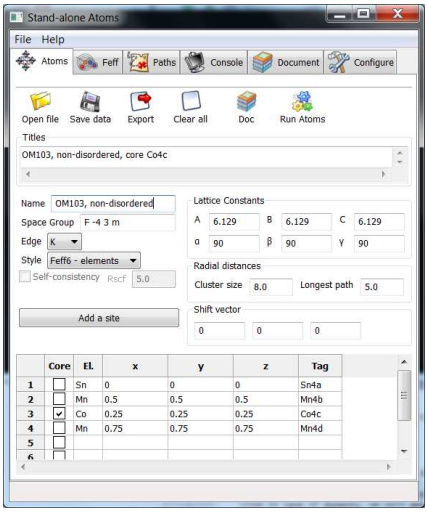

(a) The main window of the program *Atoms*. We would obtain a cluster of atoms corresponding to the non-disordered structure with cobalt as a result of the entry in this figure.

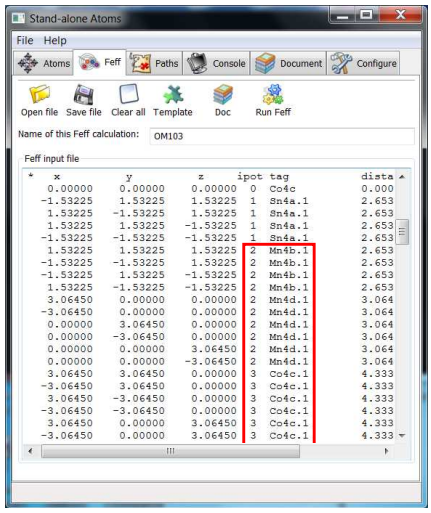

(b) A cluster of atoms, which is generated as an input for FEFF calculations. A list of atoms in the cluster can be changed additionally to count with the possible occupation disorder or dopants. Some atoms, which sould be changed in our case, are highlighted in the red rectangle.

Figure 4.2: A generation of the FEFF inputs.

1. We will generate a cluster of atoms (FEFF input) with the program *Atoms* and then we will change the individual types of atoms in the cluster with respect to required occupation numbers, disorder or doping (see Figure 4.2b)- then, one cluster of atoms (one FEFF input) represents one structure microstate. It is necessary to verify, if the EXAFS spectra resulting from FEFF calculations of individual microstates differ from each other. If yes, then the averaging of the calculated spectra has to be included.

2. In the case of dopants, we will generate two FEFF inputs. The first one - pure structure without dopants. The second one - pure structure only with dopants. Then, we put the computed EXAFS spectra to a fit with different weights, which are interrelated to a dopants quantity.

In the case of our samples, I have combined both ways discussed above. At first, I have made FEFF calculation with the non-disordered structure only with cobalt. The only possible type of occupation disorder in our samples is BiF_3 (see Section 3.2) and it has been taken into account by the manual changing of generated atomic cluster - numbers of atoms correspond to the occupation numbers in Table 1.1. It means, that the resulting FEFF calculation corresponds to the full-disordered state of the structure. The same procedure has been done with the structure, which consists only rhodium atoms instead of cobalt. *Matlab* script for a FEFF input modification is included in the attachment.

So finally, we have four types of calculations - calculations obtained from the non-disordered structure with cobalt and from the structure with rhodium

as well, and the calculations obtained from the fully-disordered structure with cobalt and from the structure with rhodium. Rhodium amount will be taken into account as it is mentioned above (the option n.2). If we put the calculation belonging to the non-disordered and fully-disordered structure with different weights to the fit, we can implement some information about the degree of disorder.

If we would consider the degree of disorder as δ, the corresponding occupation numbers can be evaluated as in the following equations.

$$\begin{aligned} o_{\mathrm{Co}}^{4b} &= (1-x)\frac{\delta}{3} & o_{\mathrm{Rh}}^{4b} &= x\frac{\delta}{3} & o_{\mathrm{Mn}}^{4b} &= 1-\frac{\delta}{3} \\ o_{\mathrm{Co}}^{4c} &= (1-x)(1-\frac{2}{3}\delta) & o_{\mathrm{Rh}}^{4c} &= x(1-\frac{2}{3}\delta) & o_{\mathrm{Mn}}^{4c} &= \frac{2}{3}\delta \\ o_{\mathrm{Co}}^{4d} &= (1-x)\frac{\delta}{3} & o_{\mathrm{Rh}}^{4d} &= x\frac{\delta}{3} & o_{\mathrm{Mn}}^{4d} &= 1-\frac{\delta}{3} \end{aligned} \tag{4.1}$$

Here, x is the value of doping. Both x and δ can have the values in the interval $[0, 1]$. The limit case, where $\delta = 0$, corresponds to the non-disorder state of structure and if $\delta = 1$, we have the fully-disorder state.

The result of the FEFF calulations is the list of scattering paths, which would have a significant contribution to EXAFS spectra. These paths are then included into fit in *Artemis*. Because our data have been measured on CoK and MnK absorption edges and we count with BiF_3-type of disorder, cobalt and manganeese atoms can sit in different crystallographic positions. Therefore, we have to make FEFF calculations with all possible positions of core atoms.

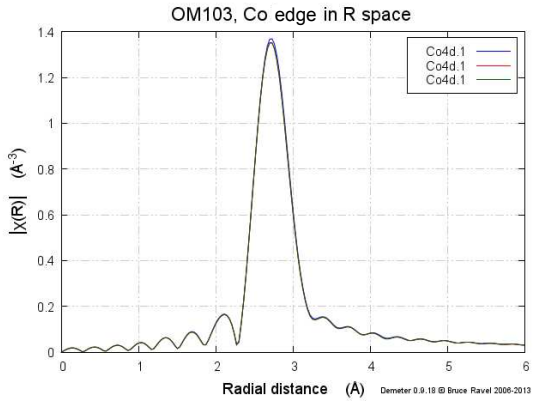

(a) A plot of the single scattering path on the cobalt atoms in position 4d (core = cobalt in 4c) corresponding to three structure microstates.

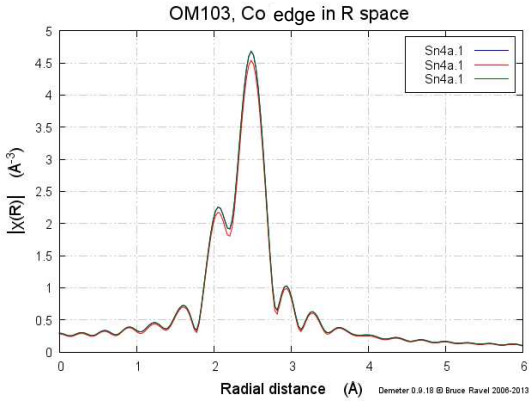

(b) A plot of the single scattering path on the tin atoms in position 4a (core = cobalt in 4c) corresponding to three structure microstates.

Figure 4.3: Plots of the scattering paths contributions corresponding to three structure microstates.

There is a plot of contributions of two scattering paths obtained from the FEFF calculation on the fully-disordered cluster of atoms with three different structure microstates ($x = 0.3$ and a core cobalt atom in the site 4c) in Figure 4.3. One can see that there is no big difference between the spectra, which were obtained by different microstates. Therefore, the spectra have not to be averaged and we are

x^{th}_{Rh}	δ
0.3	0.68 ± 0.13
0.4	0.04 ± 0.07
0.8	0.35 ± 0.14

Table 4.1: Degrees of disorder following from EXAFS measurement.

able to put only a calculation corresponding to one of the structure microstates to a subsequent fit.

Only the contributions from the first and second coordination shells were fitted, because the contributions of other coordination shells are relatively small. Advantage is, that only single-scattering paths are neccessary to count into the fit, because multi-scattering ones have bigger length and small contribution to the resulting spectra.

As it was mentioned in Section 2.1.5, we fit the parameters R_Γ, σ_Γ, S_0 and E_0. Mean square displacement σ_Γ represents an error in an estimation of the scattering path length, so it should depend on types of atoms at the scattering path ends. Moreover, σ_Γ should correspond to thermal fluctuations, so it should be inversely proportional to the atomic mass (of the atoms in the scattering path) as in the case with the Deby-Waller factors. We need as small number of the free parameters as it is possible to avoid some correlation and non-physical values in results. Therefore, I have bound σ_Γ which correspond to light (Co, Mn) and to heavy atoms (Rh, Sn) together and they differs only in a view of the order of the coordination shell, where the second atoms sits. As a result, we have only four σ_Γ which correspond to the paths like $(\mathrm{Co/Mn\text{-}Co/Mn})_{1,2}$, $(\mathrm{Co/Mn\text{-}Rh/Sn})_{1,2}$. Another reason to have least number of σ_Γ parameters as we can is that σ_Γ can correlate with S_0 or δ. The energy shifts E_0 and the amplitudes S_0 were considered as own values for each data set (Co and Mn edge).

The amplitudes S_0^{CoK} and S_0^{MnK} were set rigidly to 1 as it is mostly recommended [35]. Other resulting parameters after fit for the sample with $x^{th}_{\mathrm{Rh}=0.3}$ are following:

$$\begin{aligned}
\sigma_{\mathrm{Co/Mn\text{-}Co/Mn(1)}} &= \quad 0.018 \pm 0.002 \ \text{Å}^2 \\
\sigma_{\mathrm{Co/Mn\text{-}Co/Mn(2)}} &= \quad 0.016 \pm 0.003 \ \text{Å}^2 \\
\sigma_{\mathrm{Co/Mn\text{-}Rh/Sn(1)}} &= \quad 0.004 \pm 0.001 \ \text{Å}^2 \\
\sigma_{\mathrm{Co/Mn\text{-}Rh/Sn(2)}} &= \quad 0.022 \pm 0.008 \ \text{Å}^2 \\
E_0^{\mathrm{CoK}} &= \quad -1.8 \pm 0.6 \ \text{eV} \\
E_0^{\mathrm{MnK}} &= \quad -2.6 \pm 0.8 \ \text{eV}
\end{aligned}$$

A result of the fit for the sample with $x^{th}_{\mathrm{Rh}} = 0.3$ is depicted in Figure 4.4. The values showed above were used as guess parameters for the fitting of the spectra obtained on the other samples. The resulting values of degrees of disorder are shown in Table 4.1.

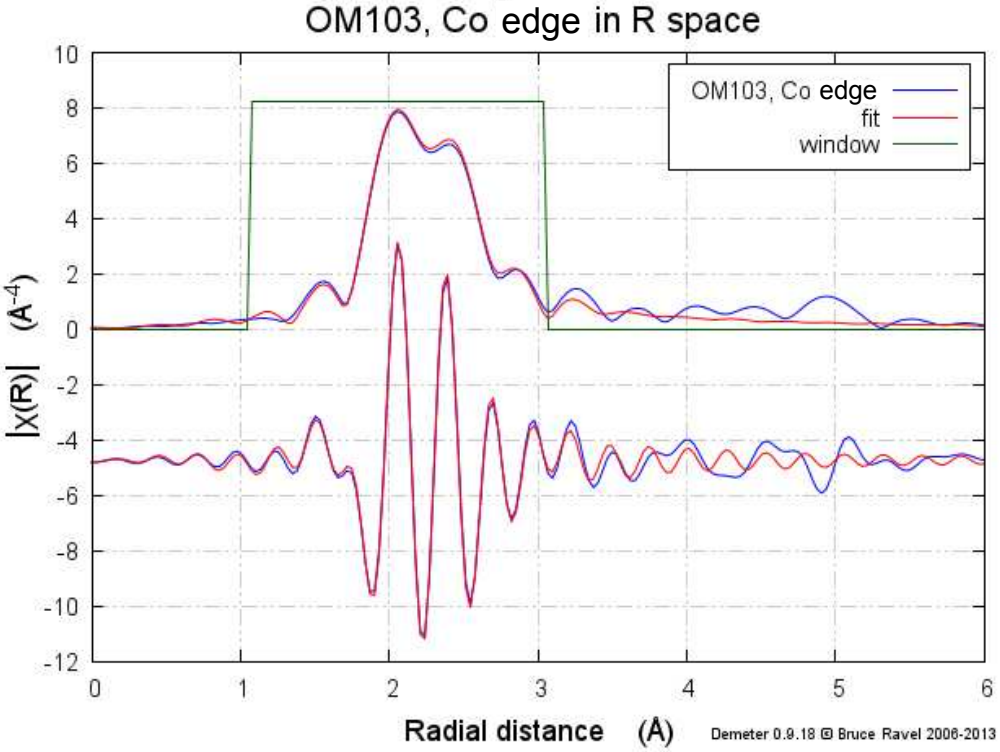

(a) The fit of the EXAFS spectra on CoK absorption edge measured on the sample with $x_{\mathrm{Rh}}^{th} = 0.3$.

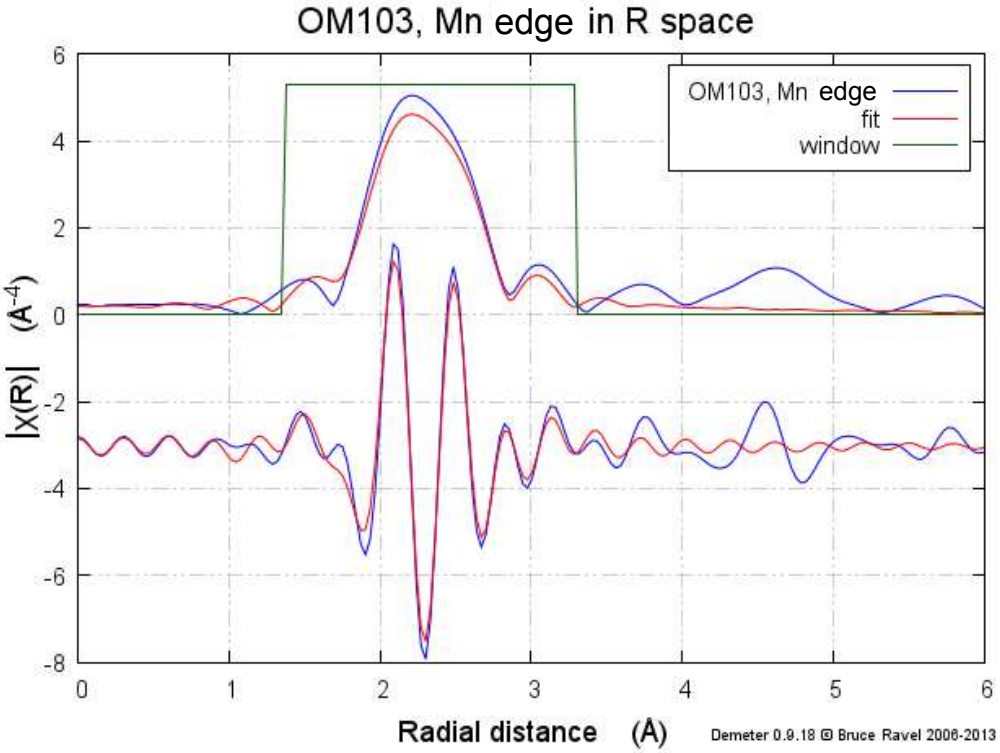

(b) The fit of the EXAFS spectra on MnK absorption edge measured on the sample with $x_{\mathrm{Rh}}^{th} = 0.3$.

Figure 4.4: The fits of the EXAFS spectra for the sample with $x_{\mathrm{Rh}}^{th} = 0.3$.

4.3 Summary

EXAFS been measured on the powder series of $Mn_2Co_{1-x}Rh_x$ to obtain information about possible occupation disorder in our samples. This structure feature was taken into account by Equations 4.1 and by importing several different FEFF calculations into the fit with different weights.

Big difficulty of the processing is to distiguish between contributions of the individual shells in measured spectra. As one can see from Figure 4.4, contributions of our first and second coordination shell overlap mutually each other. This is may lead to a fact that the error of estimated δ are possibly undervalued. Therefore, better results and easier data processing would be obtained on Heusler alloys, which have a bigger unit cell and corresponding lattice parameters - the contributions of individual coordination shells can be easier to separate. However, the disorder must be present in our samples, because I was not able to fit EXAFS data without a consideration of disorder. The values obtained from that fits were not physicaly reasonable (mean square displacements were less than 0, displacements corresponding to heavier atoms were smaller than displacements corresponding to light ones).

It is hard to say from three values, if there is some trend. But it seems that degree of disorder does not increase or decrease with respect to a growing amount of rhodium in our samples. For the more complex information it is neccessary to perform a measurement on the whole series of our samples. If the disorder originates in a preparation, it would be interesting to measure again with annealed samples, if the result will be the same.

	XPD				EXAFS			
site	$\overline{occ}_{Mn}$	$\overline{occ}_{Sn}$	$\overline{occ}_{Co}$	$\overline{occ}_{Rh}$	$\overline{occ}_{Mn}$	$\overline{occ}_{Sn}$	$\overline{occ}_{Co}$	$\overline{occ}_{Rh}$
4*a*	0	1	0	0	0	1	0	0
4*b*	0.600	0	0.200	0.200	0.77 ± 0.15	0	0.16 ± 0.03	0.07 ± 0.01
4*c*	0.700	0	0.225	0.075	0.45 ± 0.09	0	0.38 ± 0.07	0.16 ± 0.03
4*d*	0.725	0	0.275	0.025	0.77 ± 0.15	0	0.16 ± 0.03	0.07 ± 0.01

Table 4.2: A comparison of the occupation numbers obtained from XPD and EXAFS measurement for the sample with $x^{th}_{Rh} = 0.3$. The occupancies obtained from EXAFS were computed with Equations 4.1.

There is a comparison of the occupation numbers obtained from XPD measurement in Chapter 3 and the occupation numbers obtained from Equations 4.1 with the resulting values of δ. It seems that the values obtained from XPD correspond rather to the state of full occupation disorder, because the occupancies are closely to the values $occ_{Mn} = \frac{2}{3}$ and $occ_{Co} + occ_{Rh} = \frac{1}{3}$ (according to Table 1.1). Anyway, it is clearly seen that the occupation disorder with the big degree is present in the sample with $x^{th}_{Rh} = 0.3$.

5. Single-crystal diffraction on Ni_2MnGa

Ni_2MnGa is a member of a relatively small family of the shape memory alloys [36]. Strains in these materials can be controlled by an application of an external magnetic field or by an application of well defined pressure.

A previous structure research of Ni-Mn-Ga compounds has been performed mostly on powder samples (see for example [16, 37, 38]). Beside this, we have performed a systematic study by single-crystal diffraction. Ni-Mn-Ga alloys with a composition close to the stoichiometric Ni_2MnGa undergo a thermoelastic martensitic transformation [37] to the less symetric martensitic structure phase. The composition of our sample has been estimate as $Ni_{50.1}Mn_{28.4}Ga_{21.5}$ (obtained by EDX), so we should expected some lattice distortion at the room temperature. In this chapter, I will show results of our structural studies on this material - some of these results have been used to publish the article [39], which has been made with a collaboration of the magneto-optical group in our faculty.

5.1 Lattice parameters and domain structure

As it was said in the introduction of this chapter, the structure of Ni_2MnGa can be controlled by pressure. We must take care of this fact within a manipulation of the sample and when we place it on a holder. Our sample has a shape of block

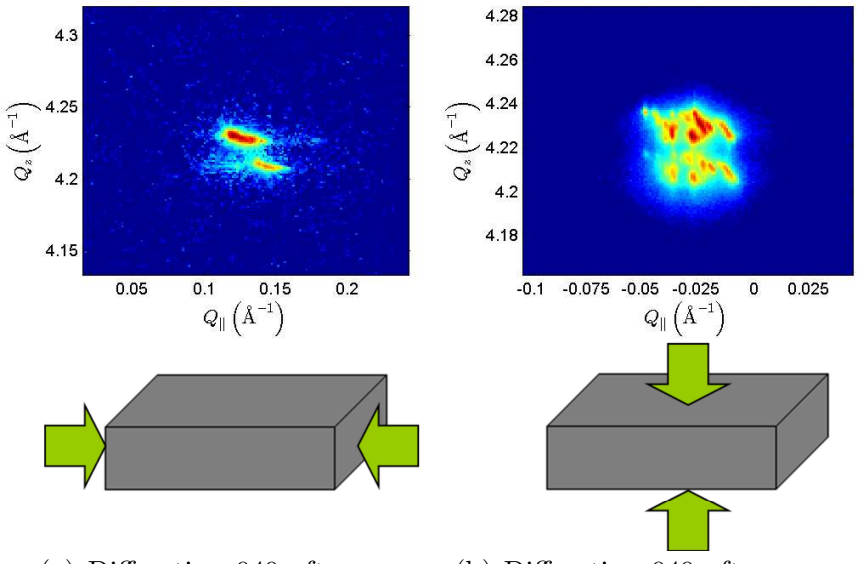

(a) Diffraction 040 after pressure application in the direction along the longest edge of the sample.

(b) Diffraction 040 after pressure application perpendicular to the largest side of the sample.

Figure 5.1: Reciprocal space map of diffraction 040 after pressure application in the specified directions.

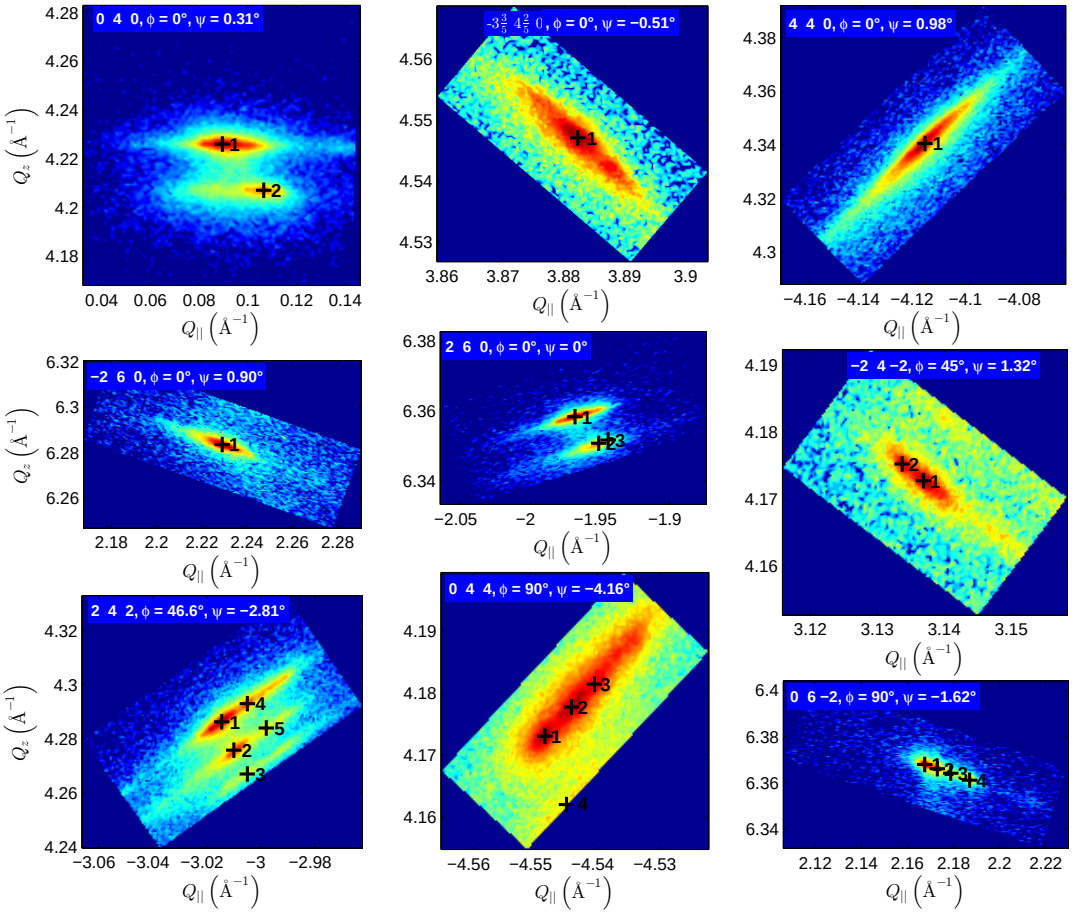

Figure 5.2: The reciprocal maps of nine diffractions. Maps contain more than one maxima (marked with black crosses in figure), which could correspond with a domain structure or mosaic.

with edges approximately $5 \times 1 \times 0.5$ mm. We can induce some domain structure in the sample by an application of pressure in the specified directions. One domain corresponds to one diffraction peak in a measured reciprocal space map. As one can see from the reciprocal space map of the diffraction 040 in Figure 5.1a, we induced simple two domains structure with the pressure applied along the longest edge of the sample. Opposite to that, when we apply the pressure perpendiculary to the largest side of the sample, the sample contains more domains then, which correspond to a lot of diffraction peaks in Figure 5.1b. For a further examination, I have worked with the case (a) (two domains), because the second one is practicaly impossible to process and evaluate.

I have measured x-ray diffraction on a single-crystalline sample Ni_2MnGa using the method of reciprocal space mapping; I used CuKα line and the following configuration of optics: $\frac{1}{4}$ divergence slit, Soller slit 0.02 and the Bartels monochromator on the primary beam and the analyzer crystal (12“ acceptance) on the secondary beam. This configuration is suitable for the exact location of the scattering vector in the scattering plane.

Nine reciprocal space maps were measured; all are depicted in Figure 5.2. I used *MatLab* for the processing of the data. In the first step, I indexed the individual measured maps. I have used the lattice parameters from [40] and compared

the norms, the distances and the angles between the measured and computed scattering vectors. The spots with the highest intensity were taken as a reference. The structure published in [40] is the monoclinic lattice with the lattice parameters:

$$a = 5.945 \text{ Å}, \quad b = 5.937 \text{ Å}, \quad c = 5.615 \text{ Å}$$
$$\alpha = 90°, \quad \beta = 90°, \quad \gamma = 90.325°$$

The only problem was to obtain the indices of the second map (in Figure 5.2 that one with the resulting indices $\overline{3}\frac{3}{5}4\frac{2}{5}0$). In this map, the measured and computed positions of the diffraction spots exhibit large deviations. We know from [40] that Ni_2MnGa can show five-layered modulated structure. This leads to extra diffraction spots with noninteger indices. In our case, indices $\overline{3}\frac{3}{5}4\frac{2}{5}0$ fit best to the second map.

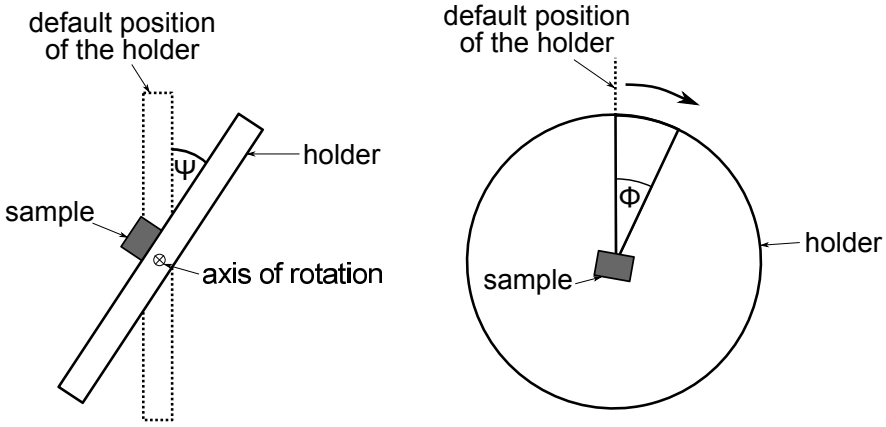

(a) View along the primary beam (b) View perpendicular to the sample holder

Figure 5.3: A sketch of the angles of possible rotation with the sample holder.

The angles Φ and Ψ in the measured reciprocal maps are angles of a rotation of the sample. The sketch of the sample holder of these angles is in Figure 5.3.

The next task was to obtain the exact values of the lattice parameters. We used the fact that we can determine the lengths of the scattering vectors (i.e., the interplanar distances) exactly, since these results are not affected by much less precise values of Φ and Ψ. Thus, I solved numerically the nonlinear system of equations:

$$\left|\vec{Q}^i_{exp}\right| = \frac{2\pi}{d^i_{hkl}}, \tag{5.1}$$

where d^i_{hkl} is the computed interplanar distance of the i-th diffraction maximum (for monoclinic structure), and $\left|\vec{Q}^i_{exp}\right|$ is the measured length of its scattering vector. Because we have nine maps, i goes from 1 to 9.

Because of more than one diffraction maximum in our maps, we solved Equation 5.1 for all combination of spots in our maps and as a result we have chosen the combination of the diffraction maxima, which led to the smallest residuum. We have obtained the following lattice parameters:

$$a = (5.971 \pm 0.002)\ \text{Å}$$
$$b = (5.9467 \pm 0.0007)\ \text{Å}$$
$$c = (5.586 \pm 0.002)\ \text{Å}$$
$$\gamma = (90.31 \pm 0.01)^\circ$$
$$\alpha = \beta = 90^\circ$$

The result was obtained with a combination of the diffraction spots in maps, which is shown in Table 5.1.

Then, I tried to find an orientation of the reference domain with respect to the sample holder. With *reference domain* we mean the domain:

- which corresponds to the reference indices of our measured reciprocal maps
- which has the lattice parameters obtained from previous step
- whose diffractions correspond to the spots from Table 5.1

The orientation of the reference domain can be described using a set of three Euler angles A, B and Γ, which we can fit. Because of the large width of the measured peaks in Φ and Ψ scans, the angles Φ and Ψ are not quite precisely measured. We have fitted these values too, but we allowed the deviations up to $\pm 3^\circ$ from their original values.

In Figure 5.4, one can see the computed positions of diffractions of the reference domain (marked by green crosses).

The next question was to explain other peaks in our maps. We can apply the same process on them. There are two possibilities for explaining these peaks:

- **mosaic blocks** – Mosaic blocks have similar orientation as the reference domain (Euler angles from the reference and from the mosaic block differ only in the range of several degrees). In our reciprocal maps, these blocks correspond to diffraction spots, which has the same diffraction indices as our reference domain. That leads to the same lengths of the scattering vector, 2Θ value respectively. But because of the different orientation of the mosaic blocks, ω value of the corresponding diffraction spots will be different. The shapes of the trajectories of the ω-scans (while the 2Θ is constant) in our reciprocal maps are indicated in Figure 5.5.
- **domain structure** – The different domains can have very different orientation with respect to the reference domain. That leads to a fact that their

Reference *hkl* of the map	040	$3\overline{\frac{3}{5}}4\frac{2}{5}0$	440	$\overline{2}60$	260	$\overline{2}4\overline{2}$	242	044	$06\overline{2}$
Spot number (see Figure 5.2)	1	1	1	1	1	1	4	2	2

Table 5.1: Combination of diffraction spots which led to the smallest residuum after a refinement of the lattice parameters.

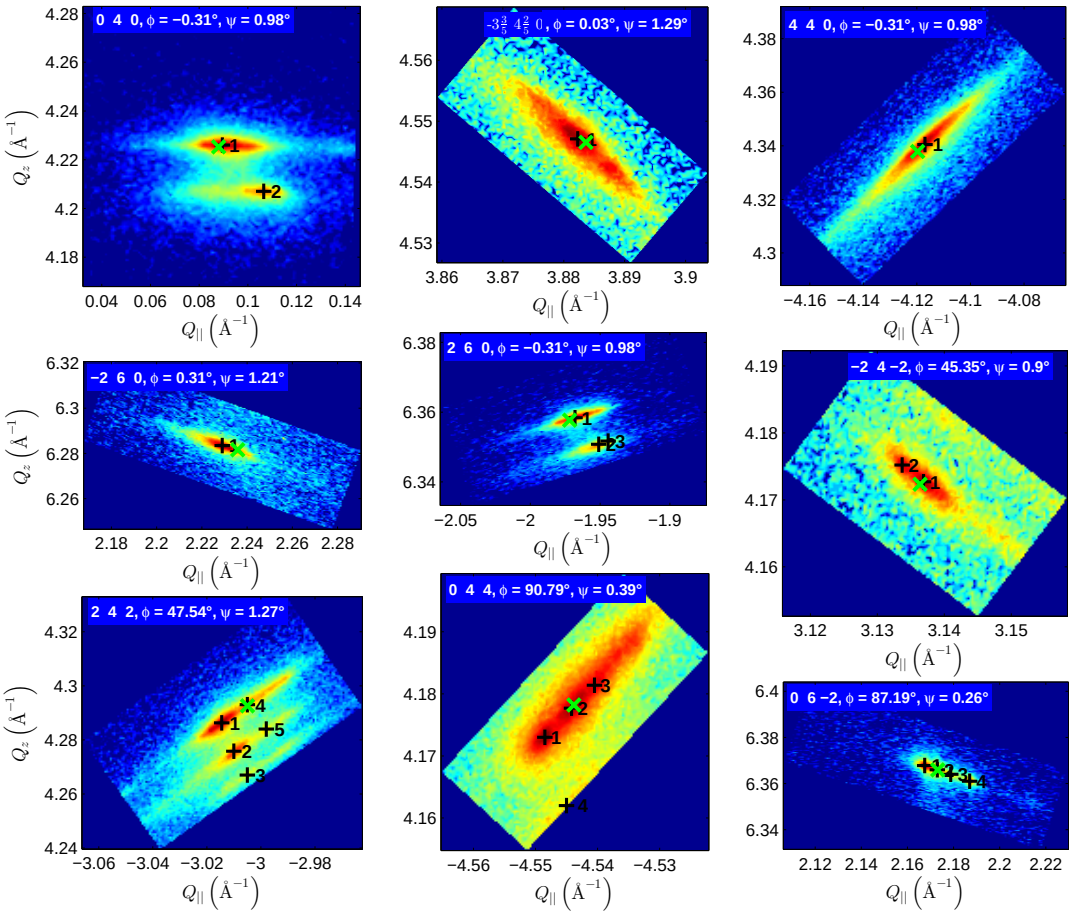

Figure 5.4: A comparison of the computed (green crosses) and measured positions (black crosses) of the diffraction maxima.

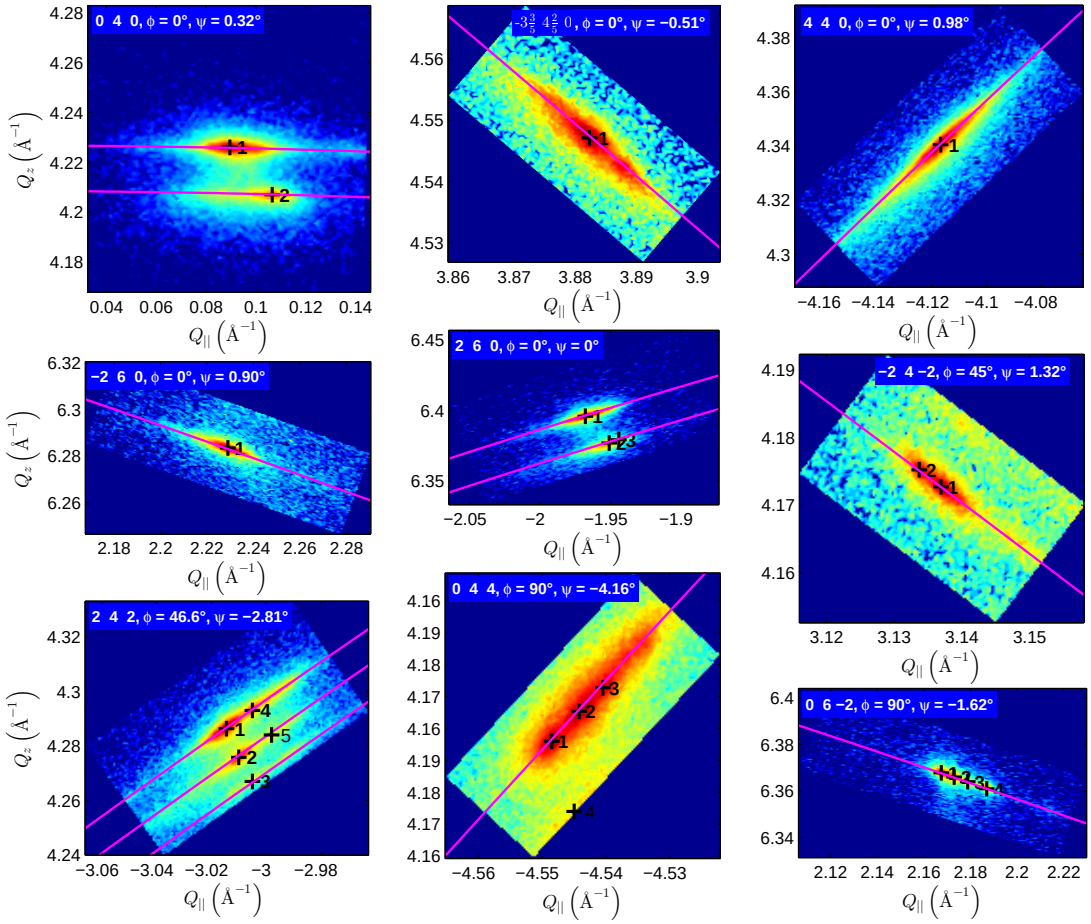

Figure 5.5: Reciprocal maps. The shapes of the trajectories of the ω-scans with constant 2Θ values in reciprocal space are drawn by purple color. Diffraction spots, which lie on these curves, correspond to mosaic blocks.

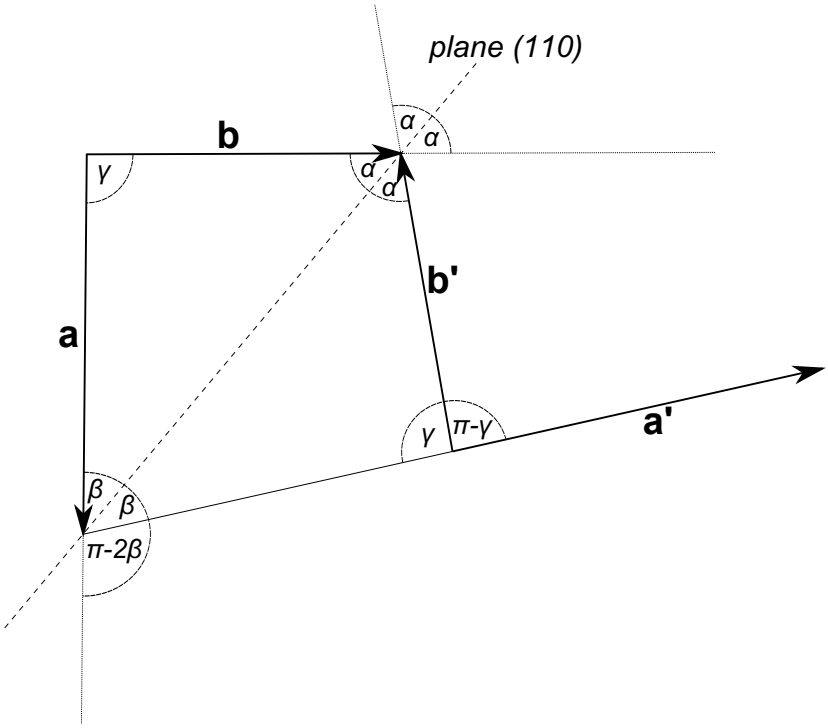

Figure 5.6: The new domain, which appeared due to the twinning, has different angles in its unit cell.

diffraction peaks should not have the same indices as reference. We know from [40] that Ni_2MnGa can undergo the twinning over the plane (110). It means that:

1. This kind of domain will be rotated around c-axis about 90° with respect to reference. In our maps, it corresponds to the change of diffraction indices from hkl to $\overline{k}hl$.
2. Because of different orientations and different diffraction indices, the length of the scattering vector will be different with respect to the reference (different 2Θ coordinations of the peaks in our maps). Moreover, this twinning leads to the change of angles in the unit cell. This fact is shown in Figure 5.6.

In order to find the orientation of the different domains, we can use the same procedure as for the reference domain. We have tried the following options in the fit:

- The second domain has the same lattice parameters as the reference. This domain and the reference domain are mutually rotated around c-axis about 90°.
- The second domain is the twin (see above).

In the case of the twinning, we obtain much smaller ressiduum from the fit. The result of this refinement is in Figure 5.7. Since the peaks with different 2Θ values did not appear in some maps, we have fitted only the peaks in maps with the reference indices 040, 260, 242, and 044.

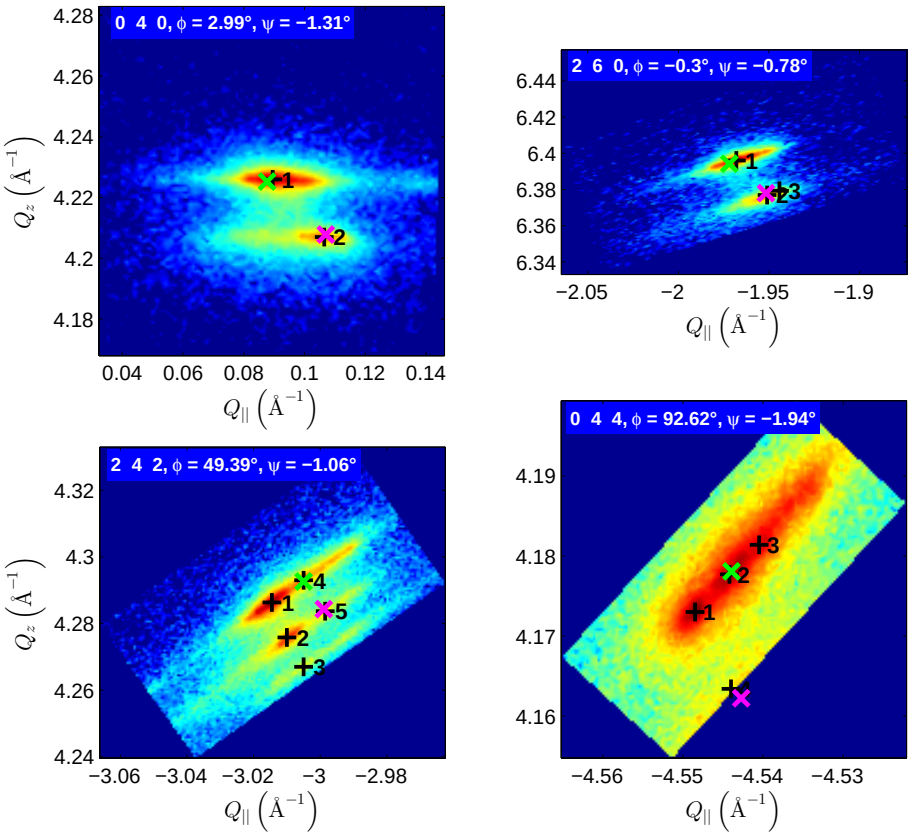

Figure 5.7: The fitted position of the twinning domain (purple crosses). Green crosses correspond to the diffraction spots belonging to the reference domain (previous results) and black crosses correspond to the measured positions of diffractions.

5.2 Modulation of the structure

The following task was to study the modulated structure. Ni_2MnGa can form a modulated structure which leads to extra diffraction spots along directions [±110] in reciprocal space (see [40]).

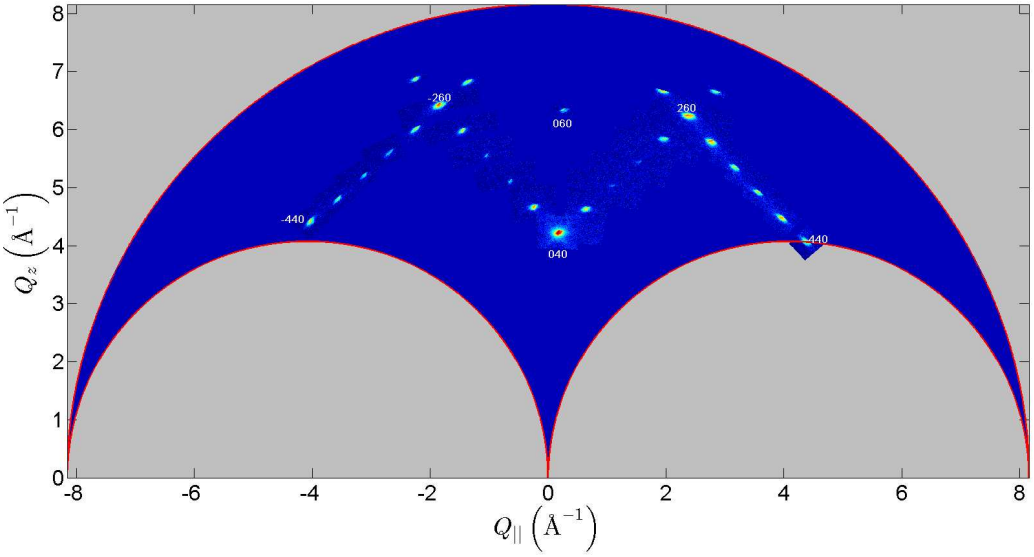

Figure 5.8: A result of the measurement of the extra diffraction spots cause by structure modulation.

At first, I measured additional diffraction maxima caused by the modulation. I used CuKα line and the following configuration of the optics: $\frac{1}{4}$ divergence slit, soller slit 0.02 and the Bartels monochromator on the primary beam as well as the rocking curve detector on the secondary beam. This configuration is not optimal as for the accuracy of the 2Θ angle, but we need a lot of intensity, because we want to see rather weak diffraction spots. The result of the measurement is in Figure 5.8.

It can be seen, that there are four extra diffraction spots between the ordinary diffraction maxima (for example 040 and 260). This leads to a fact, that Ni_2MnGa creates a 5-layered modulation structure along the direction [110] and the atoms in the planes (110) are periodicly shifted in the directions $\pm[\bar{1}10]$.

This periodic shift can be described using the sum of harmonic functions:

$$\Delta_k = \sum_{n=1}^{3} A_n \sin \frac{2\pi n \delta_k}{L} \tag{5.2}$$

where Δ_k is the shift of the k-th atom, L is the period of modulation (5 in our case), A_n are the amplitudes and δ_k is coordinate in the direction [110] of the k-th atom.

We can describe the basic structure of Ni_2MnGa parent phase with the space group $Fm\bar{3}m$ (Figure 5.9a). In Figure 5.9b) the description of modulation is sketched. Then, I have determined the values of the amplitudes A_n from our measurement. At first, I have measured some of the diffractions with the following configuration of optics: $\frac{1}{2}$ divergence slit, and the hybrid monochromator on

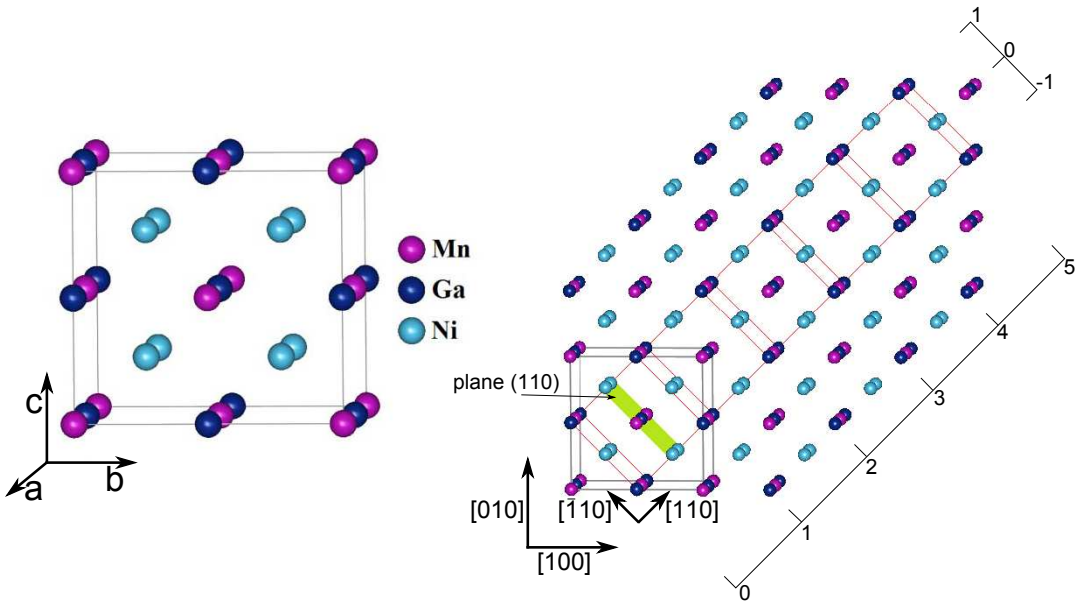

(a) Ni_2MnGa unit cell

(b) A description of the modulation – atoms in planes paralel to (110) (green color on the figure) are shifted in directions $\pm[\bar{1}10]$ (shift Δ_k). The fractional coordinates δ_k go from 0 to 5.

Figure 5.9: A sketch of the modulated structure.

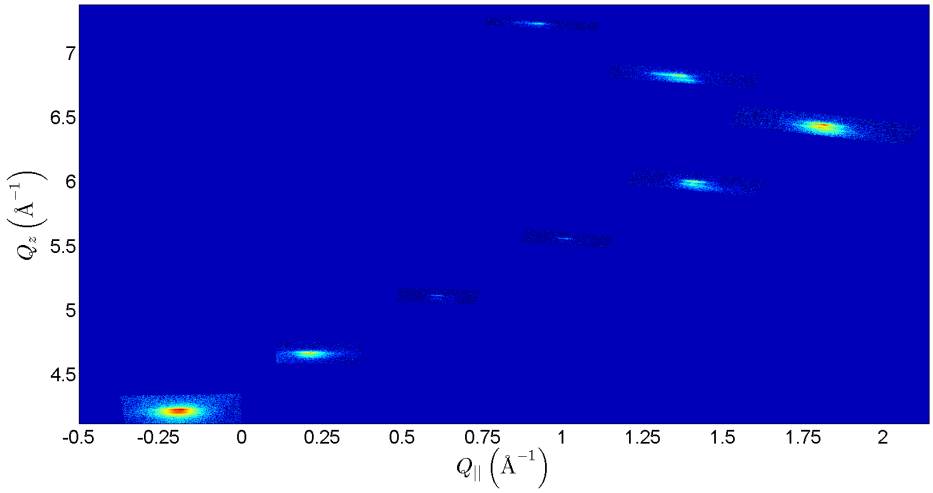

Figure 5.10: The measurement of some diffraction spots with the analyzer crystal before the detector.

the primary beam and the analyzer crystal on the secondary beam. The result of this measurement is in Figure 5.10.

I have obtained values of A_n by the fitting of integrated intensities of the measured peaks to their theoretical formula 2.4 - the structure factor has been computed from the structure block, which contained 5 unit cells distorted by the modulation. The *X0h search* tool in [41] has been used to obtain components of the Ni_2MnGa refraction index. We have fitted the logarithm of the integrated intensities, because we wanted to take into account that some of the intensities are small. In addition to the therms in Equation 2.4, a constant background has been included into our fit - the fitting script written in *MatLab* is included in the attachment. The results of the fit are plotted in Figure 5.11.

In Table 5.2, I compare our values of A_n with the values published previously

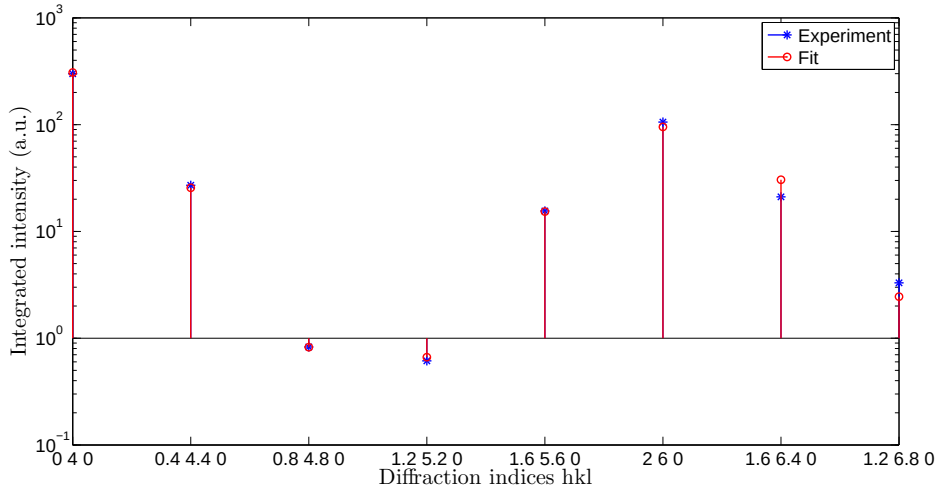

Figure 5.11: The fit of the logarithm of the integrated intensities.

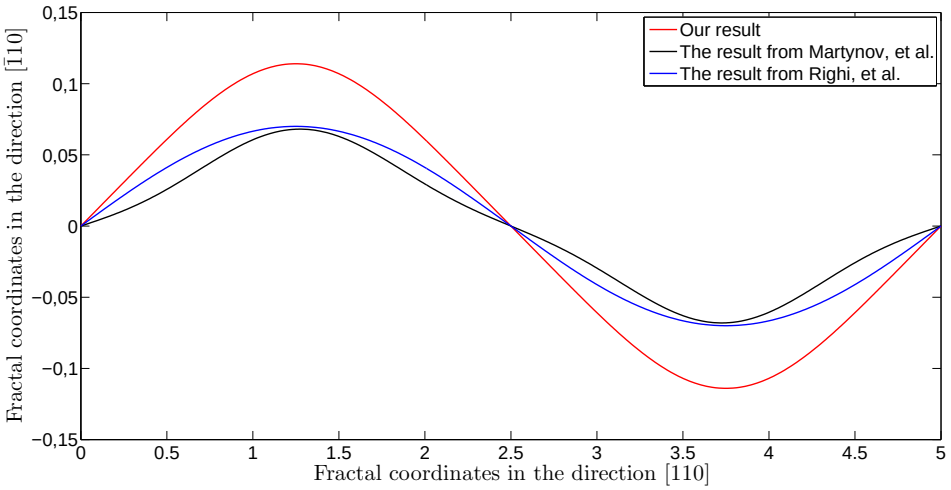

Figure 5.12: A comparison of the modulation waves obtained from our experiment and from articles of Martynov, et al. [17] and Righi, et al. [38]. The modulation wave obtained in [17] is inverted over the x-axis to compare the results better (the opposite notation should give the same results).

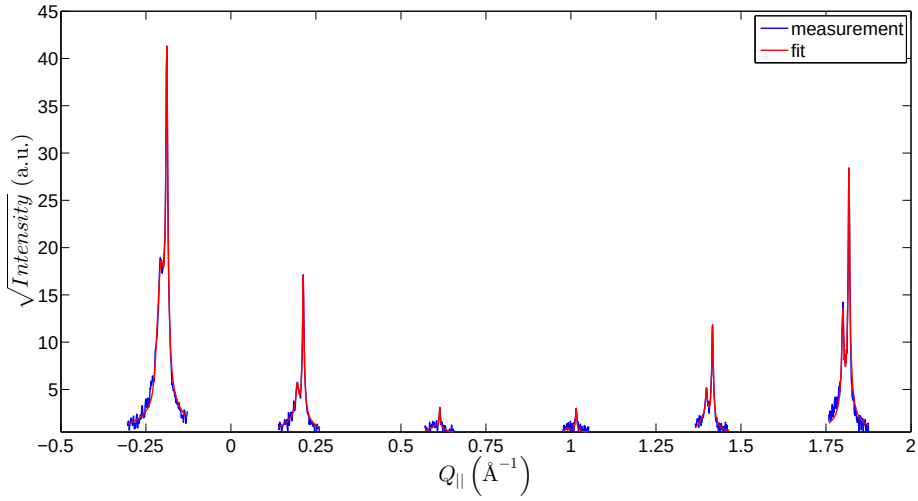

Figure 5.13: A cut trough the satelite diffraction allong the direction [110] in reciprocal space (taken from maps in Figure 5.10). The fit of the peaks with the pseudo-Voigt functions is here depicted as well.

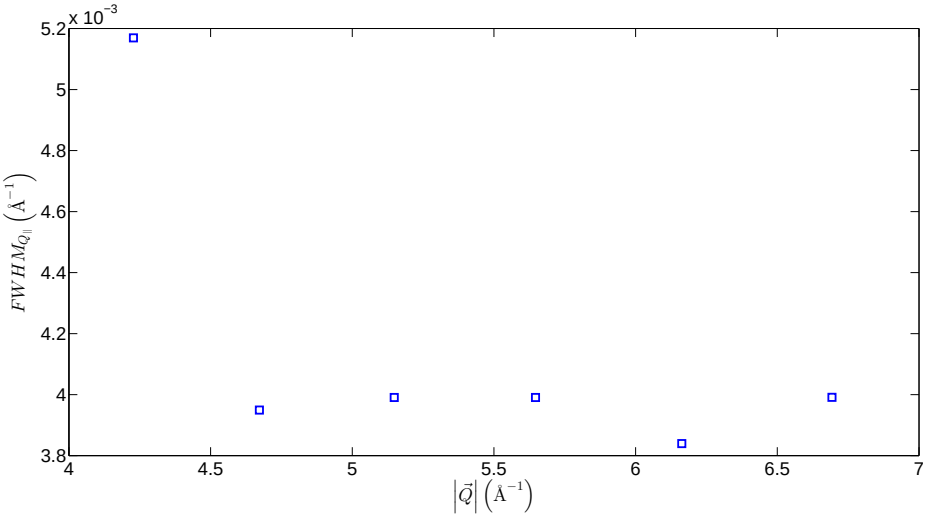

Figure 5.14: A dependence of the width of the peaks (obtained from the cut in Figure 5.13) on absolute value of scattering vector.

The amplitude	Our result	The result from [17]	The result from [38]
A_1	0.100 ± 0.008	-0.06	0.0700 ± 0.0007
A_2	0.003 ± 0.007	0.002	-
A_3	-0.007 ± 0.011	0.008	-

Table 5.2: The values of the amplitudes A_n in the comparison to the results in the articles [17] and [38].

in [17, 38]. The modulation waves 5.2 with the parameters from Table 5.2 are depicted in Figure 5.12.

There is the cut trough the satelite maxima in Figure 5.13. The shapes of the peaks have been fitted with the pseudo-Voigt functions - corresponding values of the full widths at highest maxima are shown in the plot in Figure 5.14 (FWHM of the stronger peaks from the pairs of satelite diffractions in Figure 5.13 were taken). According to Equation 2.7, FWHM should be independent on the diffraction vectore. If we consider a possible inaccuracy in the fitting due to presence of the spots corresponding to different mosaic blocks, the independence is fulfilled with an exception of the diffraction 040. This diffraction has the largest intensity from the measured ones, so the diffraction spots corresponding to the mosaic blocks have a big influence on an overall shape of 040 diffraction spot and it could cause the deviation in FWHM estimation.

If some distorted structure blocks would be present, where the lattice parameters might be slightly changed for instance due to a different stoichiometry, FWHM should be proportional to $\left|\vec{Q}\right|$ (see for example [42]).

5.3 Diffraction at higher temperatures

According to previous research and results for example in [16], the cubic structure phase (so-called austenite) of Ni_2MnGa should exists at higher temperatures. Richard et al. [16] determine the transition temperature near 50°C from temperature dependent XPD measuremets. In our case, we should expect the transition temperature slightly different, because of a different stoichiometry of our sample.

Beside the XPD measurement, we are able to manage a single-crystal diffraction measurement in dependence on temperature in our laboratory as well. The measurement procedure was following: we performed reciprocal space mapping of the diffraction 040 (see the previous section 5.1) at many values of temperature with the step of 3°C. The ajusted temperature oscilated in the range of 1-2°C, so any smaller step in the temperature measurement would be useless. When the transition occurs, we should be able to see, how the original 040 peak disappears and the new one 400 corresponding to the austenitic phase should be visible. The cubic austenitic phase is more symetric and its lattice parameter a is smaller than a and b in the martensitic room temperature phase, we should expect the position of new 400 diffraction at higher 2Θ values.

Heating has been done with the heater inbuilt in a sample holder, which was covered with a graphite dome for evacuation of an atmosphere near the sample for a better temperature stability. Our sample was hold with thin iron wires - this polycrystalline iron diffracts too, but its diffractions should be in different posi-

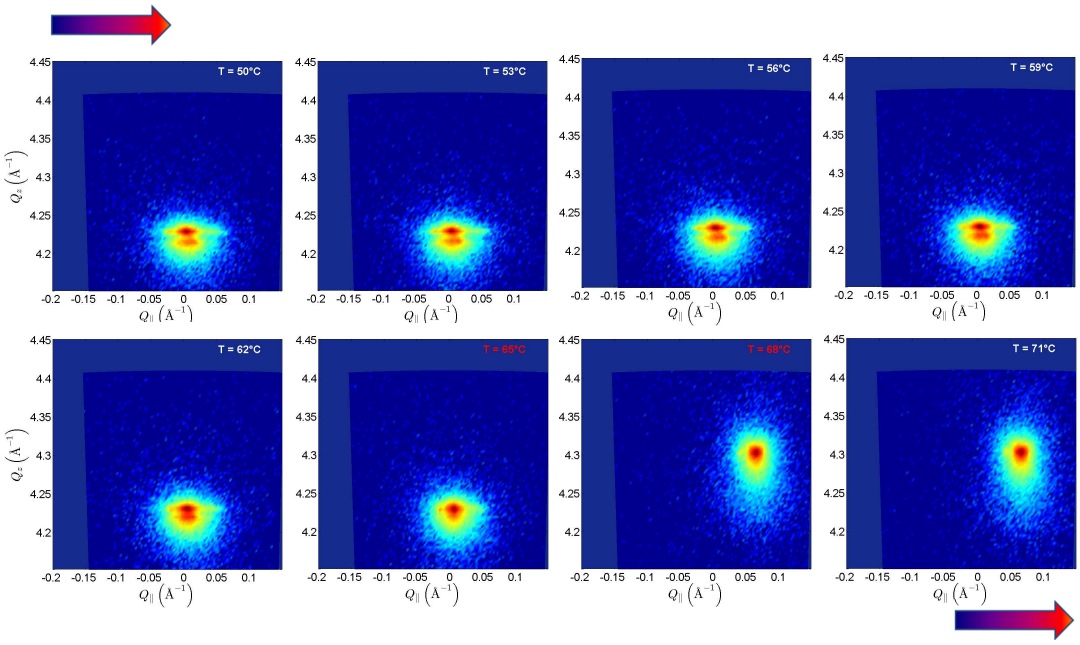

(a) A temperature dependence of the 040 reciprocal space map during heating.

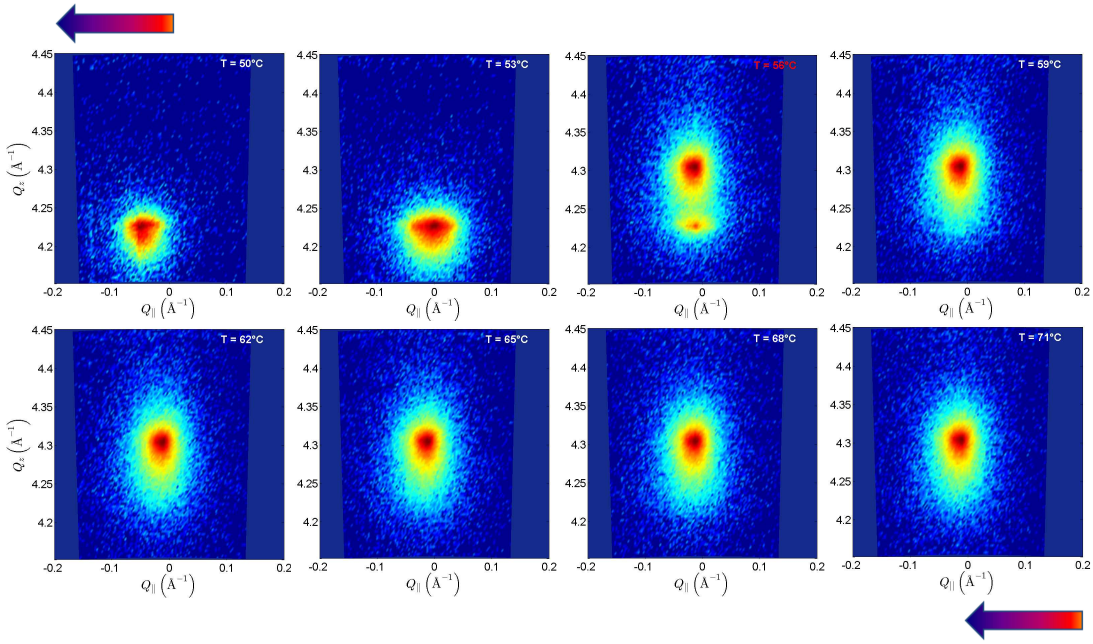

(b) A temperature dependence of the 040 reciprocal space map during cooling.

Figure 5.15: A temperature dependence of the 040 reciprocal space map. The colored arrows indicate the evolution of a temperature between the measurement of the individual reciprocal maps (dark blue indicates low temperatures, red color indicates high temperatures).

tions in reciprocal space than our measured maps. The configuration of optics was following: $\frac{1}{2}$ divergence slit and the hybrid monochromator on the primary beam and the analyzer crystal on the secondary beam. The hybrid monochromator has been chosen to obtain higher intensity, because we loose the half of the primary beam intensity only due to the graphite dome on the sample stage. The resulting reciprocal space maps are depicted in Figure 5.15a for heating and in Figure 5.15b for cooling.

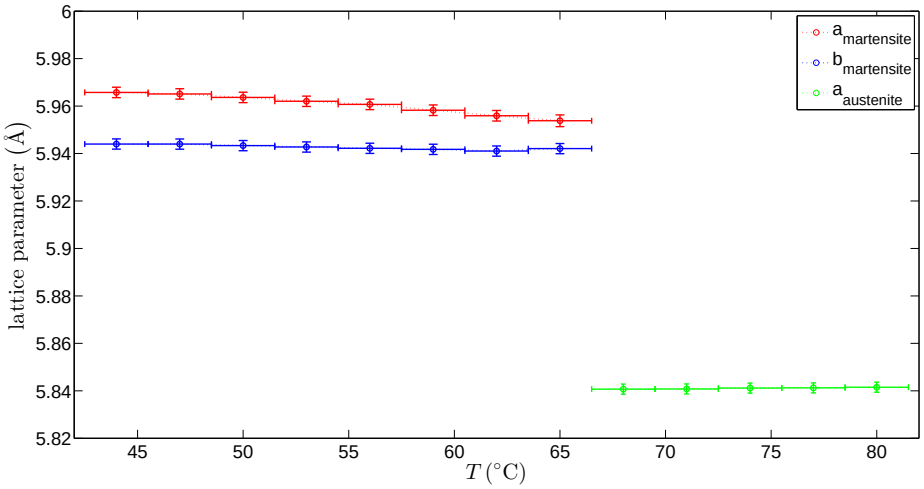

(a) A temperature dependence of the lattice parameters during heating.

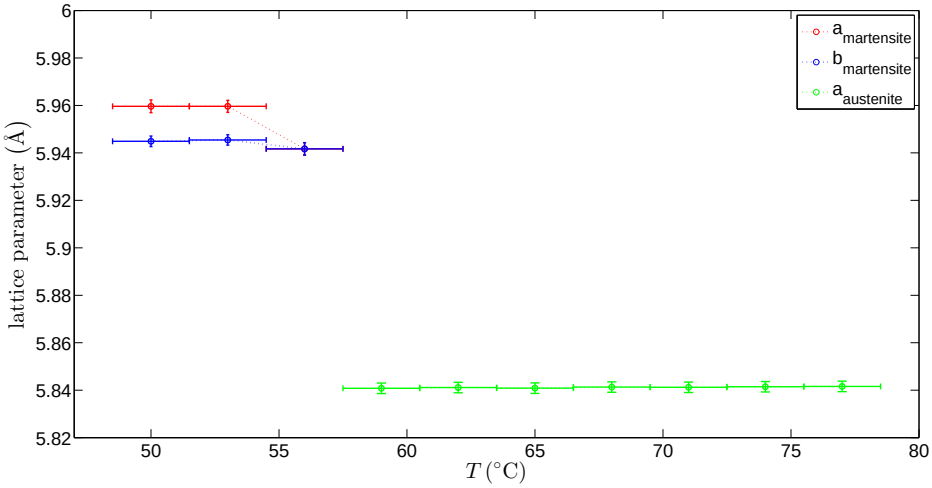

(b) A temperature dependence of the lattice parameters during cooling.

Figure 5.16: A temperature dependence of a rough estimation of the lattice parameters (determination only from positions of diffractions peak 040 and $\overline{4}00$). The vertical error bars have been obtained from statistical deviation of peak positions after the fitting by pseudo-Voigt functions and from experimental error, which has been chosen roughly as the smallest step in 2Θ from our measured maps. The horizontal errorbars should indicate the oscilation of 1-2°C of the set temperature within the measurement. Moreover, according to [43], the values of the temperature are systematicaly shifted. The true temperature of the sample should be about 5 or 6°C lower.

One can see, that transition has a hysteresis in the temperature dependence - the transition occurs at approximately 68°C during heating and at 56°C during cooling. There is a merge of the 040 and 400 peak (corresponding to twinning) at higher temperatures. It shows a fact that a and b axes became to be more equal and the structure is more symetric within a temperature increase. From the positions of indiviual peaks in 2Θ we can roughly estimate the a and b lattice parameters. There is a resulting temperature dependence of the lattice parameters in Figure 5.16a for heating and in Figure 5.16b for cooling.

But according to [43], there is different temperature on the sample with respect to the set temperature. In vacuum and at temperatures held in our measurement, the sample should be about 5 or 6°C colder than the holder with the heater (set temperature is should be on the holder). This fact leads to the systematic shift of our temperatures. Therefore, the abovementioned hysteresis corresponds to the transition temperature of about 63°C during heating and about 51°C during cooling. This hysteresis is in a quite good agreement with the position of the hysteresis loop in magneto-optical study [39], where the dependence of saturated magnetisation with respect to a temperature has been studied.

When the temperature was set at 71°C (above the transition temperature), I have performed measurement of a set of different reciprocal space maps like in previous section. As in previous case, I have obtained the lattice parameter by a numerical solution of Equations 5.1. The resulting lattice parameter of austenite cubic lattice is (5.8386 ± 0.0004) Å. I have proccesed the data in the same way as

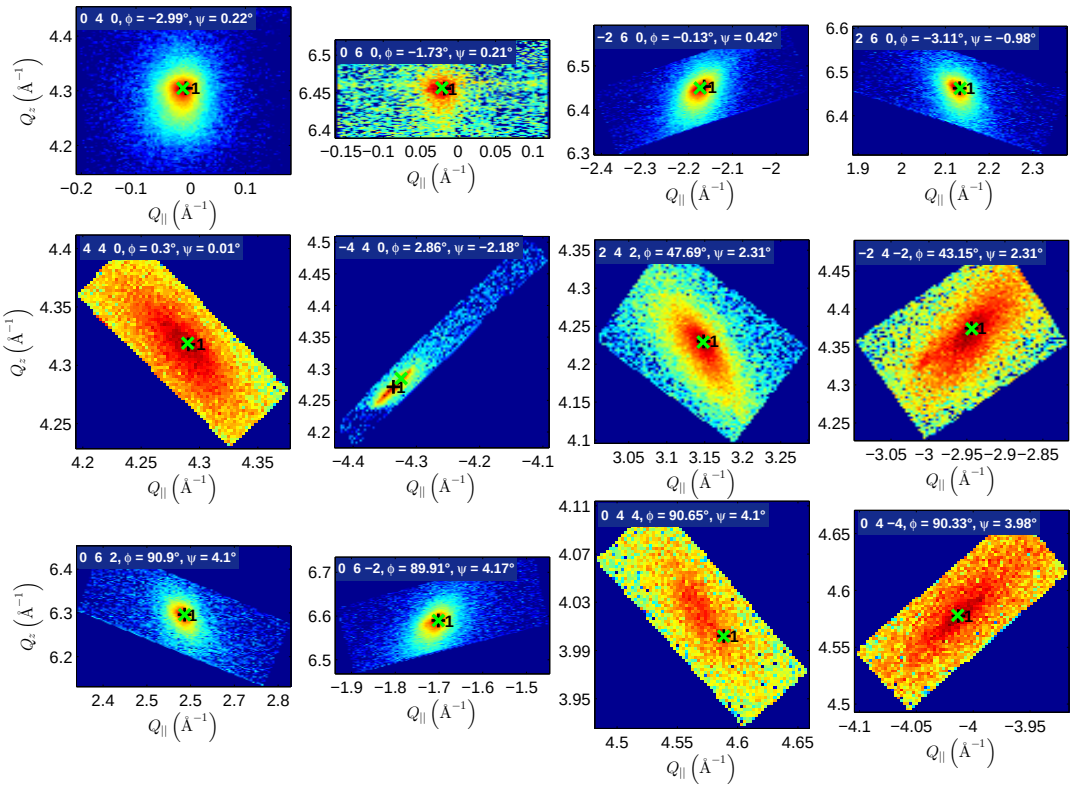

Figure 5.17: Reciprocal space maps corresponding to the austenitic phase measured at 71°C. Black crosses are the measured positions of diffraction maxima, green crosses correspond to the computed ones.

well to obtain the orientation of the lattice with respect to diffractiometer system and following comparison of the measured and computed position of diffractions. The result is depicted in Figure 5.17.

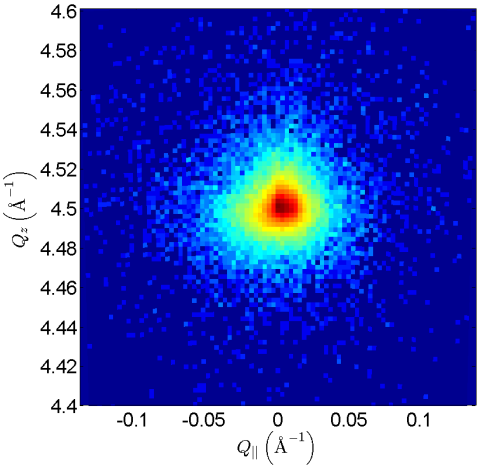

Figure 5.18: Reciprocal space map of the diffraction 004 corresponding to the structure, which was induced by application of external magnetic field. The map has been measured at room temperature.

Beside the fact that we are able to induce some domain structure by pressure, inner structure of Ni-Mn-Ga alloys can be changed by an application of external magnetic field. Thereby, the twin boundaries can be well shifted [44]. If we set the magnetic field in the specified direction, we can swap the crystallographic axes as well. We have applied the magnetic field of value approximately 1 T perpendicular to the largest side of our sample. Because one end of the sample was shielded by holder within a magnetic field application, a small strip of original domain (where the *b*-axis is perpendicular to the largest side) left in the sample - the domain boundaries are usually visible only by naked eye (one can see [45]). In the rest of the sample we obtain the structure, where *c*-axis points along the direction of magnetic field applied before - a measurement prooved this fact (result in Figure 5.18), because diffraction 004 corresponds to the higher value of 2Θ than diffraction 040.

A temperature-based measurement of diffraction 004 reciprocal space maps has been performed too. We have used the same optics configuration as in previous case. Results can be seen in Figure 5.19a and 5.19b. One can see a fast shift of the 004 diffraction peak (compare with Figure 5.15a) with respect to the increasing temperature. That indicates the anisotropy of the thermal expansion coeficients with respect to the crystallographical axes.

The hysteresis found in previous case occurs in different temperatures here. It is probably due to the existence of the strip of original domain on the end of the sample. Moreover, this small strip (lets say $\frac{1}{10}$ of the sample) was enough to return the whole sample to the original structure with *b*-axis pointing from the largest side of the sample - the diffraction peaks corresponding to the twinned domains have occured after transition during cooling (see Figure 5.19b).

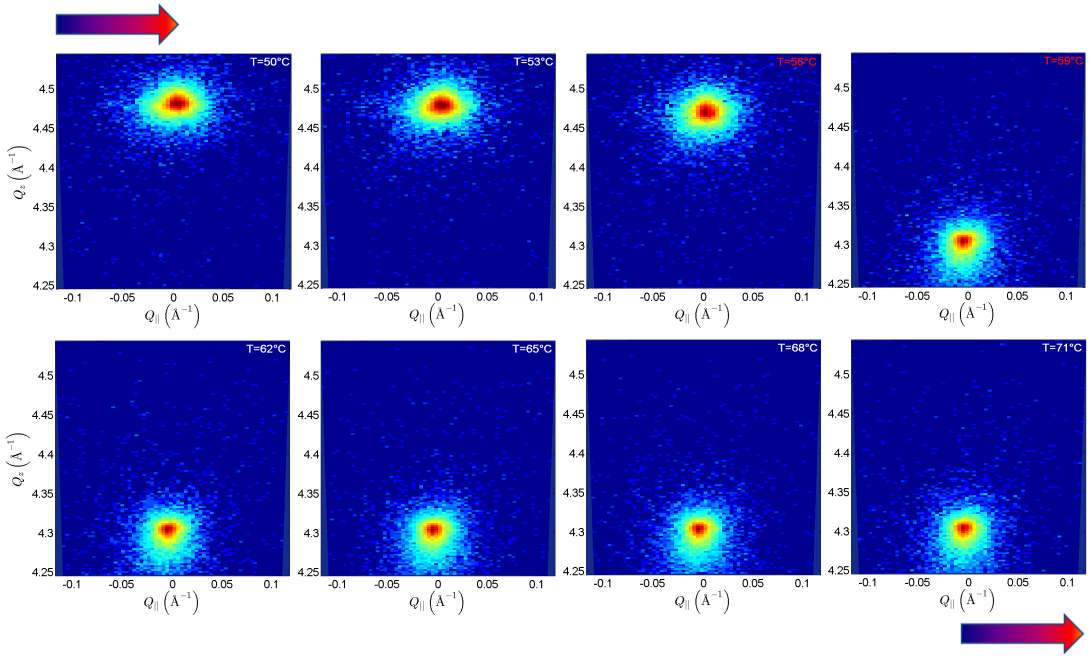

(a) A temperature dependence of the 004 reciprocal space map during heating.

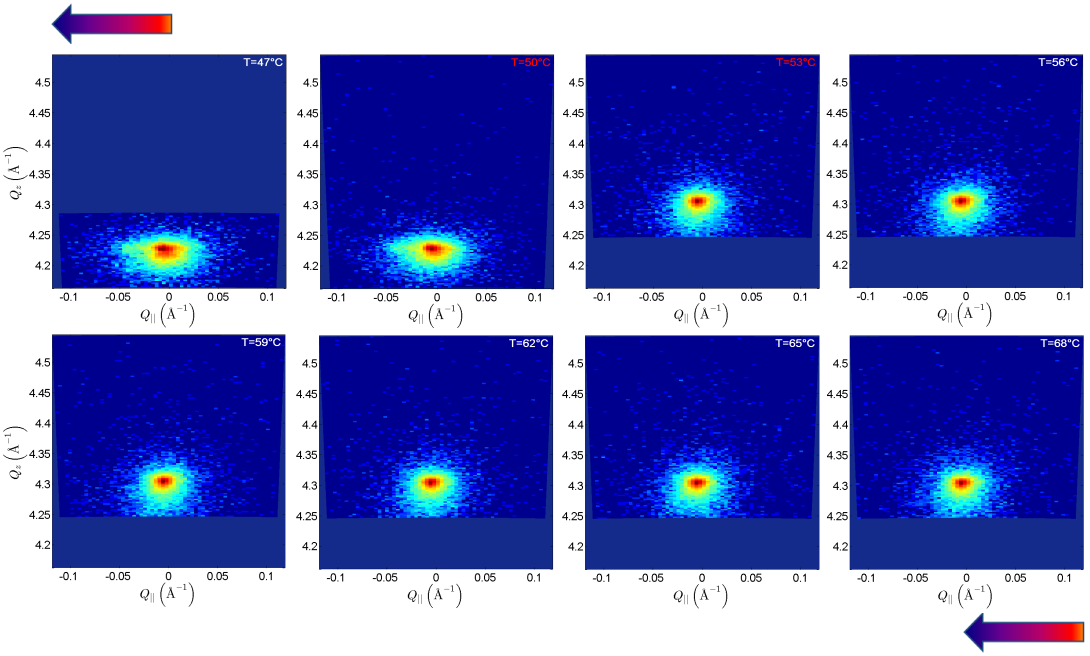

(b) The temperature dependence of the 004 reciprocal space map during cooling.

Figure 5.19: A temperature dependence of the 004 reciprocal space map. The colored arrows indicate evolution of temperature as in previous case.

Discussion and conclusions

The series of powder samples of $Mn_2Co_{1-x}Rh_xSn$ and the single-crystal of shape memory alloy Ni_2MnGa were systematicaly studied for their structure aspects. The goal was to obtain information about possible occupation disorder and other features of their fine structure.

The set of XPD measurement has been performed on the powder samples. From results it follows that $Mn_2Co_{1-x}Rh_xSn$ undergoes a tetragonal distortion aproximatelly at $x = 0.3$, corresponding lattice parameters can be seen in Figure 3.3 and in Table 3.2. Several types of possible occupation disorder (according to [2]) were excluded by the comparison of measured diffraction patterns with simulated patterns, which correspond to the individual models of occupation disorder observed in Heusler alloys. The result is that BiF_3-type of disorder is the only possible type, which can exist in our series of samples.

Following process to obtain an information about disorder has been managed by fitting of the integrated intensities obtained from the measured XPD patterns. Unfortunately, the minimum of the sum of the deviations from the fit is not so deep. The similar values of a residuum have been obtained with other slightly different combinations of the occupation numbers or only by a swap of atomic sites of individual atoms (especially Mn and Co, because they have simillar number of electrons). The results can be seen in Table 3.4. It can be seen that change about 0.3 (without respect to the swapping of the individual atomic sites) in the resulting values of the occupation numbers makes no distinct change in the value of residuum. Therefore, the error in the estimation of the resulting occupation numbers is roughly 0.3. It means, that resulting occupation numbers of the individual types of atoms in the symetricaly equivalent sites ($4a$, $4b$, $4c$ and $4d$) described by the space group $F\overline{4}3m$ have practically the same values. Altought XPD is a good method to obtain qualitative information about the type of occupation disorder (because of missing peaks in XPD patterns corresponding to different symetry of disordered structure), it is necessary to choose another method to obtain other quantitative information about disorder.

EXAFS has been choosen as another experimental method, because it is very sensitive to the closest neighbourhood of specified atoms. The results show that disorder is present in some of our samples, but the structure is not fully disordered and it should be in some state between the full disorder and idealy ordered structure. I was trying to take this into account by consideration of the degree of disorder δ (see Equations 4.1). Values of δ has been obtained by the fitting of measured EXAFS data and weightening the spectra corresponding to the non-disordered and fully-disordered structures. Results can be seen in Table 4.1. It seems that the resulting values of δ do not correspond to the increasing amount of rhodium in the samples. If the disorder originate in a preparation, it would be valuable to perform the measurement on annealed samples.

As one can see from Figure 4.4, contributions of our first and second coordination shell overlap mutually each other. This is may lead to a fact that the error of estimated δ are possibly undervalued. Therefore, better results and the easier data processing would be obtained on Heusler alloys, which have a bigger unit cell and corresponding lattice parameters - the contributions of individu-

al coordination shells should be easier to separate. However, the disorder must be present in the studied samples, because I was not able to fit EXAFS data without a disorder consideration. The values obtained from that fits were not physicaly reasonable (mean square displacements were less than 0, displacements corresponding to heavier atoms were smaller than displacements corresponding to light ones). The comparison of the occupation numbers obtained from XPD and from the EXAFS measurement is shown in Table 4.2. It seems that the values obtained from XPD correspond rather to the state of full occupation disorder, because the occupancies are closely to the corresponding values in Table 1.1. Anyway, it is clearly seen that the occupation disorder with the big degree is present in the sample with $x_{\mathrm{Rh}}^{th} = 0.3$.

The single-crystalline specimen of shape memory alloy Ni_2MnGa has been studied by reciprocal space mapping. Single-crystal diffraction led to a fact that structure of our sample is monoclinic (see Section 5.1). This corresponds with the fact that exact composition of our sample was off-stoichiometric $Ni_{50.1}Mn_{28.4}Ga_{21.5}$. The measured reciprocal space maps contained more than one maxima, which can be well explained by the mosaicity and the twinning. The second mentioned is a well observed phenomenon in Ni-Mn-Ga alloys [40, 44].

Literature points on the existence of a modulation in the structure (5-layered and 7-layered types), which leads to satelite diffractions with non-integer hkl indices [17, 38]. The existence of th modulation in our sample has been proven by another reciprocal space maps measurement, which is graphicaly shown in Figure 5.8. Because of four diffraction maxima between the pairs of proper diffraction spots, we have the 5-layered type of structure in our case. The modulation can be described by the harmonic wave 5.2, which coefficients have been obtained by the fitting of the integrated intensities of measured satelite maxima (see Table 5.2). The coefficients following from my experimental data differs from those from literature - this fact is probably caused by different compositon of our sample.

The high-temperature measurements of reciprocal space maps has been performed as well. They show the existence of more symetric high-temperature structure phase (austenite) according to the literature [16]. The structure is cubic and its lattice parameter has been estimated as (5.8386 ± 0.0004) Å. The measurement shows that the structure transition has hysteresis with respect to temperature. The transition occurs at 68°C during heating and at 56°C during cooling. Resulting reciprocal space maps can be seen in Figure 5.15a and 5.15b. One could try to evaluate, if the change in the $Q_{||}$ (resp. ω) position of the peak 040 corresponds to the change in γ angle within the transition. But, I found out, that it is impossible in our case - position in ω depends strongly on that fact, how we fix a sample on a holder. In the case of measurement at higher temperatures, sample is held only by iron wires. At one attempt of this measurement, the thermomechanical forces, which occurs within the transition, were able to push the sample out from the holder (and we lost the diffraction spot). Therefore, it is obvious that the shift in the $Q_{||}$ position of diffraction 040 can be caused by the change of γ angle, but by the shift on the sample stage as well.

Finally, the crystallographic axis in our sample were swaped by an application of external magnetic field (approx. 1 T perpendicular to the largest side of our sample). Then, c-axis pointed along the direction of used field. After that, I was able to measure a temperature dependence of the diffraction 004, which

could not be reached before. The resulting reciprocal space maps can be seen in Figure 5.19a and 5.19b. The difference between the position of hysteresis found by the position of diffraction 004 and 040 (resp. $\overline{4}00$) measured before should correspond to the existence of the original structure state in the sample after magnetic field application. This part of sample could be distinguished with the naked eye, because of visibility of domain boundaries (analogical example in [45]). Size of this part was approximately $\frac{1}{10}$ of whole sample. But it seems that it was enough to set structure back to original state (b-axis is perpendicular to the largest side) after cooling, because diffraction peak 004 has vanished (see Figure 5.19b).

Some of the results mentioned above have been used to publish the article [39], which has been made with a collaboration of the magneto-optical group in our faculty.

A Matlab scripts

Fit of the integrated intensities from XPD measurement, generation of the disordered unit cells (IntegratedIntensityFit.m)

```
% Script for the fitting of integrated intensities measured by XPD
% on two different wavelengths.

clear all
close all

%%% INPUT %%%%%%%%%%%%%%%%%%%
N_gen=1e4; % number of generated unit cells
T=293; % temperature in Kelvins
dop=0.3; % doping
sys='cubic'; % crystallographic system

cthm_1=0.7998; % cos(2th) of monochromator
cthm_2=0.7998; % cos(2th) of monochromator
lam_1=1.54056; % CuK_alpha
lam_2=1.788965; % CoK_alpha

% Reading of the data files
data1=load('OM103_Cu.dat');
hkl=data1(:,1:3);
th2_1=data1(:,4);
Intensities_1=data1(:,5);

data2=load('OM103_Co.dat');
th2_2=data2(:,4);
Intensities_2=data2(:,5);
%%%%%%%%%%%%%%%%%%%%%%%%%%%

% types of atoms
atoms.type={'Mn';'Sn';'Co';'Rh';'Mn';'Sn';'Co';'Rh';
            'Mn';'Sn';'Co';'Rh';'Mn';'Sn';'Co';'Rh';
            'Mn';'Sn';'Co';'Rh';'Mn';'Sn';'Co';'Rh';
            'Mn';'Sn';'Co';'Rh';'Mn';'Sn';'Co';'Rh';
            'Mn';'Sn';'Co';'Rh';'Mn';'Sn';'Co';'Rh';
            'Mn';'Sn';'Co';'Rh';'Mn';'Sn';'Co';'Rh';
            'Mn';'Sn';'Co';'Rh';'Mn';'Sn';'Co';'Rh';
            'Mn';'Sn';'Co';'Rh';'Mn';'Sn';'Co';'Rh';};

% atomic sites in the unit cell
atoms.positions=[0 0 0; 0 0 0; 0 0 0; 0 0 0;
              1/2 1/2 0; 1/2 1/2 0; 1/2 1/2 0; 1/2 1/2 0;
              0 1/2 1/2; 0 1/2 1/2; 0 1/2 1/2; 0 1/2 1/2;
              1/2 0 1/2; 1/2 0 1/2; 1/2 0 1/2; 1/2 0 1/2;
              1/2 1/2 1/2; 1/2 1/2 1/2; 1/2 1/2 1/2; 1/2 1/2 1/2;
              1/2 0 0; 1/2 0 0; 1/2 0 0; 1/2 0 0;
              0 1/2 0; 0 1/2 0; 0 1/2 0; 0 1/2 0;
              0 0 1/2; 0 0 1/2; 0 0 1/2; 0 0 1/2;
              1/4 1/4 1/4; 1/4 1/4 1/4; 1/4 1/4 1/4; 1/4 1/4 1/4;
              3/4 3/4 3/4; 3/4 3/4 3/4; 3/4 3/4 3/4; 3/4 3/4 3/4;
              3/4 1/4 1/4; 3/4 1/4 1/4; 3/4 1/4 1/4; 3/4 1/4 1/4;
              1/4 3/4 1/4; 1/4 3/4 1/4; 1/4 3/4 1/4; 1/4 3/4 1/4;
              1/4 1/4 3/4; 1/4 1/4 3/4; 1/4 1/4 3/4; 1/4 1/4 3/4;
```

```
53              3/4 3/4 1/4; 3/4 3/4 1/4; 3/4 3/4 1/4; 3/4 3/4 1/4;
54              3/4 1/4 3/4; 3/4 1/4 3/4; 3/4 1/4 3/4; 3/4 1/4 3/4;
55              1/4 3/4 3/4; 1/4 3/4 3/4; 1/4 3/4 3/4; 1/4 3/4 3/4;];
56
57 % all occupancies are zero at the beginning of simulation
58 atoms.occ=zeros(size(atoms.type));
59
60 % dispersion corections
61 for k=1:length(atoms.type)
62     [atoms.f1(k),atoms.f2(k)]=DispCorrF1F2(atoms.type{k}, ...
63             12398.41815/lam_1);
64 end
65
66 atoms2=atoms;
67 for k=1:length(atoms.type)
68     [atoms2.f1(k),atoms2.f2(k)]=DispCorrF1F2(atoms2.type{k}, ...
69             12398.41815/lam_2);
70 end
71
72 %%% GUESS OF PARAMETERS %%%%%%%%
73 weight=Intensities_2(3)/Intensities_1(3);
74 par0=[3e-4 6e-5 200]; % [scale1 a 2, Debye temperature]
75 lb=[0 0 30]; % lower bounds
76 ub=[1e4 1e4 1000]; % upper bounds
77
78 %%% GENERATION OF OCCUPANCY %%%%%%
79 % space group P1
80 % total amount of atoms to distribute
81 %       - they are 16 in one unit cell
82 am_Mn=8;
83 am_Sn=4;
84 am_Co=(1-dop)*4;
85 am_Rh=dop*4;
86
87 list=zeros([N_gen,length(atoms.occ')+length(par0)+1]);
88 for n=1:N_gen
89     disp(n); % it prints the actual number of n
90
91     % starting values
92     am_Mn=8;
93     % am_Sn=4;
94     am_Co=(1-dop)*4;
95     am_Rh=dop*4;
96     atoms.occ=zeros(size(atoms.type));
97
98     % we go over all position until the sum of occupation numbers
99     % in individual positions is equal to 1
100    positions=1:16;
101    positions2=ones(size(positions));
102    while sum(positions2)>0
103        % list of positions, which have not been filled yet
104        rest=positions(positions2==1);
105        % generation of the position number to fill it
106        %       - it should avoid to prefer any position
107        kk=round((length(rest)-1)*rand)+1;
108        k=rest(kk);
109        positions2(k)=0;
110        % total occupancy in one position has not be bigger than 1
```

```
111         while round(10*(atoms.occ(4*k-3)+atoms.occ(4*k-2)+...
112                     atoms.occ(4*k-1)+atoms.occ(4*k)))/10<1
113             if k<5
114                 atoms.occ(4*k-3)=0;
115                 atoms.occ(4*k-2)=1;
116                 atoms.occ(4*k-1)=0;
117                 atoms.occ(4*k)=0;
118             else
119             % generation of 4 numbers (4 types of atoms)
120             hlp=[(1:4)', [2*rand; 0; (1-dop)*rand; dop*rand]];
121             [w,j]=sort(hlp(:,2)); % sorting of generated numbers
122             % site corresponding to the smallest generated number
123             % will be filled
124             type=hlp(j,:);
125             switch type(4,1)
126                 case 1
127                     if round(10*am_Mn)/10>0
128                         am_Mn=am_Mn-0.1;
129                         atoms.occ(4*k-3)=atoms.occ(4*k-3)+0.1;
130                     end
131                 % case 2 - case of Sn - solved before
132                 case 3
133                     if round(10*am_Co)/10>0
134                         am_Co=am_Co-0.1;
135                         atoms.occ(4*k-1)=atoms.occ(4*k-1)+0.1;
136                     end
137                 case 4
138                     if round(10*am_Rh)/10>0
139                         am_Rh=am_Rh-0.1;
140                         atoms.occ(4*k)=atoms.occ(4*k)+0.1;
141                     end
142             end
143             end
144         end
145     end
146     atoms2.occ=atoms.occ;
147
148     % Fitting
149     [parT,Feval]=fminsearchbnd(@(x) ...
150             sum((weight*Intensities_1-x(1)*MyFun(hkl,th2_1,...
151                     cthm_1,atoms,1,sys,lam_1,T,x(3))).^2)+...
152             sum((Intensities_2-x(2)*MyFun(hkl,th2_2,cthm_2,...
153                     atoms2,1,sys,lam_2,T,x(3))).^2),par0,lb,ub);
154
155     % List of results
156     list(n,:)=[atoms.occ',parT,Feval];
157 end
158
159 %%% sorting of the list with respect to the value of residui
160 [w,j]=sort(list(:,size(list,2)));
161 list_T=list(j,:);
162
163 %%% Result with the smallest residuum
164 atoms.occ=list_T(1,1:length(atoms.occ));
165 parT=list_T(1,length(atoms.occ)+1:size(list,2)-1);
166 Feval=list_T(1,size(list,2));
167
168 %%% PLOTTING %%%%%%%%%%%%%%%%%
```

```
figure(1)
plot(th2_1,Intensities_1,'bo-',th2_1,parT(1)/weight*MyFun(hkl,...
        th2_1,cthm_1,atoms,1,sys,lam_1,T,parT(3)),'ro-');
xlabel('$$2\Theta \left[^\circ\right]$$','Interpreter','latex');
ylabel('Integrate intensity $$\left[\textrm{a.u.}\right]$$',...
        'Interpreter','latex');
title('Measurement on CuK$$_{alpha}$$','Interpreter','latex');

figure(2)
plot(th2_2,Intensities_2,'bo-',th2_2,parT(2)*MyFun(hkl,...
        th2_2,cthm_2,atoms2,1,sys,lam_2,T,parT(3)),'ro-');
xlabel('$$2\Theta \left[^\circ\right]$$','Interpreter','latex');
ylabel('Integrate intensity $$\left[\textrm{a.u.}\right]$$',...
        'Interpreter','latex');
title('Measurement on CoK$$_{alpha}$$','Interpreter','latex');

%%% REPORT %%%%%%%%%%%%%%%%%%
disp(Feval);
disp(list_T(1:5,:))
```

Function for integrated intensities, which is used within the fitting (MyFun.m)

```
function y=MyFun(hkl,th2,cthm,atoms,N,sys,lam,T,ThD)
% Script computes an integrated intensity.
% hkl - hkl indices of diffractions
% th2 - 2theta positions of measured diffractions
% cthm - cos(2th_M) of monochromator
% atoms - struc type of variable
%       atoms.type ... cell array with names of atoms/ionts
%       atoms.occ ... occupation numbers
%       atoms.positions ... fractional coordinates of atoms
%       atoms.f1, atoms.f2 ... dispersion corrections
%       atoms.B ... temperature factors
% N - scale
% sys - crystallographic system
% lam - wavelength
% T - temperature
% ThD - Debye temperature

% Lorenz and polarisation factor
L_p=(1+cthm*(cos(th2*pi/180)).^2)./(1+cthm).*...
        1./(sin(th2*pi/180).*sin(th2*pi/360));

% Structure factor
F=StrucFactor(hkl,th2,lam,atoms,T,ThD);

% p_hkl is a multiplicity of diffraction
y=N.*L_p.*abs(F).^2.*p_hkl(hkl,sys);
```

Structure factor evaluation (StrucFactor.m)

```
function y=StrucFactor(hkl,th2,lam,atoms,T,ThD)
% Function y=StrucFactor(hkl,th2,lam,atoms,T,ThD)
% returns the structure factor.
% hkl - indices of diffractions
% th2 - 2theta positions of diffractions
% lam - used wavelength of x-rays
% atoms.positions - positions of the atoms in the unit cell
%         .occ - occupation numbers
%         .f1, .f2 - dispersion corrections
%         .type - types of the atoms
% T, ThD - temperature and Debye temperature

% prelocation before a sumation
hlp=zeros(size(hkl,1),1);

% temperature factor - if the temperature and Debye temperature
% are specified, B factors is computed by them
if nargin>4
    atoms.B=DWTF(atoms.type,T,ThD);
end

% sumation over atoms in the unit cell
for k=1:length(atoms.type)
    hlp=hlp+...
        (ScatFacF0(atoms.type{k},sin(th2*pi/360)/lam)+...
                atoms.f1(k)+1i*atoms.f2(k)).*...
        atoms.occ(k).*...
        exp(-atoms.B(k).*(sin(th2*pi/360)/lam).^2).*...
        exp(-2*pi*i*(hkl(:,1).*atoms.positions(k,1)+...
                hkl(:,2).*atoms.positions(k,2)+...
                hkl(:,3).*atoms.positions(k,3)));
end
y=hlp;
```

Change of FEFF input with respect to disorder (MakeDisorder.m)

```
% The script, which will read the file with cluster of atom
% generated for the FEFF input - originaly ideal
% non-disordered structure will be edited with respect
% to the degree of disorder. Core atom will stay original.

close all
clear all

%%% INPUT %%%%%%%%%%%%%%%%%%
name_in='feff.inp'; % name of the file with original input
name_ex='disorder.inp'; % name of the file to edit

del=1; % degree of disorder
X='Mn'; ipotX=2; % labels of atoms corresponding to original file
Y='Rh'; ipotY=3; % labels of atoms corresponding to original file
%%%%%%%%%%%%%%%%%%%%%%%%%
```

```
17
18 occ4b_X=1-del/3; occ4b_Y=del/3;
19 occ4c_X=2*del/3; occ4c_Y=1-2*del/3;
20 occ4d_X=1-del/3; occ4d_Y=del/3;
21
22 % opening for the reading and writting
23 file1=fopen(name_in,'r');
24 file2=fopen(name_ex,'w');
25
26 counter=-1;
27 change=0;
28 while 1
29     string=fgets(file1); % reading of the line
30
31     if length(string)>5 & all(string(2:6)=='ATOMS')
32         counter=0;
33     end
34
35     if length(string)>3 & all(string(2:4)=='END')
36         fprintf(file2,string); % writting
37         fclose(file1);
38         fclose(file2);
39         break
40     end
41
42     % counter, which is switched on at the beginning of atoms list
43     if counter>=0 & length(string)>2
44         counter=counter+1;
45         % the first line corresponds to the headlines,
46         % the second to the core atom
47         if counter>2
48             % manganese at 4b site in ideal structure
49             % will be replaced
50             if all(string(36:42)==[num2str(ipotX) ,'  ',X,'4b'])
51                 hlp=rand(1);
52                 if hlp<occ4b_Y
53                     string(36:42)=[num2str(ipotY),'  ',Y,'4b'];
54                     change=change+1;
55                 end
56             end
57             % cobalt at 4c site in ideal structure
58             % will be replaced
59             if all(string(36:42)==[num2str(ipotY),'  ',Y,'4c'])
60                 hlp=rand(1);
61                 if hlp<occ4c_X
62                     string(36:42)=[num2str(ipotX),'  ',X,'4c'];
63                     change=change+1;
64                 end
65             end
66             % manganese at 4d site in ideal structure
67             % will be replaced
68             if all(string(36:42)==[num2str(ipotX),'  ',X,'4d'])
69                 hlp=rand(1);
70                 if hlp<occ4d_Y
71                     string(36:42)=[num2str(ipotY),'  ',Y,'4d'];
72                     change=change+1;
73                 end
74             end
```

```
        end
    else
        counter=-1;
    end

    fprintf(file2,string); % writting

end

disp(['Number of changes: ' num2str(change)]);
```

Fit of the integrated intensities of satelites peaks caused by a structure modulation (ModulationFit.m)

```
% Script for the fitting of the integrated intensities of satelite
% peaks caused by modulation in the structure

close all
clear all

lam=1.54056; % used wavelength

%%% FIT OF THE LOGARITHM OF INTENSITIES? %%%
log_fit=1; % 1 if yes, 0 if no
%%% GUESS %%%%%%%%%%%%%%%%%%%%%%
A_n=[0.07 -0.002 0]; % amplitudes of the harmonical function
L=5; % period of modulation
N=0.1; % scale factor
bgr=0.5; % background
B=1; % Debye-Waller temperature factor

par0=[A_n, N, bgr, B];

% lower bounds
lb(1:3)=[0.00 -0.030 -0.010];
lb(4)=0;
lb(5)=0;
lb(6)=0;

% upper bounds
ub(1:3)=[0.15 0.030 0.010];
ub(4)=1e3;
ub(5)=10;
ub(6)=5;

%%% LOADING OF MEASURED DATA %%%%%%%%
hkl(:,:,1)=[0 4 0;
            0.4 4.4 0;
            0.8 4.8 0;
            1.2 5.2 0;
            1.6 5.6 0;
            2 6 0;
            1.6 6.4 0;
            1.2 6.8 0;];

```

```
Intensities(:,1)=[299.6039321; % 040
                  27.02710817; % 0.4 4.4 0
                  0.828013474; % 0.8 4.8 0
                  0.612932801; % 1.2 5.2 0
                  15.55226308; % 1.6 5.6 0
                  105.7475566; % 2 6 0
                  21.07043308; % 1.6 6.4 0
                  3.29658631;]; % 1.2 6.8 0

th2(:,1)=[62.4;
          70.2;
          78.2;
          87.9;
          97.7;
          109.7;
          117.2;
          126.7;];

om(:,1)=[28.5;
         26.75;
         26.8;
         28;
         30.2;
         33.7;
         47.3;
         56.1;];

%%%%%%%%%%%%%%%%%%%%%%%%%%%%
% SOME  CALCULATION BEFORE FIT %%%%%%%
% The structure will be discribed by unit cell, which is rotated
% about 45deg around c-axis => this easier way for the modulation
% description, because the direction of modulation is [110]

% position of atoms in non-distorted unit cell
atoms.positions=[0 0 0;
                 1/2 1/2 1/2;
                 0 1/2 1/4;
                 1/2 0 1/4;
                 0 1/2 3/4;
                 1/2 0 3/4;
                 1/2 1/2 0;
                 0 0 1/2;];
% corresponding types of atoms
atoms.type={'Ga';
            'Ga';
            'Ni';
            'Ni';
            'Ni';
            'Ni';
            'Mn';
            'Mn';};
% transformation of diffraction indices
hkl_new=[(hkl(:,1,:)+hkl(:,2,:))/2,...
         (-hkl(:,1,:)+hkl(:,2,:))/2,...
         hkl(:,3,:)];

% refraction index obtained from X0h search
RefInd=1-0.22352e-4+i*0.10018e-5;
```

```
% dispersion correction
for k=1:length(atoms.type)
    [atoms.f1(k,1),atoms.f2(k,1)]=DispCorrF1F2(atoms.type{k},...
                                                12398.41815/lam);
end

%%%%%%%%%%%%%%%%%%%%%%%%%%%%
%%% FITTING %%%%%%%%%%%%%%%%%%%%
options=optimset('display','iter','maxfunevals',1e6,'maxiter',1e6);
if log_fit==1
    [parT,Feval]=fminsearchbnd(@(x)...
          sum((log(Intensities)-log(MyFun2(x,hkl_new,L,th2,om,...
          RefInd,atoms,lam))).^2),par0,lb,ub,options);
else
    [parT,Feval]=fminsearchbnd(@(x)...
          sum((Intensities-MyFun2(x,hkl_new,L,th2,om,...
          RefInd,atoms,lam)).^2),par0,lb,ub,options);
end
%%%%%%%%%%%%%%%%%%%%%%%%%%%%
%%% ERRORS ESTMATION %%%%%%%%%%%%%
% prelocation of Jacobian
J=zeros([length(Intensities),length(parT)]);
for j=1:length(Intensities)
    for k=1:length(parT)
        eta=1e-9;
        par=parT;
        par(k)=par(k)+eta;
        hlp1=log(MyFun2(parT,hkl_new,L,th2,om,...
                    RefInd,atoms,lam));
        hlp2=log(MyFun2(par,hkl_new,L,th2,om,...
                    RefInd,atoms,lam));

        J(j,k)=(hlp1(j)-hlp2(j))/eta;
    end
end
% statistical error
err_st=sqrt(diag(Feval*inv(J'*J)/...
            (length(Intensities)-length(parT))))';

%%% PRINT %%%%%%%%%%%%%%%%%%%%
disp(['A_1: ' num2str(parT(1)) ' +/- ' num2str(err_st(1))]);
disp(['A_2: ' num2str(parT(2)) ' +/- ' num2str(err_st(2))]);
disp(['A_3: ' num2str(parT(3)) ' +/- ' num2str(err_st(3))]);
disp(['period: ' num2str(L)]);
disp(['scale: ' num2str(parT(4))  ' +/- ' num2str(err_st(4))]);
disp(['bgr: ' num2str(parT(5))  ' +/- ' num2str(err_st(5))]);
disp(['DWTF: ' num2str(parT(6))  ' +/- ' num2str(err_st(6))]);
disp(['resnorm: ' num2str(Feval)]);

Int_0=MyFun2(par0,hkl_new,L,th2,om,RefInd,atoms,lam);
Int_T=MyFun2(parT,hkl_new,L,th2,om,RefInd,atoms,lam);

%%% PLOTS %%%%%%%%%%%%%%%%%%%%
% Intensities
for k=1:length(N)
    figure(k)
    stem(Intensities(:,k),'b*','MarkerSize',8,...
                              'display','Measurement');
```

```
158     hold on
159         stem(Int_0(:,k),'k','MarkerSize',3,'display','Guess');
160         stem(Int_T(:,k),'r','display','Fit');
161     hold off
162 end
163 
164 % Modulation wave
165 figure()
166 x=linspace(0,L,512);
167 plot(x,par0(1)*sin(2*pi*x/L)+par0(2)*sin(2*pi*2*x/L)+...
168                  par0(3)*sin(2*pi*3*x/L),'k',...
169      x,parT(1)*sin(2*pi*x/L)+parT(2)*sin(2*pi*2*x/L)+...
170                  parT(3)*sin(2*pi*3*x/L),'r');
```

Function computing integrated intensities by the crystal with modulated structure (MyFun2.m)

```
1  function y=MyFun2(par,hkl,L,th2,om,RefInd,atoms0,lam)
2  % Function y=MyFun2(par,hkl,L,th2,om,RefInd,atoms0,lam)
3  % returns the value of integrated intensities corresponding
4  % to the modulated structure determined by parameters
5  % A_n and L.
6  % par - free parameters
7  % hkl - indices of the diffractions
8  % th2, om - angular coordinations of the diffractions
9  % L - period of the modulation
10 % RefInd - refraction index of the material
11 % lam - used wavelength
12 % atoms.type - types of atoms in the original unit cell
13 %       .positions - positions of atoms in the original unit cell
14 %       .f1, .f2 - dispersion corrections
15 
16 A_n=par(1:3); % amplitudes of the harmonical function
17 N=par(4); % scale factor
18 bgr=par(5); % background
19 B=par(6); % Debye-Waller temperature factor
20 
21 Cthm=0.7998; % cos(2th) of monochromator
22 r_el=2.81794e-5; % classical radius of electron
23 
24 %%% MODULATION %%%%%%%%%%%%%%%%%%
25 atoms=Modulation(atoms0,A_n,L);
26 
27 % prelocation of structure factor before sumation
28 F=zeros([size(hkl,1) 1]);
29 for k=1:size(atoms.positions,1)
30     F=F+...
31       (ScatFacF0(atoms.type{k},sin(th2*pi/360)/lam)+...
32                  atoms.f1(k)+i*atoms.f2(k)).*...
33       exp(-2*pi*i*(hkl(:,1)*atoms.positions(k,1)+...
34                  hkl(:,2)*atoms.positions(k,2)+...
35                  hkl(:,3)*atoms.positions(k,3)));
36 end
37 
38 P=(1+Cthm*cos(th2*pi/180).^2)/(1+Cthm); % polarisation factor
```

```
Qiz=2*pi/lam*imag(RefInd).*...
            (1./sin(om*pi/180)+1./sin((th2-om)*pi/180));
S=1./sin(om*pi/180); % irradiated area correction
DWTF=exp(-2*B*(sin(th2*pi/360)/lam).^2); % temperature factor

y=N.*P.*abs(F).^2.*8*pi^3*r_el^2.*DWTF.*S./(2*Qiz)+bgr;
```

Calculation of the modulated structure (Modulation.m)

```
function atoms=Modulation(atoms0,A,L)
% Function atoms=Modulation(atoms0,A,L)
% function returns coordinates and corresponding types of atoms
% after the consideration of modulation in the structure.
% atoms0.type - types of atoms in the original unit cell
%   .positions - positions of atoms in the original unit cell
%   .f1, .f2 - dispersion corrections
% A - amplitudes of the modulation wave
% L - period of the modulation

% number of atoms in non-distorted unit cell
N=size(atoms0.positions,1);

% positions of the atoms in the five neighbouring unit cells
for k=1:L
    pos2((k-1)*N+1:k*N,:)=[atoms0.positions(:,1)+k-1,...
                atoms0.positions(:,2),atoms0.positions(:,3)];
end

% modulation function
fcn=A(1)*sin(2*pi*pos2(:,1)*1/L)+A(2)*sin(2*pi*pos2(:,1)*2/L)+...
            +A(3)*sin(2*pi*pos2(:,1)*3/L);

% distortion of the atomic positions
atoms.positions=[pos2(:,1) pos2(:,2)+fcn pos2(:,3)];

% save of the results
for k=1:L
    atoms.type((k-1)*N+1:k*N,1)=atoms0.type;
    atoms.f1((k-1)*N+1:k*N,:)=atoms0.f1;
    atoms.f2((k-1)*N+1:k*N,:)=atoms0.f2;
end
```

The scripts mentioned above are included in a CD in the attachment together with the corresponding examples of data files. Fundamental and less important scripts used above (such as DispCorr.m, p_hkl.m, etc.) can be found in the CD as well.

Bibliography

[1] Friedrich Heusler. Über magnetische manganlegierungen. *Verhandlungen der Deutschen Physikalischen Gesellschaf*, 1903.

[2] Tanja Graf, Claudia Felser, and Stuart S.P. Parkin. Simple rules for the understanding of Heusler compounds. *Progress in Solid State Chemistry*, 39(1):1 – 50, 2011.

[3] S. O. Mariager, C. Dornes, J. A. Johnson, A. Ferrer, S. Grübel, T. Huber, A. Caviezel, S. L. Johnson, T. Eichhorn, G. Jakob, H. J. Elmers, P. Beaud, C. Quitmann, and G. Ingold. Structural and magnetic dynamics in the magnetic shape-memory alloy Ni_2MnGa. *Phys. Rev. B*, 90:161103, Oct 2014.

[4] S. R. Barman, S. Banik, and Aparna Chakrabarti. Structural and electronic properties of ni_2MnGa. *Phys. Rev. B*, 72:184410, Nov 2005.

[5] Y. Sutou, Y. Imano, N. Koeda, T. Omori, R. Kainuma, K. Ishida, and K. Oikawa. Magnetic and martensitic transformations of NiMnX(X=In,Sn,Sb) ferromagnetic shape memory alloys. *Applied Physics Letters*, 85(19), 2004.

[6] Germany: Kernforschungszentrum Karlsruhe, editor. *Superconductivity in d- and f-band metals*. urldate.

[7] P. Courtois, B. Hamelin, and K. H. Andersen. Production of copper and Heusler alloy Cu $_2$MnAl mosaic single crystals for neutron monochromators. *Nuclear Instruments and Methods in Physics Research A*, 529:157–161, August 2004.

[8] B. Yan and A. de Visser. Half-Heusler topological insulators. *ArXiv e-prints*, October 2014.

[9] C. Felser, V. Alijani, J. Winterlik, S. Chadov, and A.K. Nayak. Tetragonal Heusler compounds for spintronics. *Magnetics, IEEE Transactions on*, 49(2):682–685, Feb 2013.

[10] Claudia Felser, Gerhard H. Fecher, and Benjamin Balke. Spintronics: A challenge for materials science and solid-state chemistry. *Angewandte Chemie International Edition*, 46(5):668–699, 2007.

[11] Yoshio Miura, Kazutaka Nagao, and Masafumi Shirai. Atomic disorder effects on half-metallicity of the full-heusler alloys $Co_2(Cr_{1-x}Fe_x)Al$: a first-principles study. *Phys. Rev. B*, 69:144413, Apr 2004.

[12] Vajiheh Alijani, Olga Meshcheriakova, Juergen Winterlik, Guido Kreiner, Gerhard H. Fecher, and Claudia Felser. Increasing curie temperature in tetragonal Mn2RhSn heusler compound through substitution of Rh by Co and Mn by Rh. *Journal of Applied Physics*, 113(6):–, 2013.

[13] Jürgen Winterlik, Gerhard H. Fecher, Benjamin Balke, Tanja Graf, Vajiheh Alijani, Vadim Ksenofontov, Catherine A. Jenkins, Olga Meshcheriakova, Claudia Felser, Guodong Liu, Shigenori Ueda, Keisuke Kobayashi, Tetsuya Nakamura, and Marek Wójcik. Electronic, magnetic, and structural properties of the ferrimagnet Mn_2CoSn. *Phys. Rev. B*, 83:174448, May 2011.

[14] B. Ravel and M. Newville. Athena, Artemis, Hephaestus: data analysis for x-ray absorption spectroscopy using IFEFFit. *Journal of Synchrotron Radiation 12, 537–541*, pages 537–541, 2005.

[15] S. Singh, V. Petricek, P. Rajput, A. H. Hill, E. Suard, S. R. Barman, and D. Pandey. High-resolution synchrotron x-ray powder diffraction study of the incommensurate modulation in the martensite phase of Ni_2MnGa: Evidence for nearly 7M modulation and phason broadening. *PRB*, 90(1):014109, July 2014.

[16] M.L. Richard, J. Feuchtwanger, S.M. Allen, R.C. O'handley, P. Lázpita, and J.M. Barandiaran. Martensite transformation in Ni-Mn-Ga ferromagnetic shape-memory alloys. *Metallurgical and Materials Transactions A*, 38(4):777–780, 2007.

[17] Kokorin V.V., Martynov, V.V. The crystal structure of thermally- and stress-induced martensites in Ni2MnGa single crystals. *Journal de Physique III*, 2(5):739–749, 1992.

[18] Yoshio Miura, Kazutaka Nagao, and Masafumi Shirai. Atomic disorder effects on half-metallicity of the full-Heusler alloys $Co_2(Cr_{1-x}Fe_x)Al$: a first-principles study. *Phys. Rev. B*, 69:144413, Apr 2004.

[19] Bilbao crystallographic server, Wyckoff positions. [online], `http://www.cryst.ehu.es/cryst/get_wp.html`, Last visit 12. 3. 2015.

[20] Gerhard H. Fecher, Sabine Wurmehl, Hem C. Kandpal and Claudia Felser. Valence electron rules for prediction of half-metallic compensated-ferrimagnetic behaviour of Heusler compounds with complete spin polarization. *J. Phys.: Condens. Matter*, 18:6171–6181, 2006.

[21] S. Skaftouros, K. Özdoğan, E. Şaşıoğlu, and I. Galanakis. Generalized slater-pauling rule for the inverse Heusler compounds. *PRB*, 87(2):024420, jan 2013.

[22] Léon Van Hove. The occurrence of singularities in the elastic frequency distribution of a crystal. *Phys. Rev.*, 89:1189–1193, Mar 1953.

[23] H. A. Kierstead, B. D. Dunlap, S. K. Malik, A. M. Umarji, Shenoy, and G. K. Coexistence of ordered magnetism and superconductivity in Pd_2YbSn. *Phys. Rev. B*, 32:135–138, Jul 1985.

[24] Kane C. L.and Mele E. J.. Z_2 topological order and the quantum spin hall effect. *Phys. Rev. Lett.*, 95:146802, Sep 2005.

[25] Polcarová Milena, Lukáč Pavel, Valvoda Václav. *Základy strukturní analýzy*. Nakladatelství a vydavatelství JP, 1992.

[26] McMorrow Des, Als-Nielsen Jens. *Elements of Modern X-ray Physics*. John Wiley & Sons Ltd, 2001.

[27] Holý V. Kinematical diffraction - materials for the lecture of Structure and Diffraction held on the Faculty of mathematics and physics at Charles University in Prague. 2013/2014.

[28] Juan Rodríguez-Carvajal. Fullprof suite [computer software]. `http://www.ill.eu/sites/fullprof/`, 1993-2006.

[29] X-ray absorption edges. [online], `http://skuld.bmsc.washington.edu/scatter/AS_periodic.html`, Last visit 20. 12. 2014.

[30] Demeter, x-ray absorption spectroscopy using FEFF and IFEFFit. [online], `http://bruceravel.github.io/demeter/`, Last visit 20. 12. 2014.

[31] Fundamentals of XAFS. [online], `http://xafs.org/Tutorials?action=AttachFile&do=get&target=Newville_xas_fundamentals.pdf`, Last visit 20. 12. 2014.

[32] Factsage 6.2 - list of stored phase diagrams (2634). [online], `http://www.crct.polymtl.ca/fact/Documentation/All_Figs.htm`, Last visit 9. 2. 2015.

[33] Elliott Rodney P., Shunk Francis A., Hansen Max. *Constitution of binary alloys, first supplement*. McGraw-Hill, Inc., USA, 1965.

[34] Elliott Rodney P., Shunk Francis A., Hansen Max. *Constitution of binary alloys, second supplement*. McGraw-Hill, Inc., USA, 1969.

[35] The artemis user's guide: Handling dopants in FEFF. [online], `http://bruceravel.github.io/demeter/artug/extended/dopants.html`, Last visit 2. 4. 2015.

[36] Shape-memory alloy. [online], `http://en.wikipedia.org/wiki/Shape-memory_alloy`.

[37] J. Pons, V.A. Chernenko, R. Santamarta, and E. Cesari. Crystal structure of martensitic phases in Ni–Mn–Ga shape memory alloys. *Acta Materialia*, 48(12):3027 – 3038, 2000.

[38] L. Righi, F. Albertini, L. Pareti, A. Paoluzi, and G. Calestani. Commensurate and incommensurate "5m" modulated crystal structures in Ni–Mn–Ga martensitic phases. *Acta Materialia*, 55(15):5237 – 5245, 2007.

[39] L. Beran, P. Cejpek, M. Kulda, R. Antos, V. Holy, M. Veis, L. Straka, and O. Heczko. Optical and magneto-optical studies of martensitic transformation in Ni-Mn-Ga magnetic shape memory alloys. *Journal of Applied Physics*, 117(17), 2015.

[40] Ge Yanling. *The Crystal and Magnetic mictostructure of Ni-Mn-Ga Alloys*. PhD thesis, Helsinki University of Technology Doctoral Theses in Materials and Earth Sciences, 2007.

[41] X-ray dynamical diffraction data on the web, X0h. [online], http://x-server.gmca.aps.anl.gov/cgi/WWW_form.exe?template=x0h_form.htm, Last visit 8. 4. 2015, Last modified 16. 12. 2013.

[42] Stokes, A. R. and Wilson, A. J. C.. The diffraction of x rays by distorted crystal aggregates - I. *Proceedings of the Physical Society*, 56(3):174, 1944.

[43] Horák L. - private communication about the calibration for the temperature-based measurement on MRD diffractometer.

[44] S. J. Murray, M. Marioni, S. M. Allen, R. C. O'Handley, and T. A. Lograsso. 6ferromagnetic Ni–Mn–Ga. *Applied Physics Letters*, 77(6), 2000.

[45] NiMnGa. [online], video, https://www.youtube.com/watch?v=wLC0l3HToNg&feature=youtu.be.

List of Tables

1.1 Atomic occupation in fully disordered types of structure 6

2.1 The list of the studied samples 19

3.1 The results of the EDX measurement 20
3.2 The lattice parameters of $Mn_2Co_{1-x}Rh_xSn$ obtained from XPD . 23
3.3 Diffraction peaks missing in XPD patterns due possible disorder . 23
3.4 Occupation in the ideal and generated disordered unit cells 28
3.5 Mean occupancy of the symetricaly equivalent atomic sites 29

4.1 Degrees of disorder following from EXAFS measurement. 35
4.2 Comparison of the occupancies obtained from XPD and EXAFS . 37

5.1 Combination of diff.spots leading to resulting lattice paremeters . 41
5.2 Comparison of the values of A_n with the literature 50

List of Abbreviations

- MSMA(s) - Magnetic Shape Memory Alloy(s)
- EDX - Energy Dispersive X-ray Analysis
- EXAFS - Extended X-ray Absorption Fine Structure
- XRD - X-ray Diffraction
- XPS - X-ray Photo-electron Spectroscopy
- XPD - X-ray powder diffraction
- fcc - face-centered cubic (lattice)
- bcc - body-centered cubic (lattice)
- RE - rare earth
- GMR - giant magnetoresistance
- XAS - X-ray Absorption Spectroscopy

Attachments

- CD with the own *MatLab* scripts, which were used in the thesis